Electron-phonon interactions and charge transport from first-principles calculations: complex crystals, higher order coupling, and steps toward the small polaron regime

Thesis by
Nien-En Lee

In Partial Fulfillment of the Requirements for the
Degree of
Doctor of Philosophy

CALIFORNIA INSTITUTE OF TECHNOLOGY
Pasadena, California

2021
Defended November 19, 2020

Nien-En Lee
ORCID: 0000-0002-3172-7750

ACKNOWLEDGEMENTS

I wish to express my sincere appreciation to my advisor, Professor Marco Bernardi, for your guidance, support, and encouragement throughout my Ph.D. life.

I wish to show my gratitude to Professor Nai-Chang Yeh, Professor Jason Alicea, and Professor Austin Minnich for serving on my thesis committee and for valuable feedback and advice.

I thank Hsiao-Yi for our fruitful discussion. I thank JinJian and Luis for collaborations and all the technical help. I thank everyone in the Bernardi group, Vatsal, I-Te, Austin, Megan, Vsevolod, Xiao, Jinsoo, Raffaello, Benjamin, Shiyuan, Ivan, and Dhruv, with whom I have overlapped.

I thank Kuan-Chang and Shun-Jia for our awesome time in the gym, and I thank all of my friends, Albert, Chia-Yi, Frank, Nancy, and more, who have being a part of my Ph.D. life.

I would like to thank my parents and parents-in-law for your full support. Lastly, I wish to express my deepest gratitude to my wife, Ting-Hsuan, and my lovely daughter, Evelyn, for your company in this arduous journey. Without you, I would not have accomplished what I have.

ABSTRACT

Electron-phonon (e-ph) interactions quantify the strength of interplay between charge carriers and lattice vibrations and critically determine the transport properties in materials near room temperature. Depending on the coupling strength, charge carriers can exhibit behaviors ranging from propagating waves extending across crystals to trapped particles localized in space. Therefore, accurately describing e-ph interactions plays a central role in quantitative transport studies on real materials. Over the last few years, first-principles methods combining density functional theory (DFT) and related techniques with the Boltzmann transport equation (BTE) have rapidly risen and reached maturity for investigating transport in various metals, semiconductors, and insulators with weak e-ph coupling. The lowest-order e-ph scattering process can be investigated starting from e-ph interactions from DFT calculations; this first-principles approach provides unambiguous quantitative prediction of transport properties such as the conductivity and mobility in common semiconductors and metals over a wide temperature range without using any empirical parameter. Encouraged by the agreement of the computed transport properties with experiment for many simple materials, this thesis aims to extend the applicability of this first-principles methodology and to further our understanding of microscopic transport mechanisms, especially in the wide temperature window near room temperature where transport is governed by e-ph scattering. We present research that expands the state of the art in three distinct ways, focusing on three research directions we pursue in this work. First, we employ the BTE to calculate the hole carrier mobility of naphthalene, an organic molecular crystal containing 36 atoms in a unit cell, the record largest system for first-principles charge transport calculations to date. The results are in excellent agreement with experiments, demonstrating that transport in some high-mobility organic semiconductors can still be explained within the band theory framework, and show that low-frequency rigid molecular motions control the electrical transport in organic molecular semiconductors in the bandlike regime. The second topic is an attempt to go beyond the lowest-order theory of e-ph interactions and quantify the importance of higher-order e-ph processes. We derive the electron-two-phonon scattering rates using many-body perturbation theory, compute them in GaAs, and quantify their impact on the electron mobility. We show that these next-to-leading order e-ph scattering rates, although smaller than the lowest-order contribution, are not

negligible, and can compensate the overestimation of mobility generally made by the lowest-order BTE calculation in weakly-polar semiconductors. In the third part of the thesis, we explore the opposite extreme case in which *e*-ph interactions are strong and lead to the formation of localized (so-called "polaron") electronic states that become self-trapped by the interactions with the atomic vibrations. We derive a rigorous approach based on canonical transformations to compute the energetics of self-localized (small) polarons in materials with strong *e*-ph interactions. With the aid of *ab initio* *e*-ph interactions, we carry out the corresponding numerical calculations to investigate the formation energy of small polaron and determine whether the charge carriers favor localized states over the Bloch waves. Due to the low computational cost of our approach, we are able to apply these calculations to various compounds, focusing on oxides, predicting the presence of small polaron in agreement with experiments in various materials. Our work paves the way to understanding small polaron formation and extending these calculations to predict transport in the polaron hopping mechanism in materials with strong *e*-ph coupling.

PUBLISHED CONTENT AND CONTRIBUTIONS

[1] N.-E. Lee, J.-J. Zhou, H.-Y. Chen, and M. Bernardi, Nat. Commun. **11**, 1607 (2020). DOI: 10.1038/s41467-020-15339-0.
N.-E. Lee participated in the conception of the project, derived the analytic expressions, implemented the code, carried out the numerical calculations, and wrote the manuscript.

[2] N.-E. Lee, J.-J. Zhou, L. A. Agapito, and M. Bernardi, Phys. Rev. B **97**, 115203 (2018). DOI: 10.1103/PhysRevB.97.115203.
N.-E. Lee contributed to conceiving the project and designing the research, carried out the numerical calculations, analyzed the results, and wrote the manuscript.

TABLE OF CONTENTS

LIST OF ILLUSTRATIONS

Chapter 1

INTRODUCTION

1.1 Overview

Electron-phonon (e-ph) interactions play an important role in solid state and material physics. They are key to understanding various physical phenomena and novel technological applications. For example, in a conventional superconductor [1], two electrons experience an attraction mediated by phonons and form a Cooper pair, resulting in a vanishing resistance below a critical temperature. In addition, phonons can assist the optical absorption in semiconductors with indirect band gap by providing the momentum required for the charge carrier to make an interband transition [2], which is shown to be crucial to photovoltaic devices based on Si and Ge. The interactions between electrons and phonons are also instrumental in understanding electrical and heat transport. In particular, e-ph interactions typically control charge transport near room temperature, setting an intrinsic limit to the electrical conductivity and mobility and determining their temperature dependence [3, 4]. In addition, they contribute to the zero-point renormalization and temperature dependence of the electronic band structure [5], and are crucial to understanding ultrafast dynamics [6], thermal conductivities [7], and thermoelectric transport [8].

Among these phenomena, the dominant role of e-ph interactions on room-temperature charge carrier transport is of fundamental importance to advancing novel technologies. Charge carrier transport in materials is typically characterized by the carrier mobility, which measures how fast a charge carrier can move on average in response to an applied electric field, determining the performance of modern electronic and optoelectronic devices. A low value of the room-temperature mobility reduces the operation speed of transistors [9], limits the efficiency in solar cells [10], and results in degradation in batteries [11]. As the e-ph interaction prevails over other sources of scattering such as impurities and defects [12] in this temperature range, a thorough understanding of microscopic e-ph processes can provide design rules and insights into systematic optimization of modern devices. Therefore, considerable efforts have been devoted to pursuing both qualitative and quantitative explanations on macroscopic transport properties using various microscopic transport mechanisms in a wide range of materials.

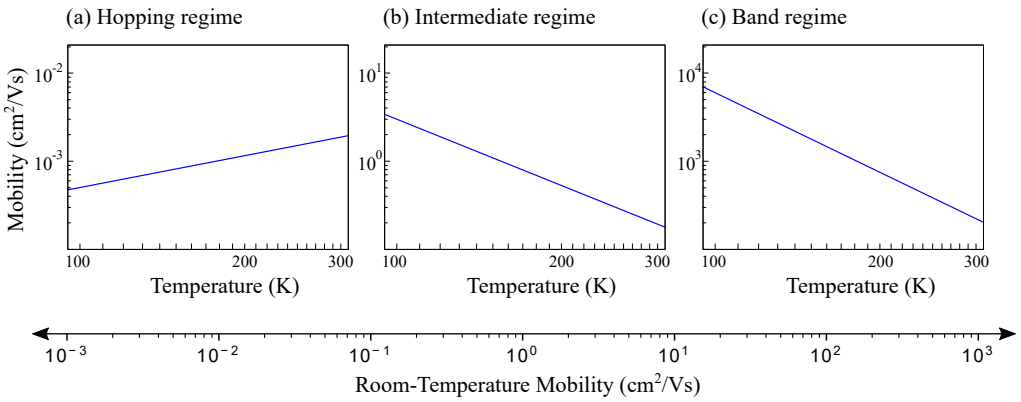

Figure 1.1: **Classification of transport regimes.** Illustration of the classification of transport regimes according to the absolute values of mobilities.

Materials can be roughly classified into three transport regimes according to the magnitude of their room-temperature mobilities, as illustrated in Fig. 1.1. Each regime corresponds to a specific transport behavior, due to a different strength of e-ph interactions, and is typically treated using different physical picture and theoretical approach. Charge transport in common semiconductors such as Si [13] and GaAs [14] occurs in the band transport regime, which is typical of high-mobility materials that have relatively weak e-ph interactions. In this regime, charge carriers can be described by quasiparticles associated with extended Bloch waves, whose motions are hindered only by occasional phonon scattering. This resistance from phonons increases at higher temperatures due to the increasing phonon number, resulting in a power-law decrease of the mobility in this regime [see Fig. 1.1(c)]. The opposite extreme is represented by materials with strong e-ph coupling and transport in the hopping regime, such as MnO [15] and CeO_2 [16]. This regime is characterized by low mobility values (typically, lower than 1 cm^2/Vs). The charge carriers in these materials couple strongly with phonons, forming localized distortions in the atomic lattice and becoming localized in space. These electrons can only diffuse in the material by incoherent hopping from site to site, and thus exhibit a macroscopic mobility typically increasing with temperature [see Fig. 1.1(a)]. The intermediate regime consists of materials with moderate mobility, and their temperature trends and transport mechanisms are highly material dependent.

E-ph interactions play a central role in transport study in all three regimes as they determine how often a charge carrier is scattered by phonons in the band regime or whether and how a charge carrier can distort its surrounding lattice and become

self-trapped in the hopping regime. Therefore, a proper description of *e*-ph interactions is critical to investigating the microscopic transport mechanism, and is a first step toward precise quantitative prediction. The conventional treatment of *e*-ph interactions consists of breaking them up into distinct physical mechanisms and analyzing them in the long-wavelength limit [17]. The value of each interaction, including the acoustic deformation potential, piezoelectric interaction, and the long-range optical Fröhlich coupling, is obtained by fitting experimental data or even set to an empirical constant. These empirical *e*-ph interactions are then combined with appropriate transport theory to investigate the charge carrier transport. For example, for weakly-coupled materials in band regime, charge carriers can be described by the semiclassical Boltzmann transport equation (BTE), and using empirical *e*-ph interactions, one can obtain a power-law decrease in the mobility with temperature [18]. However, this empirical approach is not predictive because it relies on experimental data for fitting, and it cannot unambiguously determine the contributions of the individual scattering mechanisms, which are combined as parameters in the theory. As such, the conventional treatment of charge transport is inadequate for quantitative predictions on real materials.

In the last decade, first-principles methods have emerged and quickly reached maturity to accurately compute *e*-ph interactions without using empirical parameters [19]. These calculations are based on density functional theory (DFT) [20, 21] and its linear response extension, density functional perturbation theory (DFPT) [22], to compute the *e*-ph matrix elements. This *ab initio* method provides unambiguous, accurate description on the *e*-ph interactions throughout the entire Brillouin zone, and is rapidly superseding the conventional approach described above. Combined with the BTE and the lowest-order *e*-ph scattering process, these first-principles methods can be routinely employed to make quantitative predictions of the transport properties of various metals and semiconductors in the band regime over a wide temperature range [3, 23–27], and have shifted the research focus from qualitative description of the model Hamiltonian to quantitative prediction on physical properties of real materials.

The success of BTE calculations in the band regime has triggered efforts on extending this first-principles methodology to the intermediate and hopping regimes, which are still relatively pristine territories for quantitative first-principles predictions. Researchers have started to incorporate *ab initio* *e*-ph interactions into more advanced transport theories in the past two years, trying to explain transport phe-

nomena in various scenarios. With the goal of advancing understanding of the microscopic transport mechanisms in real materials, this thesis work pursues three aspects of *ab initio* calculations of e-ph interactions and transport properties. First, it conducts a lowest-order e-ph scattering plus band transport BTE calculation in the organic molecular crystal naphthalene, pushing the frontiers of the current band transport calculations due to the structural complexity of naphthalene, a material with 36 atoms in the unit cell (and thus 108 phonon modes); ours is the record-largest calculation shown in the field to date. Our work on naphthalene additionally shows that some molecular crystals, where transport is commonly thought to occur in the intermediate or polaron hopping regimes, can in fact be well explained by band transport theory. We then derive an approach to compute next-to-leading order e-ph interactions, and show numerical calculations of the corresponding electron-two-phonon scattering rates in GaAs. Our results show that this next-to-leading order e-ph contribution, though smaller than the lowest-order interaction, is sizable and plays a role in mobility calculations in polar materials. Finally, we present a new framework for investigating materials with strong e-ph coupling, and derive an efficient computational approach to determine the energetics and formation of self-localized small-polaron electronic states in low-mobility materials, paving the way to understanding transport in the hopping regime. These advances and quantitative predictions of charge transport are enabled by the methodology for calculating e-ph interactions from first principles, which will be briefly reviewed in the next section.

1.2 First-Principles Electron-Phonon Interactions

First-principles calculations based on DFT have become an established computational tool to study the total energies and structural properties of real materials [19]. They find increasingly broad applications in condensed matter physics, quantum chemistry, and material science for predicting the behavior of materials within an atomistic framework [28, 29]. For example, they have achieved great success in obtaining band structures and optical properties in solids, as well as binding energies and the structure of molecules. These methods take only the crystal structures and atomic positions as inputs and do not make use of empirical parameters. A common approach, employed in this thesis, is DFT within the plane-wave pseudopotential framework [20, 21, 30]. The essence of DFT is formulating a theory of electrons in materials in which the ground state properties can be uniquely determined by the electron density, reformulating the many-electron problem into a convenient density-based framework amenable to efficient computations. The key result of the

theory is a Schrödinger-like equation, the Kohn-Sham (KS) equation, describing the mean-field behavior of a single electron in a material, where all the intractable many-body interactions among the electrons are represented by an exchange-correlation functional.

As calculations of ground state material properties have become well-established, the research focus has gradually shifted toward studying excited states within the first-principles framework [31]. To investigate electron dynamics, a conceptually straightforward approach is to evolve in time the electronic wavefunction and charge density obtained from the KS equation, an approach known as time-dependent DFT [32, 33]. Another route, adopted in this thesis, is leveraging well-developed transport theories within the many-body perturbation theory, typically BTE or linear response theory, while computing the relevant interactions using first-principles calculations. This approach is becoming widely successful for investigating electron dynamics and transport in a variety of systems. Let us briefly review this framework.

In the context of studying charge transport near room temperature in the phonon-limited regime, the starting point is usually taken to be the e-ph Hamiltonian

$$H = \sum_{n\mathbf{k}} \varepsilon_{n\mathbf{k}} a^\dagger_{n\mathbf{k}} a_{n\mathbf{k}} + \sum_{\nu\mathbf{q}} \omega_{\nu\mathbf{q}} \left(b^\dagger_{\nu\mathbf{q}} b_{\nu\mathbf{q}} + \frac{1}{2} \right) + \frac{1}{\sqrt{N_\Omega}} \sum_{mn\mathbf{k}} \sum_{\nu\mathbf{q}} g_{mn\nu}(\mathbf{k}, \mathbf{q}) \left(b^\dagger_{\nu-\mathbf{q}} + b_{\nu\mathbf{q}} \right) a^\dagger_{m\mathbf{k}+\mathbf{q}} a_{n\mathbf{k}}, \tag{1.1}$$

where $a_{n\mathbf{k}}$ and $b_{\nu\mathbf{q}}$ are the annihilation operators for electrons and phonons with energies $\varepsilon_{n\mathbf{k}}$ and $\omega_{\nu\mathbf{q}}$, respectively, and N_Ω is the number of unit cells in the crystal. The e-ph coupling constant $g_{mn\nu}(\mathbf{k}, \mathbf{q})$ is the probability amplitude for an electron in the Bloch state $|n\mathbf{k}\rangle$, with band index n and crystal momentum $\mathbf{k}$, to scattering to a final state $|m\mathbf{k} + \mathbf{q}\rangle$ due to an interaction with a phonon with mode index ν and momentum $\mathbf{q}$; we set $\hbar$ to unity here and in the following. We first briefly sketch how these quantities are obtained from first-principles calculations, and then outline the electron transport calculations in the following section. Further information can be found in Refs. [31, 34].

The electron energy $\varepsilon_{n\mathbf{k}}$ in Eq. (1.1) and its corresponding wavefunction $\psi_{n\mathbf{k}}$ are set to be the KS eigenvalue and eigenfunction, which satisfy the KS equation [21]

$$H^{\mathrm{KS}} \psi_{n\mathbf{k}} = \left(-\frac{1}{2m_\mathrm{e}} \nabla^2 + V^{\mathrm{KS}}\left[n_\mathrm{e}\right] \right) \psi_{n\mathbf{k}} = \varepsilon_{n\mathbf{k}} \psi_{n\mathbf{k}}, \tag{1.2}$$

where n_e is the charge density and m_e is the electron mass. The KS potential is denoted as V^{KS}, and is a functional of the charge density $V^{\mathrm{KS}} = V^{\mathrm{KS}}\left[n_\mathrm{e}\right]$. It

consists of three contributions, $V^{\mathrm{KS}} = V^{\mathrm{ext}} + V^{\mathrm{H}} + V^{\mathrm{XC}}$, which respectively account for the potentials from ions and core electrons, Hartree, and exchange-correlation interactions. The KS equation in Eq. (1.2) can be solved in a self-consistent manner: upon obtaining the KS wavefunctions $\psi_{n\mathbf{k}}$, the charge density can be calculated by summing the contributions from N_{e} electrons:

$$n_{\mathrm{e}} = \sum_{N_{\mathrm{e}}} |\psi_{n\mathbf{k}}|^2 .$$

This new charge density updates the KS potential in Eq. (1.2) and consequently gives a new set of wavefunctions $\psi_{n\mathbf{k}}$. This calculation is then repeated until the electron density, total energy, and electronic wavefunctions converge.

The properties of phonons, the quanta of lattice vibration, can also be calculated using linear response DFT (so-called density functional perturbation theory, DFPT) [22] by solving the Sternheimer equation associated with the first-order response to lattice perturbations. Denoting the ion displacement as u_κ, where $\kappa = cs\alpha$ is a composite index labelling the ion s in unit cell c moving in the Cartesian direction α, then the total energy of the crystal $E(u_\kappa)$ from DFT calculations with ions slightly deviated from their equilibrium positions can be expanded as

$$E(u_\kappa) = E_0 + \frac{1}{2} \sum_{\kappa\kappa'} \frac{\partial E}{\partial u_\kappa \partial u_{\kappa'}} u_\kappa u_{\kappa'} + \cdots , \tag{1.3}$$

where E_0 is the energy at equilibrium without ion displacements. The phonon frequency $\omega_{\nu\mathbf{q}}$ in Eq. (1.1) and its associated phonon eigenvector $e^{s\alpha}_{\nu\mathbf{q}}$ are then assigned to be the normal frequency and normal mode of the interatomic force constants $\partial E / \partial u_\kappa \partial u_{\kappa'}$. One straightforward real-space implementation is the frozen phonon approach [35, 36], which explicitly shifts the ion positions in a supercell, u_κ and $u_{\kappa'}$ in Eq. (1.3), to compute the force constants. In this thesis, we employ the more common and efficient DFPT method [22] formulated in momentum space in a plane-wave basis, as implemented in the Quantum ESPRESSO code [37]. The DFPT calculations directly compute the dynamical matrices, which are the Fourier transform of the interatomic force constants, at arbitrary phonon momentum $\mathbf{q}$, and can routinely compute the lattice dynamical properties using just a single unit cell.

The ion displacement u_κ also creates a perturbation in the KS potential that can scatters the propagating electrons. With similar notation as in the above treatment, we expand the KS potential with respect to the ion displacements as

$$V^{\mathrm{KS}}(u_\kappa) = V_0^{\mathrm{KS}} + \sum_{\kappa} \frac{\partial V^{\mathrm{KS}}}{\partial u_\kappa} u_\kappa + \cdots \tag{1.4}$$

$$= V_0^{\mathrm{KS}} + \sum_{\nu\mathbf{q}} \frac{1}{\sqrt{2\omega_{\nu\mathbf{q}}}} \Delta_{\nu\mathbf{q}} V^{\mathrm{KS}} \left(b_{\nu\mathbf{q}} + b_{\nu-\mathbf{q}}^{\dagger} \right).$$

In the second equality of Eq. (1.4), we use the fact that phonons are the normal modes of lattice vibration and express them in second quantized form [31], using

$$u_\kappa = \sum_{\nu\mathbf{q}} \frac{1}{\sqrt{2M_s\omega_{\nu\mathbf{q}}N_\Omega}} e_{\nu\mathbf{q}}^{s\alpha} e^{i\mathbf{q}\cdot\mathbf{R}_c} \left(b_{\nu\mathbf{q}} + b_{\nu-\mathbf{q}}^{\dagger} \right),$$

where M_s is the mass of atom s. The phonon perturbation potential felt by an electron due to a phonon in mode $\nu\mathbf{q}$ is defined as

$$\frac{1}{\sqrt{2\omega_{\nu\mathbf{q}}}} \Delta_{\nu\mathbf{q}} V^{\mathrm{KS}} = \frac{1}{\sqrt{2\omega_{\nu\mathbf{q}}}} \sum_\kappa \frac{e_{\nu\mathbf{q}}^{s\alpha}}{\sqrt{M_s}} \frac{e^{i\mathbf{q}\cdot\mathbf{R}_i}}{\sqrt{N_\Omega}} \frac{\partial V^{\mathrm{KS}}}{\partial u_\kappa},$$

and can be computed as a byproduct of the DFPT calculations. The e-ph coupling constant $g_{mn\nu}(\mathbf{k},\mathbf{q})$ is then readily computed as

$$g_{mn\nu}(\mathbf{k},\mathbf{q}) = \frac{1}{\sqrt{2\omega_{\nu\mathbf{q}}}} \langle \psi_{m\mathbf{k}+\mathbf{q}} | \Delta_{\nu\mathbf{q}} V^{\mathrm{KS}} | \psi_{n\mathbf{k}} \rangle,$$

which is fully *ab initio* since all quantities involved in the integral are obtained from DFT and DFPT calculations.

In principle, the e-ph Hamiltonian in Eq. (1.1) can now be built up for arbitrary electron and phonon momenta $\mathbf{k}$ and $\mathbf{q}$. However, a transport calculation usually involves integrals over both $\mathbf{k}$ and $\mathbf{q}$ requiring very dense Brillouin zone grids to achieve numerical convergence, and it is prohibitive to compute all the relevant quantities by direct DFT and DFPT calculations at all grid points. Therefore, in practice, we first compute the e-ph coupling constants and other relevant quantities on coarser grids, typically of order $10 \times 10 \times 10$, and then we employ various interpolation techniques – in our calculations, Fourier interpolation based on Wannier function, to obtain the e-ph matrix elements on fine grids, and tetrahedron integration to compute the conductivity and mobility [34]. Details of the interpolation schemes can be found in the paper of the PERTURBO code [34], developed in the Bernardi group at Caltech and employed in this thesis to compute the e-ph coupling matrix elements and the transport properties.

1.3 Band Transport and Electron-Phonon Scattering

The *ab initio* e-ph Hamiltonian obtained in the previous section can be combined with any transport theory for quantitative predictions. For materials with transport in the band regime, the semiclassical BTE is of particular importance because it

usually gives a satisfactory result at an affordable computational cost. Since the e-ph interactions are relatively weak in the band regime, the electrons can be described by weakly interacting quasiparticles in Bloch states $|n\mathbf{k}\rangle$, and the probability that these electronic states are occupied is quantified by the distribution function $f_{n\mathbf{k}}$. The BTE depicts how this distribution function $f_{n\mathbf{k}}$ evolves in time in a system out of equilibrium. As such, it can also provide the steady state distribution of the electron when an external electric field $\mathbf{E}$ is applied, from which various transport coefficients can be extracted [38].

In the case of a weak electric field, we assume that the distribution function deviates only slightly from its equilibrium value, and define this linear deviation by introducing the quantity $\mathbf{F}_{n\mathbf{k}}$:

$$f_{n\mathbf{k}} = f^0_{n\mathbf{k}} + e\mathbf{E}\cdot\mathbf{F}_{n\mathbf{k}} f^0_{n\mathbf{k}}\left(1 - f^0_{n\mathbf{k}}\right)\beta + O(E^2).$$

In this expansion, $f^0_{n\mathbf{k}}$ is the Fermi-Dirac distribution, $\beta = 1/k_\mathrm{B}T$ is the inverse temperature, with k_B the Boltzmann constant, and e as the electron charge. The BTE can then be linearized as (see Appendix B for detailed derivations)

$$\mathbf{F}_{n\mathbf{k}} = \tau_{n\mathbf{k}}\mathbf{v}_{n\mathbf{k}} + \frac{\tau_{n\mathbf{k}}}{N_\Omega}\sum_{m\nu\mathbf{q}} \mathbf{F}_{m\mathbf{k}+\mathbf{q}}\widetilde{\Gamma}^{\nu\mathbf{q}}_{n\mathbf{k},\,m\mathbf{k}+\mathbf{q}}, \tag{1.5}$$

where $\tau_{n\mathbf{k}}$ and $\mathbf{v}_{n\mathbf{k}}$ are the relaxation time and band velocity, respectively, and $\widetilde{\Gamma}^{\nu\mathbf{q}}_{n\mathbf{k},\,m\mathbf{k}+\mathbf{q}}$ is the scattering rate between states $|n\mathbf{k}\rangle$ and $|m\mathbf{k}+\mathbf{q}\rangle$. As mentioned above, solving the BTE amounts to finding the unknown electron distribution $f_{n\mathbf{k}}$, in practice by solving for its linear-in-field variation, $\mathbf{F}_{n\mathbf{k}}$ in Eq. (1.5). A common approach is the relaxation time approximation (RTA), which neglects the second term on the right hand side of Eq. (1.5) and approximates $\mathbf{F}_{n\mathbf{k}}$ to $\tau_{n\mathbf{k}}\mathbf{v}_{n\mathbf{k}}$, therefore neglecting the backscattering events. A more accurate solution can be obtained by iteratively solving Eq. (1.5) [24]. After solving the equation, the electrical mobility can be obtained through

$$\mu^\alpha = \frac{2e\beta}{n_c V_\mathrm{uc}}\sum_{n\mathbf{k}} f_{n\mathbf{k}}(1 - f_{n\mathbf{k}})v^\alpha_{n\mathbf{k}}F^\alpha_{n\mathbf{k}}, \tag{1.6}$$

where V_uc is the unit cell volume and n_c the charge carrier concentration. Loosely speaking, if the electric field points in one direction – say, to the "right", the electrons experience an electric force and move to the left. This motion is compensated by the scattering events $\widetilde{\Gamma}^{\nu\mathbf{q}}_{n\mathbf{k},\,m\mathbf{k}+\mathbf{q}}$ and the system eventually reaches a steady state. The electron distribution in this steady state, which can be obtained by solving Eq. (1.5),

has more left-moving than the right-moving electrons, therefore building up an electrical current.

The scattering term $\widetilde{\Gamma}^{\nu\mathbf{q}}_{n\mathbf{k},\,m\mathbf{k}+\mathbf{q}}$ on the right hand side of Eq. (1.5) should in principle encompass collisions from every possible source (not just e-ph interactions) that scatter a charge carrier from state $|n\mathbf{k}\rangle$ to state $|m\mathbf{k}+\mathbf{q}\rangle$. Nevertheless, near room temperature the e-ph interactions have a dominant contribution, and in practical transport calculations for materials with relatively weak coupling strength, it typically suffices to include only the lowest order e-ph scattering processes [31], using:

$$\widetilde{\Gamma}^{\nu\mathbf{q}}_{n\mathbf{k},\,m\mathbf{k}+\mathbf{q}} = 2\pi\,|g_{mn\nu}(\mathbf{k},\mathbf{q})|^2\left[\left(1+N^0_{\nu\mathbf{q}}-f^0_{m\mathbf{k}+\mathbf{q}}\right)\delta\left(\varepsilon_{n\mathbf{k}}-\varepsilon_{m\mathbf{k}+\mathbf{q}}-\omega_{\nu\mathbf{q}}\right)\right. \\ \left. +\left(N^0_{\nu\mathbf{q}}+f^0_{m\mathbf{k}+\mathbf{q}}\right)\delta\left(\varepsilon_{n\mathbf{k}}-\varepsilon_{m\mathbf{k}+\mathbf{q}}+\omega_{\nu\mathbf{q}}\right)\right], \tag{1.7}$$

where $N^0_{\nu\mathbf{q}}$ is the Bose-Einstein distribution for phonon in mode $\nu\mathbf{q}$. The first and second terms correspond to scattering events where an electron emits or absorbs one phonon, respectively, and the delta functions enforce energy conservation between initial and final states. The relaxation time in Eq. (1.5) is defined as the inverse of the first-order e-ph scattering rate,

$$\frac{1}{\tau_{n\mathbf{k}}} = \Gamma_{n\mathbf{k}} = \frac{1}{N_\Omega}\sum_{m\nu\mathbf{q}}\widetilde{\Gamma}^{\nu\mathbf{q}}_{n\mathbf{k},\,m\mathbf{k}+\mathbf{q}}. \tag{1.8}$$

A typical workflow for computing the mobility within the RTA involves converging the integral in Eq. (1.6) over the $\mathbf{k}$-point grid, with $\mathbf{F}_{n\mathbf{k}}$ set equal to $\tau_{n\mathbf{k}}\mathbf{v}_{n\mathbf{k}}$. The relaxation time $\tau_{n\mathbf{k}}$ at each $\mathbf{k}$ point is computed using Eqs. (1.7) and (1.8), paying special attention to converging the integral over the $\mathbf{q}$ point grid. In these integrations, the e-ph coupling constants $g_{mn\nu}(\mathbf{k},\mathbf{q})$ are obtained on fine $\mathbf{k}$- and $\mathbf{q}$-point grids by the Fourier-Wannier interpolation of the coarse-grid DFPT e-ph coupling constants [34]. The delta functions in Eq. (1.7) are approximated by Gaussian functions with a small broadening, typically of order 5 meV. This workflow has been applied extensively by our group and can accurately compute the room-temperature mobility for a wide range of metals and semiconductors with weak e-ph coupling, showing that the BTE can successfully explain electrical transport in the band regime.

However, applying this first-principles methodology to the intermediate and hopping regimes is an open challenge for various reasons. As the strength of the e-ph interactions increases, the lowest-order perturbative treatment is expected to be inadequate both because higher-order e-ph processes become important and because

of the need to resort to more advance transport theories to include effects not captured by the BTE. In materials with moderate e-ph interaction strength, the charge carriers are still mobile, but, contrary to the weakly interacting quasiparticle picture in the band regime, they are dressed by a phonon cloud, forming a composite particle known as large polaron. The weights of their spectral function no longer concentrates around the quasiparticle peak, an effect that needs to be carefully taken into account for quantitative transport predictions. For example, recent work from our group [4] combined *ab initio* electron spectral functions from a cumulant approach with the Green-Kubo conductivity formula from linear response theory. Their treatment can successfully explain electron transport in $SrTiO_3$, a material with transport in the intermediate regime, where a lowest-order e-ph plus BTE calculation significantly overestimates the mobility [39]. For materials with strong e-ph interactions, perturbation theory breaks down, and charge carriers typically couple to the lattice so strongly that they form self-localized small polaron states [40]. Pioneering work on small polarons and their hopping transport mechanism were started decades ago [41, 42], but the resulting theoretical frameworks have not yet been combined with first-principles calculations to achieve quantitative predictions.

Another reason for the slow progress is that materials with transport in the intermediate and hopping regimes tend to have complex atomic or electronic structures, posing additional challenges for accurate first-principles descriptions from DFT and related methods. For example, although organic semiconductors [43, 44] play a critical role in environmental-friendly and flexible electronic devices, understanding their transport mechanisms remains a formidable challenge due to their large numbers of atoms in the unit cell, typically ranging from a few tens to a few hundreds, which is orders of magnitude more than common inorganic semiconductors. Calculations of phonon dispersions and e-ph coupling using DFPT, which scales as the third power of system size with a large prefactor, become prohibitive for more than a few tens of atoms in the unit cell. Another relevant example are perovskites [39], many of which exhibit structural phase transitions at finite temperature that DFT calculations, which capture zero-temperature ground state properties, cannot properly handle, so that direct application of the DFPT method using the room-temperature structure usually results in phonons with negative frequencies due to strong anharmonic effects. In addition, many materials in the intermediate and hopping regimes contain transition metals with open d or f shell. Standard DFT calculations usually fail in modelling these localized electrons due to self-interaction errors inherent in the conventional exchange-correlation functionals, predicting inaccurate band gaps

and physical properties. As a result, combining *ab initio* e-ph calculations with transport theories to study the intermediate and hopping regimes is an ongoing research effort, and one receiving increasing attention in the past few years.

1.4 Thesis Outline

Using as a starting point the first-principles e-ph calculations and the transport theories introduced above, this thesis presents research at the forefront of *ab initio* e-ph interactions and transport calculations, articulated into three research directions, each addressing an open challenge in the field.

In chapter 2, we demonstrate calculations combining the BTE and *ab initio* e-ph coupling constants on an organic molecular crystal, naphthalene, whose hole mobility is of the order of $1-10$ cm^2/Vs, and therefore at the crossroad between the band and intermediate transport regimes. Our results for the hole mobility in naphthalene are in excellent agreement with experiments and can accurately predict the mobility and its temperature dependence over a wide temperature range. We take all 108 phonon modes into account, and show that intermolecular phonons, consisting of low-frequency rigid molecular motions such as acoustic or molecular rotational modes, control the mobility due to their large scattering phase space near the band edge. This work also demonstrates that the applicability of band theory and the BTE can be extended to some materials in the intermediate regime and to hole transport in various organic semiconductors. It also forms the basis for extending studies of organic materials to the intermediate and hopping regimes, and to understand the shortcomings of widely-used simplified transport models in organic materials.

Chapter 3 is devoted to investigating next-to-leading order e-ph scattering processes and how they affect the mobility. The BTE can accurately predict transport in the band regime, but it substantially overestimates the mobility in weakly polar semiconductors. An example is GaAs, where the (carefully converged) lowest-order e-ph plus BTE result is about twice greater than the measured mobility. As the charge carriers in polar materials experience the Fröhlich interaction with longitudinal optical phonons, which can range from weak to strong depending on how strongly polar are the chemical bonds, one expects that the discrepancy between the BTE result and experiments is due to omission of higher-order e-ph effects. In this work, we derive the analytic expressions for the electron-two-phonon (2ph) scattering rates by calculating two-loop Feynman diagrams, and evaluate their

numerical values from first principles for GaAs. The results, to our surprise, show that the 2ph scattering rates are not negligibly small, and are nearly half the value of the lowest-order scattering rates. We rationalize their peculiar dependence on electron energy, and demonstrate that the overestimation of the calculated mobility in GaAs can be compensated by taking this next-to-leading order 2ph scattering processes into account.

In Chapter 4, we extend the first-principles methodology to the hopping regime and investigate small polaron formation in materials with strong e-ph coupling. The small polaron is a self-localized electronic state trapped by the local lattice distortion it induces. In early theoretical treatments, the presence of this self-localized state was typically assumed rather than predicted. We develop a formalism based on canonical transformations to compute the polaron formation energy and wavefunction using *ab initio* e-ph interactions. By direct comparison of the calculated polaron energy with the conduction or valence band edge, we can infer whether charge carriers in a material favor a localized small polaron over a delocalized Bloch state. The formalism presented in this chapter enables preditions of small polaron formation in materials, as demonstrated through the examples of alkali halides and metal oxides. It also serves as the starting point for developing quantitative transport predictions in the hopping regime.

References

[1] J. Bardeen, L. N. Cooper, and J. R. Schrieffer, Phys. Rev. **108**, 1175–1204 (1957).

[2] J. Noffsinger, E. Kioupakis, C. G. Van de Walle, S. G. Louie, and M. L. Cohen, Phys. Rev. Lett. **108**, 167402 (2012).

[3] J.-J. Zhou and M. Bernardi, Phys. Rev. B **94**, 201201 (2016).

[4] J.-J. Zhou and M. Bernardi, Phys. Rev. Research **1**, 033138 (2019).

[5] G. Antonius, S. Poncé, E. Lantagne-Hurtubise, G. Auclair, X. Gonze, and M. Côté, Phys. Rev. B **92**, 085137 (2015).

[6] X. Tong and M. Bernardi, Preprint at arXiv:2009.07958 (2020).

[7] T. Y. Kim, C.-H. Park, and N. Marzari, Nano Lett. **16**, 2439–2443 (2016).

[8] Z. Wang, S. Wang, S. Obukhov, N. Vast, J. Sjakste, V. Tyuterev, and N. Mingo, Phys. Rev. B **83**, 205208 (2011).

[9] A. S. Sedra and K. C. Smith, *"Microelectronic Circuits"*, 6th ed. (Oxford University Press, 2009).

[10] K. A. Mazzio and C. K. Luscombe, Chem. Soc. Rev. **44**, 78–90 (2015).

[11] J. Kang, Y. S. Jung, S.-H. Wei, and A. C. Dillon, Phys. Rev. B **85**, 035210 (2012).

[12] I.-T. Lu, J.-J. Zhou, and M. Bernardi, Phys. Rev. Materials **3**, 033804 (2019).

[13] C. Jacoboni, C. Canali, G. Ottaviani, and A. Alberigi Quaranta, Solid-State Electronics **20**, 77–89 (1977).

[14] D. L. Rode, Phys. Rev. B **2**, 1012–1024 (1970).

[15] C. Crevecoeur and H. D. Wit, J. Phys. Chem. Solids **31**, 783–791 (1970).

[16] H. Tuller and A. Nowick, J. Phys. Chem. Solids **38**, 859–867 (1977).

[17] G. D. Mahan, *"Many-Particle Physics"*, 3rd ed. (Springer, 2000).

[18] B. Segall, M. R. Lorenz, and R. E. Halsted, Phys. Rev. **129**, 2471–2481 (1963).

[19] R. M. Martin, *"Electronic Structure: Basic Theory and Practical Methods"*, 1st ed. (Cambridge University Press, 2004).

[20] P. Hohenberg and W. Kohn, Phys. Rev. **136**, B864–B871 (1964).

[21] W. Kohn and L. J. Sham, Phys. Rev. **140**, A1133–A1138 (1965).

[22] S. Baroni, S. de Gironcoli, A. Dal Corso, and P. Giannozzi, Rev. Mod. Phys. **73**, 515–562 (2001).

[23] V. A. Jhalani, J.-J. Zhou, J. Park, C. E. Dreyer, and M. Bernardi, Phys. Rev. Lett. **125**, 136602 (2020).

[24] W. Li, Phys. Rev. B **92**, 075405 (2015).

[25] J. Ma, A. S. Nissimagoudar, and W. Li, Phys. Rev. B **97**, 045201 (2018).

[26] T.-H. Liu, J. Zhou, B. Liao, D. J. Singh, and G. Chen, Phys. Rev. B **95**, 075206 (2017).

[27] G. Brunin, H. P. C. Miranda, M. Giantomassi, M. Royo, M. Stengel, M. J. Verstraete, X. Gonze, G.-M. Rignanese, and G. Hautier, Phys. Rev. B **102**, 094308 (2020).

[28] A. D. Becke, J Chem. Phys. **140**, 18A301 (2014).

[29] P. J. Hasnip, K. Refson, M. I. J. Probert, J. R. Yates, S. J. Clark, and C. J. Pickard, Philos. Trans. R. Soc. A **372**, 20130270 (2014).

[30] N. Troullier and J. L. Martins, Phys. Rev. B **43**, 1993–2006 (1991).

[31] M. Bernardi, Eur. Phys. J. B **89**, 239 (2016).

[32] E. Runge and E. K. U. Gross, Phys. Rev. Lett. **52**, 997–1000 (1984).

[33] M. A. Marques, A. Castro, G. F. Bertsch, and A. Rubio, Comp. Phys. Commun. **151**, 60–78 (2003).

[34] J.-J. Zhou, J. Park, I.-T. Lu, I. Maliyov, X. Tong, and M. Bernardi, Preprint at arXiv:2002.02045 (2020).

[35] G. J. Ackland, M. C. Warren, and S. J. Clark, J. Phys. Condens. Matter **9**, 7861–7872 (1997).

[36] M. T. Yin and M. L. Cohen, Phys. Rev. B **26**, 3259–3272 (1982).

[37] P. Giannozzi et al., J. Phys. Condens. Matter **21**, 395502 (2009).

[38] M. P. Marder, *"Condensed Matter Physics"*, 2nd ed. (Wiley, 2015).

[39] J.-J. Zhou, O. Hellman, and M. Bernardi, Phys. Rev. Lett. **121**, 226603 (2018).

[40] D. Emin, Phys. Today **35**, 34 (1982).

[41] T. Holstein, Ann. Phys. (N. Y.) **8**, 343–389 (1959).

[42] I. G. Lang and Y. A. Firsov, J. Exptl. Theoret. Phys. (U.S.S.R.) **43**, 1843–1860 (1962).

[43] F. Brown-Altvater, T. Rangel, and J. B. Neaton, Phys. Rev. B **93**, 195206 (2016).

[44] F. Brown-Altvater, G. Antonius, T. Rangel, M. Giantomassi, C. Draxl, X. Gonze, S. G. Louie, and J. B. Neaton, Phys. Rev. B **101**, 165102 (2020).

Chapter 2

BANDLIKE HOLE MOBILITY IN NAPHTHALENE CRYSTAL

This chapter is a slightly modified version of the published article:

N.-E. Lee, J.-J. Zhou, L. A. Agapito, and M. Bernardi, *"Charge transport in organic molecular semiconductors from first principles: The bandlike hole mobility in a naphthalene crystal"*, Phys. Rev. B 97, 115203 (2018).

2.1 Introduction

Organic molecular crystals are broadly relevant to solid state physics. Their electronic properties range from conducting to insulating, and they can exhibit anisotropic electrical and optical properties, ferroelectricity, magnetism, and superconductivity. Organic semiconductors are lead candidates for novel optoelectronics and spintronics applications [1, 2]. Crystals like pentacene and rubrene are already widely used in organic field-effect transistors and light-emitting devices [3–5].

Yet, in most organic crystals the nature and transport mechanisms of charge carriers remain unclear. Possible charge transport regimes include polaron charge hopping, band transport, and intermediate regimes, each leading to a peculiar temperature dependence of the mobility. Even in the same organic crystal, electrons and holes can behave differently. An example is naphthalene, where hole carriers display bandlike transport with a power-law temperature dependence of the mobility [6], though

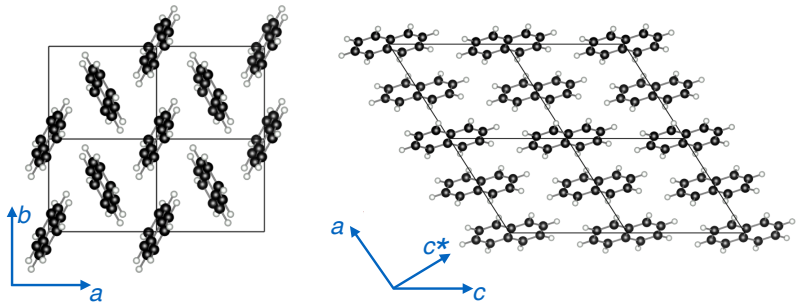

Figure 2.1: **Crystal structure of naphthalene.** The monoclinic crystal structure of naphthalene, with two molecules in the unit cell. The molecules are arranged in a herringbone pattern in the *ab* planes (left), which are stacked in the *c* crystallographic direction (right). The *c** direction normal to the *ab* plane is also shown.

electron transport in the out-of-plane direction is polaronic and nearly temperature independent [7].

Several approaches have been proposed to compute charge transport in organic crystals [8]. Recent calculations favor either quantum chemistry methods based on hopping of localized charge carriers [8–15], or somewhat less extensively polaron theories [16–21]. Charge hopping calculations have provided remarkable insight into charge transport in molecular crystals [8–15]. However, they are laborious, and are not based on rigorous condensed matter theory. They require large molecular dynamics or Monte Carlo simulations, rely on semiempirical charge transfer models based on Marcus theory, and include the temperature dependence of charge transport only approximately, typically using the Einstein diffusion formula. A common assumption is also that only rigid molecular motions affect the rate of carrier hopping, and therefore charge transport. The accuracy of the charge hopping approaches is limited – the best calculations yield mobility values 3–4 times greater than the experiment [9, 10], though order-of-magnitude discrepancies between computed and measured mobilities are more common [8].

To date, only few works have employed band theory to compute charge transport in organic crystals [22–25], despite experimental [26–29] and theoretical [30] evidence of bandlike transport in tetracene, rubrene, naphthalene, and other organic semiconductors. Methods combining band theory and many-body perturbation theory have been recently employed to accurately compute e-ph scattering and charge transport, for now in simple inorganic materials with a handful of atoms in the unit cell [31–34]. Due to computational cost, these calculations have not yet been applied to organic crystals with tens of atoms in the unit cell. *Ab initio* studies of e-ph coupling in organic crystals exist [35–37], but charge transport, which requires more elaborate workflows [32], has not yet been investigated within this framework.

Here we compute from first principles the bandlike hole mobility of naphthalene crystal, a material with 36 atoms in the unit cell (see Fig. 2.1). The computed mobility is within a factor of 3–4 of experiment, and we can accurately predict its temperature dependence between 100–300 K. For organic semiconductors, these results are a rare case of very good quantitative agreement with experiment – the accuracy on the mobility is on par with the best charge hopping calculations, and we make an order of magnitude improvement over previous *ab initio* mobility calculations in organic crystals using band theory [22, 23]. We show that intermolecular phonons (i.e., rigid molecular motions) regulate the mobility due to a large phase

space for scattering holes with energy close to the band edge. Yet, contrary to common notions, intramolecular phonons exhibit the strongest coupling with holes. Our work reconciles the tenet of charge hopping methods that intermolecular phonons control the mobility with the many-body theory perspective, which treats carrier scattering in terms of phonon absorption and emission events.

2.2 Methods

We carry out density functional theory (DFT) calculations using the QUANTUM ESPRESSO code [38] with a plane-wave basis set. We employ the Perdew-Burke-Ernzerhof generalized gradient approximation [39] and norm-conserving pseudopotentials [40] from Pseudo Dojo [41]. A kinetic energy cutoff of 90 Ry and $4\times4\times4$ **k**-point grids are used in all DFT calculations. Thermal expansion is taken into account by employing, in separate calculations, lattice constants [42] and atomic positions [43, 44] taken from experiment at four different temperatures of 100, 160, 220, and 300 K. All calculations listed below are repeated separately at these four temperatures. The Grimme van der Waals (vdW) correction [45, 46] is included during structural relaxation. To obtain accurate electronic band structures [47], we carry out GW calculations using the YAMBO code [48], and obtain the G_0W_0 self-energy using 500 bands in the polarization function and a cutoff of 10 Ry in the dielectric screening. WANNIER90 [49] is employed to interpolate the band structure, using *ab initio* molecular orbitals [50] as initial guesses.

Phonon dispersions are computed with density functional perturbation theory (DFPT) [51] on a $2\times4\times2$ **q**-point grid [52]. The e-ph coupling matrix elements $g_{nm\nu}(\mathbf{k},\mathbf{q})$ on coarse **k**- and **q**-point grids [34] are computed using a routine from the EPW code [53] and interpolated using Wannier functions [54] generated with the WANNIER90 code [49]. Here and in the following, n and m are band indices, ν labels phonon modes, and **k** and **q** are crystal momenta for electrons and phonons, respectively. Our in-house developed code PERTURBO [55] is employed to interpolate the e-ph matrix elements on fine grids with up to $60\times60\times60$ **k**-points and 10^5 random **q**-points, and to compute e-ph scattering rates and the hole mobility. The band- and momentum-resolved e-ph scattering rates $\Gamma^{e\text{-ph}}_{n\mathbf{k}}$ are obtained in the lowest order of perturbation theory [34],

$$\Gamma^{e\text{-ph}}_{n\mathbf{k}} = \frac{2\pi}{\hbar}\sum_{m\nu\mathbf{q}}|g_{nm\nu}(\mathbf{k},\mathbf{q})|^2\left[(N_{\nu\mathbf{q}}+1-f_{m\mathbf{k}+\mathbf{q}})\delta(\varepsilon_{n\mathbf{k}}-\varepsilon_{m\mathbf{k}+\mathbf{q}}-\hbar\omega_{\nu\mathbf{q}})\right. \quad (2.1)$$
$$\left.+(N_{\nu\mathbf{q}}+f_{m\mathbf{k}+\mathbf{q}})\delta(\varepsilon_{n\mathbf{k}}-\varepsilon_{m\mathbf{k}+\mathbf{q}}+\hbar\omega_{\nu\mathbf{q}})\right],$$

where $\varepsilon_{n\mathbf{k}}$ and $\hbar\omega_{\nu\mathbf{q}}$ are the hole and phonon energies, respectively, and $f_{n\mathbf{k}}$ and $N_{\nu\mathbf{q}}$ the corresponding occupations. The scheme developed in our recent work [32] is applied to converge $\Gamma^{e\text{-ph}}_{n\mathbf{k}}$. The relaxation times $\tau_{n\mathbf{k}}$ used in the mobility calculations are the inverse of the scattering rates, $\tau_{n\mathbf{k}} = 1/\Gamma^{e\text{-ph}}_{n\mathbf{k}}$. Our calculations focus on holes, and include only the HOMO and HOMO−1 bands because the energy gaps to the HOMO−2 and LUMO bands are larger than the highest phonon frequency.

We employ the Boltzmann transport equation [32, 56] within the relaxation time approximation to calculate the electrical conductivity

$$\sigma_{\alpha\beta}(T) = e^2 \int_{-\infty}^{\infty} dE \left(-\frac{\partial f(E,T)}{\partial E}\right) \Sigma_{\alpha\beta}(E,T) \tag{2.2}$$

where the transport distribution function $\Sigma_{\alpha\beta}(E,T)$ at energy E and temperature T is defined as

$$\Sigma_{\alpha\beta}(E,T) = \frac{2}{V_{\text{uc}}} \sum_{n\mathbf{k}} \tau_{n\mathbf{k}}(T) v_{n\mathbf{k},\alpha} v_{n\mathbf{k},\beta}\, \delta(E - \varepsilon_{n\mathbf{k}}) \tag{2.3}$$

and is calculated via tetrahedron integration [57]. The band velocities $\mathbf{v}_{n\mathbf{k}}$ are obtained from Wannier interpolation; α and β are cartesian directions, and V_{uc} is the unit cell volume. The hole mobility along the direction α is computed using $\mu_\alpha = \sigma_{\alpha\alpha}/n_p|e|$, where n_p is the hole concentration. These e-ph and mobility calculations on unit cells with tens of atoms are made possible by efficient algorithms combining MPI plus OpenMP parallelizations we recently developed.

The computed band structures and phonon dispersions are given in the Supplementary Materials (See Fig. 2.5). The GW correction is important as it stretches the valence band, thus lowering the hole effective mass and changing the relative alignment of the valence band valleys. The quality of our phonon dispersions is comparable with that of recent accurate phonon calculations in naphthalene [52]. For reference, we also employ the methods above to compute the phonon dispersion of the perdeuterated naphthalene. The comparison with experimental data is given in the Supplementary Materials (See Fig. 2.7).

2.3 Results

Figure 2.2 shows our calculated hole mobilities in the in-plane a and b and the plane-normal c^* directions (see Fig. 2.1). The experimental data given for comparison is taken from Ref. [6]. The computed mobilities are lower by a factor of 3−5 than the experimental values; the smallest discrepancy (a factor of 3) is found for the a direction, and the highest (a factor of 5) in the c* direction. Note that the

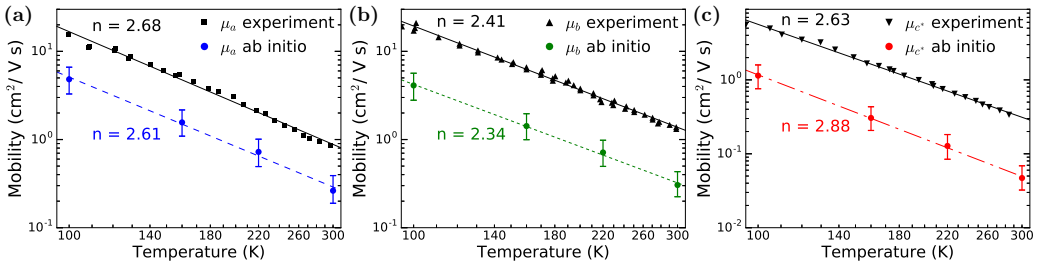

Figure 2.2: **Calculated hole mobility in naphthalene.** The hole mobility in naphthalene, given, from left to right in separate panels, in the two in-plane directions a, b, and in the plane-normal direction c*. Circle markers are the computed mobilities and black markers the experimental data from Ref. [6]. Straight lines are best fits to the power law function T^{-n} of the data points in the 100−300 K temperature range, and the exponent n for each data set is also given. The error bars are obtained by assuming a 10% error on both the phonon frequencies and the GW band stretching factor. These error sources are assumed to be independent and combined together.

c* axis corresponds to a direction along which the molecules are stacked, so that the slightly lower accuracy in this direction is expected due to our neglect of van der Waals interactions in the e-ph coupling. Fitting the data with a power law function T^{-n} over the 100−300 K temperature range yields calculated exponents n in the 2.34−2.88 range for the three directions, in agreement *within 3%* (in the ab plane) and 10% in the c* direction with the exponents n obtained by fitting the experimental data (see Fig. 2.2). The charge transport anisotropy is estimated by evaluating mobility ratios between different directions at 300 K. The computed ratios, $\mu_b/\mu_a = 1.16$ and $\mu_{c*}/\mu_a = 0.18$ are consistent with the experimental values of 1.57 and 0.34, respectively.

Since the accuracy of the phonon dispersions and GW band structures depends on the chosen crystal structure, exchange-correlation functional, and pseudopotential, it is important to quantify how these sources of uncertainty affect the computed mobility. To this end, we estimate how the combination of a small error in the GW correction (arbitrarily chosen to be ∼10% in the stretching factor of the valence band) and an assumed ∼10% error on the phonon frequencies (a conservative value for organic crystals) affect our calculations. The resulting error bars on the mobilities are given in Fig. 2.2.

Within these uncertainties, which are typical of *ab initio* methods − especially for organic crystals with complex structures − the range of computed mobilities (inclusive of the error bars) reaches values roughly 2−3 times smaller than the

experimental results in the in-plane a and b directions. Overall, the temperature trends and absolute values of the mobility are remarkably accurate, particularly when compared to the very scarce literature on charge transport in organic crystals using *ab initio* band theory. Our accuracy is comparable to the best calculations [9, 10] using quantum chemistry methods based on hopping that dominate the literature.

We have verified that employing the Tkatchenko-Scheffler (TS) vdW correction [58, 59], which is more accurate than the Grimme-vdW correction used here, does not change appreciably the structure and mobility. In particular, the root-mean-square (RMS) deviation between the atomic positions obtained with the Grimme-vdW and the TS-vdW corrections is only 0.05 Å, and the RMS deviation of the bond lengths is ∼0.05%. The mobility at 300 K obtained by computing the band structure, phonons, and e-ph matrix elements with the structure obtained using the TS-vdW correction is very close (within 5−10%, and thus within the error bars in Fig. 2.2) to the mobility computed here using the Grimme-vdW method (see Fig. 2.6 in the Supplementary Materials). Future work will investigate further the role of the vdW correction on the e-ph coupling and mobility in organic crystals.

Next, we investigate the role of different phonon modes in scattering the hole carriers. In the charge hopping picture, the conventional wisdom is that low-frequency intermolecular phonon modes, which correspond to rigid motions of entire molecules [12, 13], determine the mobility since they strongly affect the rate of charge hopping between molecules. Intramolecular vibrations, on the other hand, are typically neglected due to their hypothesized weaker coupling to the carriers. There are 108 phonon modes in naphthalene; the 12 lowest-frequency modes are intermolecular, and the others are intramolecular. We express the total e-ph scattering rate in Eq. (2.1) as the sum of the scattering rates due to each individual mode ν, i.e., $\Gamma^{e\text{-ph}}_{n\mathbf{k}} = \sum_\nu \Gamma^{(\nu)}_{n\mathbf{k}}$, and investigate the mode-resolved scattering rates $\Gamma^{(\nu)}_{n\mathbf{k}}$. Here and in the following, the phonon modes are numbered in order of increasing energy at the Brillouin zone center, and the hole energy increases moving away from the valence band maximum (VBM) into the valence band.

Figure 2.3(a) shows the mode-resolved e-ph scattering rates as a function of hole energy for the 12 intermolecular phonon modes, and Fig. 2.3(b) for selected intramolecular phonons. Note that the intermolecular phonons have either zero or very small minimum frequency since they correspond to transverse acoustic (TA) and longitudinal acoustic (LA) vibrations (modes 1−3) or other rigid vibrations or librations of the molecules (modes 4−12). By contrast, the intramolecular modes

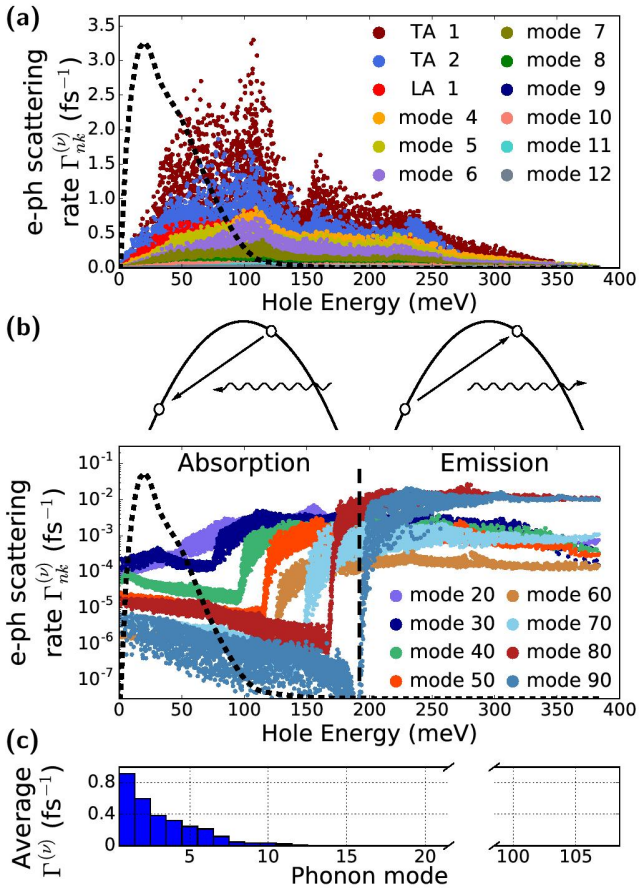

Figure 2.3: **Mode resolved hole-phonon scattering rates.** Mode resolved e-ph scattering rates, $\Gamma^{(\nu)}_{n\mathbf{k}}$, for (a) the 12 intermolecular phonon modes and (b) selected intramolecular phonon modes (note the y-axis log scale). Also sketched in (b) are the dominant e-ph scattering processes below and above the phonon emission threshold energy $\hbar\omega_0$, which is shown as a vertical dashed line for mode 90. The black dashed curve represents the integrand in Eq. (2.2), and shows that only hole states within a 50−100 meV energy window of the valence band maximum (VBM) contribute to the mobility. (c) Mode-resolved scattering rates averaged over the energy window contributing to the mobility. In all plots, the zero of the energy axis is the VBM, and the hole energy increases moving away from the VBM into the valence band.

20−90 in Fig. 2.3(b) possess much higher frequencies. The integrand of the mobility in Eq. (2.2) is also plotted in Figs. 2.3(a)−2.3(b) to highlight the energy window contributing to the mobility, which spans hole states within 50−100 meV of the VBM. In this energy window, the 12 intermolecular phonon modes exhibit much greater scattering rates than the intramolecular modes, due to reasons related to the e-ph scattering phase space that are examined next.

In the hole scattering rates of Eq. (2.1), the first term in square brackets corresponds

to phonon emission, and is proportional to the phonon population $N_{\nu\mathbf{q}}+1$ since $f_{m\mathbf{k+q}} \approx 0$ for holes in our chosen temperature range. The term in the second square brackets is the phonon absorption rate, which is proportional to $N_{\nu\mathbf{q}}$. Since the intermolecular phonon modes 1−12 have a zero or small minimum energy, intermolecular phonon absorption and emission processes are *both* active at all hole energies. Their scattering rate decreases monotonically with phonon energy (and thus with mode number, since the modes are numbered in order of increasing energy). Similarly to simple metals and nonpolar inorganic semiconductors, the main sources of scattering are acoustic modes, with smaller contributions from other molecular rigid vibrations and librations (modes 4−12). This result is further illustrated in Fig. 2.3(c), where the average $\Gamma^{(\nu)}_{n\mathbf{k}}$ over the 100 meV energy window of relevance for the mobility is given for each phonon mode. The dominant role of intermolecular modes is consistent with the charge hopping intuition that rigid molecular vibrations mainly affect charge transport in organic materials. However, in our band picture based on phonon emission and absorption events, the origin of this behavior can be attributed to the phase space rather than the strength of the e-ph coupling per se, as further discussed below.

The effect of intramolecular phonons on the mobility is more subtle. Figure 2.3(b) shows that the e-ph scattering rates for these modes exhibit a trend with two plateaus as a function of hole energy. As explained next, the plateau at low hole energy corresponds to phonon absorption, and the one at higher hole energy to phonon emission. Consider an intramolecular phonon with minimum energy $\hbar\omega_0$. Due to energy conservation, a hole in the valence band can emit such a phonon only at hole energy higher than $\hbar\omega_0$. At hole energies below this threshold, only phonon absorption is possible, with a rate proportional to the phonon occupation $N_{\nu\mathbf{q}} \propto e^{-\hbar\omega_0/k_BT}$, which is much smaller than 1 at room temperature in naphthalene since most intramolecular modes have minimum energies $\hbar\omega_0 \approx 50-200$ meV. Therefore, the plateau at hole energies below $\hbar\omega_0$ is associated with a small intramolecular phonon absorption rate, and it spans the entire energy window contributing to the mobility.

At hole energies above $\hbar\omega_0$, the phase space for e-ph scattering increases dramatically since holes can emit intramolecular phonons, with a rate proportional to $N_{\nu\mathbf{q}}+1$, and thus much greater than the absorption rate. Opening this phonon emission channel leads to an increase of the e-ph scattering rates by several orders of magnitude, but this increase occurs outside the energy window of relevance for charge transport

due to the high energy of intramolecular phonons in naphthalene. These trends are expected to be general in organic crystals, since the dominant presence of hydrogen, carbon, and other light elements makes their intramolecular phonon energies much greater than $k_B T$. Interestingly, in organic molecules containing heavy atoms, which introduce low-frequency intramolecular vibrations, a contribution to transport from intramolecular phonons is expected.

In short, the two-plateau structure for intramolecular mode e-ph scattering is such that only the small rate for thermally activated phonon absorption falls in the energy range of interest for transport. Therefore the mobility is controlled by low-frequency intermolecular vibrations. However, note that intramolecular phonons are expected to dominate carrier dynamics at a higher hole energy above the phonon emission threshold, where their combined scattering rate overwhelms that from the (much fewer) intermolecular modes. This analysis shows that intramolecular phonons play an essential role in the dynamics of excited carriers [32–34, 60] in organic semiconductors.

2.4 Discussion

While the phase space limits their scattering near the band edge, intramolecular phonons can couple strongly with holes at all energies, and in fact more strongly than intermolecular modes. To study this point, we compute the local e-ph coupling constants $g^{(\mathrm{loc})}_{\nu\mathbf{q}}$ between each phonon mode at the Brillouin zone center ($\mathbf{q} = 0$) and the HOMO Wannier function (WF) $w_{\mathbf{R}}(\mathbf{r})$:

$$g^{(\mathrm{loc})}_{\nu\mathbf{q}} = \sqrt{\frac{\hbar}{2\omega_{\nu\mathbf{q}}}} \langle w_{\mathbf{R}} | \Delta_{\nu\mathbf{q}} V^{\mathrm{KS}} | w_{\mathbf{R}} \rangle, \tag{2.4}$$

where $\mathbf{R}$ is the WF center, and the change in Kohn-Sham potential $\Delta_{\nu\mathbf{q}} V^{\mathrm{KS}}$ arises from the atomic displacements $e_{\kappa\alpha,\nu}$ of each atom κ (with mass M_κ) along all cartesian directions α due to the phonon mode ν,

$$\Delta_{\nu\mathbf{q}} V^{\mathrm{KS}} = e^{i\mathbf{q}\cdot\mathbf{r}} \sum_{\kappa\alpha} \frac{1}{\sqrt{M_\kappa}} e_{\kappa\alpha,\nu} \partial_{\kappa\alpha,\mathbf{q}} V^{\mathrm{KS}}. \tag{2.5}$$

The absolute values of these local e-ph coupling constants are shown in Fig. 2.4(a) for all 108 phonon modes. Contrary to intuition, the strongest e-ph coupling to the HOMO hole state is not with the intermolecular modes that control transport. Rather, specific high-frequency intramolecular phonons (in particular, modes 79–88) exhibit the strongest coupling to holes. To understand this result, we plot quantities entering

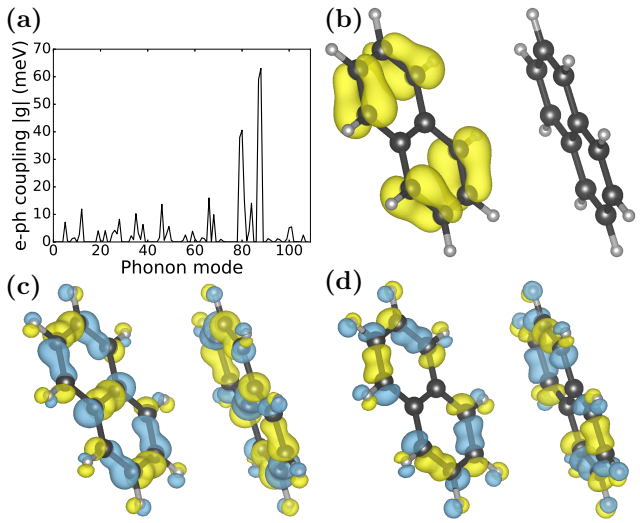

Figure 2.4: **Visualization of Wannier function and phonon potential perturbation.** (a) The absolute value of the local coupling constant [see Eq. (2.4)] between each of the phonon modes and the HOMO Wannier function. (b) The square of the HOMO Wannier function. The potential perturbation $\Delta_{\nu\mathbf{q}}V^{\mathrm{KS}}$ at $\mathbf{q} = 0$ is shown for (c) mode $\nu = 88$ and (d) mode $\nu = 89$. These modes correspond to the peak (mode 88) and sudden drop (mode 89) in e-ph coupling in (a). In panels (b)−(d), yellow is used for positive and blue for negative isosurfaces.

the local e-ph coupling in Eq. (2.4), namely the square of the HOMO WF, $|w_{\mathbf{R}}(\mathbf{r})|^2$, and the perturbation potential $\Delta_{\nu\mathbf{q}}V^{\mathrm{KS}}$ due to the atomic motions associated with the given mode.

Figure 2.4(b) shows the square of the HOMO WF orbital, $|w_{\mathbf{R}}(\mathbf{r})|^2$; the perturbation potential $\Delta_{\nu\mathbf{q}}V^{\mathrm{KS}}(\mathbf{r})$ at $\mathbf{q} = 0$ is shown in Fig. 2.4(c) for mode 88 and Fig. 2.4(d) for mode 89, which are, respectively, cases of maximally strong and weak e-ph coupling. We find that e-ph coupling is maximal for mode 88 due to the strong overlap between the square of the HOMO WF and the perturbation potential, and the fact that both quantities possess the same sign over most of the molecule, so that no cancellations occur in the real-space integral in Eq. (2.4). By contrast, the symmetry of mode 89 is such that its perturbation potential $\Delta_{\nu\mathbf{q}}V^{\mathrm{KS}}(\mathbf{r})$ alternates positive and negative lobes at bonds where the square of the HOMO WF is large. As a result, the *integrand* $|w_{\mathbf{R}}(\mathbf{r})|^2 \cdot \Delta_{\nu\mathbf{q}}V^{\mathrm{KS}}(\mathbf{r})$ in Eq. 2.4 is positive for two bonds and negative (and roughly equal in absolute value) for the other two bonds, thus leading to a small integral over the entire molecule in Eq. 2.4. This cancellation results in a small e-ph coupling for mode 89. Other phonon modes are either associated with perturbation potentials with small overlap with the square of the HOMO WF, as is

the case for modes in which only the hydrogen atoms vibrate, or with perturbations that are out of phase with the square of the HOMO WF, similar to the case of mode 89. This analysis shows that the atomic displacements and mode symmetry critically determine the *e*-ph coupling of intramolecular modes, which can be much stronger than that of intermolecular modes due to the large spatial overlap between the hole charge density and the intramolecular mode perturbation.

Lastly, we comment on the fact that our computed phonon-limited mobility is smaller than the experimental result. Due to the presence of impurities and defects in real samples, our calculation is expected to provide an upper bound to the mobility, and thus to slightly overestimate its experimental value, consistent with our recent results for inorganic crystals [32]. The reason why our result is lower than the experiment is unclear, but a possible cause is the neglect of nonadiabatic effects.

Our method employs only the lowest Born–Oppenheimer potential energy surface (PES), since the *e*-ph perturbation potential is computed using DFPT. However, an insight from nonadiabatic surface hopping calculations [8, 61] is that several PESs can lie close in energy in organic crystals, and including their contributions to charge transport may increase the mobility. The impact of such nonadiabatic effects on the mobility within the band theory framework used here deserves further investigation. Nonetheless, the fact that our results underestimate the measured mobility is important as it further supports the conclusion in Ref. [37] that hole charge carriers in naphthalene crystals are weakly coupled to phonons, so that transport occurs in the bandlike regime studied here. In fact, polaronic effects resulting from strong *e*-ph coupling (beyond the lowest order employed here) would further suppress carrier transport by increasing the scattering rates and effective masses [62], thus reducing the mobility.

2.5 Conclusion

In summary, we compute with quantitative accuracy the hole mobility and its temperature dependence in naphthalene, dramatically improving the agreement with experiment compared to previous efforts using band theory to study charge transport in organic crystals. Our results show that *ab initio* approaches based on band theory and many-body perturbation theory are well equipped to compute charge transport in organic semiconductors. They can provide an accuracy at least as satisfactory as widespread quantum chemistry methods based on charge hopping, as well as insight into the role of different phonon modes. Our work sets the stage for at-

tempting higher-order corrections or diagram resummations in the e-ph perturbation to access the strong e-ph coupling regime typical of polaron transport.

2.6 Supplementary Materials

Band structure and phonon dispersion

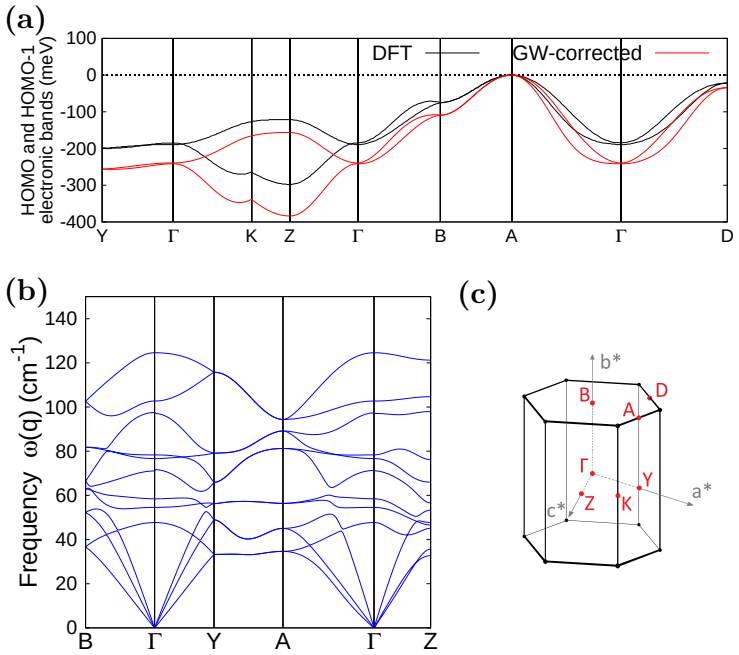

Figure 2.5: **Naphthalene band structures and phonon dispersions.** Band structures and phonon dispersions of naphthalene crystal, for the structure used at 300 K. (a) The HOMO and HOMO−1 electronic bands, where black is used for the DFT bands and red for the bands with the GW correction. (b) Dispersion of the 12 intermolecular phonon modes. (c) Sketch of the first Brillouin zone.

Results with different van der Waals correction

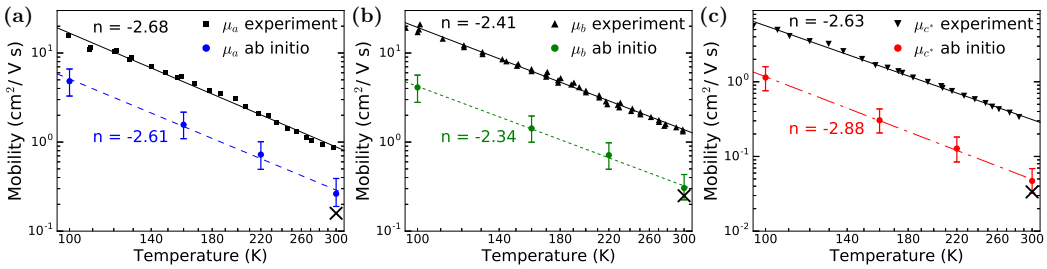

Figure 2.6: **Calculated hole mobility using the TS-vdW correction.** The mobility at 300 K obtained using a structure relaxed with the TS-vdW correction is shown with black crosses. The values fall within the error bars.

Comparison of calculated phonon dispersions with experiment

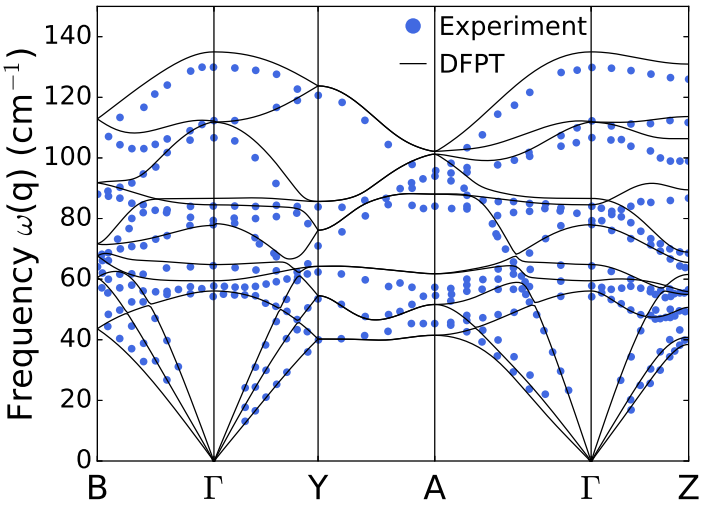

Figure 2.7: **Comparison of calculated phonon dispersions with experiment.** Calculated dispersion of the 12 intermolecular phonon modes for perdeuterated naphthalene, with lattice constants taken from Refs. [52, 63]. The markers are the experimental data at 6 K from Ref. [64].

Refined interpolation and its impact on the calculated hole mobility

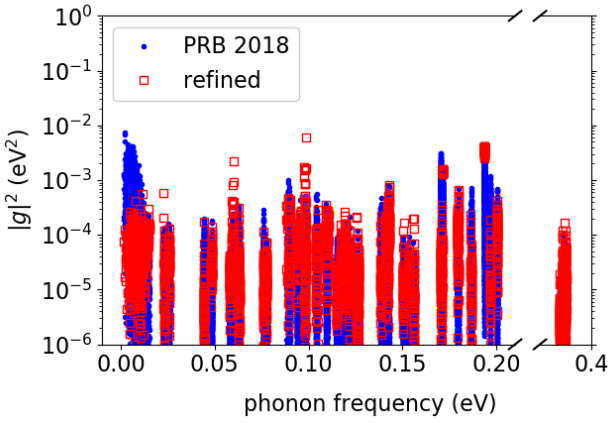

Figure 2.8: **Coupling constants from refined interpolation.** Comparison of the coupling constants used in Chapter 2 and those from a refined interpolation scheme developed in our recent work. The original interpolation overestimates the coupling strength for low-frequency phonons, and hence exaggerates the scattering rates from intermolecular phonons.

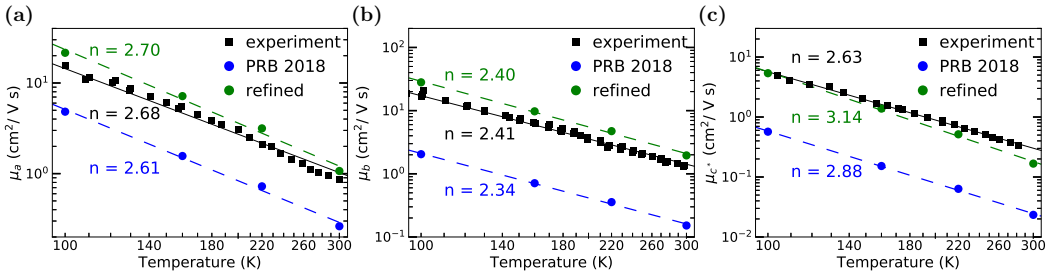

Figure 2.9: **Hole mobility calculated with refined coupling constants.** Calculated hole mobility using the refined coupling constants. The result is in excellent agreement with experiment, indicating that the discrepancy is mainly due to the improperly-interpolated g for low-frequency phonons.

In our recent work, the open problem that the calculated phonon-limited hole mobility is lower than experiment by a factor of 3–4 is resolved. Upon refining our results, we found that the commonly-adopted interpolation scheme cannot properly handle a $\mathbf{q}$-point grid that is as coarse as $2 \times 4 \times 2$, leading to a large overestimation on the coupling strength with low-frequency phonons (see Fig. 2.8). Improvements in the acoustic sum rules and Wigner-Seitz cell sampling used for e-ph interpolation [55] have allowed us to refine the results and obtain accurate interpolated e-ph coupling constants that match the DFPT benchmark at all grid points. The overestimation of e-ph coupling with low-frequency modes that affected our results in Ref. [65] artificially increases the scattering rate due to intermolecular phonons, resulting in a lower mobility. Using a refined interpolation scheme [55], we can bring the calculated hole mobility to a value just slightly higher than experiment (see Fig. 2.9). This result is consistent with our expectation, and shows that transport of hole carriers in naphthalene can be fully explained by band theory.

References

[1] M. Muccini, Nat. Mater. **5**, 605–613 (2006).

[2] V. A. Dediu, L. E. Hueso, I. Bergenti, and C. Taliani, Nat. Mater. **8**, 707–716 (2009).

[3] A. L. Briseno, S. C. B. Mannsfeld, M. M. Ling, S. Liu, R. J. Tseng, C. Reese, M. E. Roberts, Y. Yang, F. Wudl, and Z. Bao, Nature **444**, 913–917 (2006).

[4] T. Sekitani, U. Zschieschang, H. Klauk, and T. Someya, Nat. Mater. **9**, 1015–1022 (2010).

[5] M. Kitamura, T. Imada, and Y. Arakawa, Appl. Phys. Lett. **83**, 3410–3412 (2003).

[6] N. Karl, *"Organic semiconductors, Landolt-Börnstein Numerical Data and Functional Relationships in Science and Technology New Series - Group III Crystal and Solid State Physics"*, Vol. 17i (Springer-Verlag Berlin-Heidelberg, 1985).

[7] L. B. Schein, C. B. Duke, and A. R. McGhie, Phys. Rev. Lett. **40**, 197–200 (1978).

[8] H. Oberhofer, K. Reuter, and J. Blumberger, Chem. Rev. **117**, 10319–10357 (2017).

[9] S. Canola and F. Negri, Phys. Chem. Chem. Phys. **16**, 21550–21558 (2014).

[10] A. Troisi, Adv. Mater. **19**, 2000–2004 (2007).

[11] J. C. Tully, J. Chem. Phys. **93**, 1061–1071 (1990).

[12] L. Wang and D. Beljonne, J. Phys. Chem. Lett. **4**, 1888–1894 (2013).

[13] A. Troisi and G. Orlandi, Phys. Rev. Lett. **96**, 086601 (2006).

[14] S. Fratini, D. Mayou, and S. Ciuchi, Adv. Funct. Mater. **26**, 2292–2315 (2016).

[15] S. Fratini, S. Ciuchi, D. Mayou, G. T. de Laissardiére, and A. Troisi, Nat. Mater. **16**, 998–1002 (2017).

[16] R. Silbey and R. W. Munn, J. Chem. Phys. **72**, 2763–2773 (1980).

[17] V. M. Kenkre, J. D. Andersen, D. H. Dunlap, and C. B. Duke, Phys. Rev. Lett. **62**, 1165–1168 (1989).

[18] K. Hannewald and P. A. Bobbert, Phys. Rev. B **69**, 075212 (2004).

[19] K. Hannewald and P. A. Bobbert, Appl. Phys. Lett. **85**, 1535–1537 (2004).

[20] F. Ortmann, F. Bechstedt, and K. Hannewald, Phys. Rev. B **79**, 235206 (2009).

[21] F. Ortmann, F. Bechstedt, and K. Hannewald, New J. Phys. **12**, 023011 (2010).

[22] L. J. Wang, Q. Peng, Q. K. Li, and Z. Shuai, J. Chem. Phys. **127**, 044506 (2007).

[23] L. Tang, M. Long, D. Wang, and Z. Shuai, Sci. China Ser. B-Chem. **52**, 1646–1652 (2009).

[24] Y. C. Cheng, R. J. Silbey, D. A. da Silva Filho, J. P. Calbert, J. Cornil, and J. L. Brédas, J. Chem. Phys. **118**, 3764–3774 (2003).

[25] L. Giuggioli, J. D. Andersen, and V. M. Kenkre, Phys. Rev. B **67**, 045110 (2003).

[26] O. Ostroverkhova, D. G. Cooke, F. A. Hegmann, J. E. Anthony, V. Podzorov, M. E. Gershenson, O. D. Jurchescu, and T. T. M. Palstra, Appl. Phys. Lett. **88**, 162101 (2006).

[27] D. Moses, C. Soci, X. Chi, and A. P. Ramirez, Phys. Rev. Lett. **97**, 067401 (2006).

[28] Z. Q. Li, V. Podzorov, N. Sai, M. C. Martin, M. E. Gershenson, M. Di Ventra, and D. N. Basov, Phys. Rev. Lett. **99**, 016403 (2007).

[29] S. Machida, Y. Nakayama, S. Duhm, Q. Xin, A. Funakoshi, N. Ogawa, S. Kera, N. Ueno, and H. Ishii, Phys. Rev. Lett. **104**, 156401 (2010).

[30] H. Kobayashi, N. Kobayashi, S. Hosoi, N. Koshitani, D. Murakami, R. Shirasawa, Y. Kudo, D. Hobara, Y. Tokita, and M. Itabashi, J. Chem. Phys. **139**, 014707 (2013).

[31] J. I. Mustafa, M. Bernardi, J. B. Neaton, and S. G. Louie, Phys. Rev. B **94**, 155105 (2016).

[32] J.-J. Zhou and M. Bernardi, Phys. Rev. B **94**, 201201 (2016).

[33] V. A. Jhalani, J.-J. Zhou, and M. Bernardi, Nano Lett. **17**, 5012–5019 (2017).

[34] M. Bernardi, Eur. Phys. J. B **89**, 239 (2016).

[35] M. Casula, M. Calandra, and F. Mauri, Phys. Rev. B **86**, 075445 (2012).

[36] A. Girlando, L. Grisanti, M. Masino, I. Bilotti, A. Brillante, R. G. Della Valle, and E. Venuti, Phys. Rev. B **82**, 035208 (2010).

[37] N. Vukmirović, C. Bruder, and V. M. Stojanović, Phys. Rev. Lett. **109**, 126407 (2012).

[38] P. Giannozzi et al., J. Phys. Condens. Matter **21**, 395502 (2009).

[39] J. P. Perdew, K. Burke, and M. Ernzerhof, Phys. Rev. Lett. **77**, 3865–3868 (1996).

[40] N. Troullier and J. L. Martins, Phys. Rev. B **43**, 1993–2006 (1991).

[41] M. van Setten, M. Giantomassi, E. Bousquet, M. Verstraete, D. Hamann, X. Gonze, and G.-M. Rignanese, Comput. Phys. Commun. **226**, 39–54 (2018).

[42] C. P. Brock and J. D. Dunitz, Acta Cryst. B **38**, 2218–2228 (1982).

[43] S. Gražulis, A. Daškevič, A. Merkys, D. Chateigner, L. Lutterotti, M. Quirós, N. R. Serebryanaya, P. Moeck, R. T. Downs, and A. Le Bail, Nucleic Acids Res. **40**, D420–D427 (2012).

[44] S. Gražulis, D. Chateigner, R. T. Downs, A. F. T. Yokochi, M. Quirós, L. Lutterotti, E. Manakova, J. Butkus, P. Moeck, and A. Le Bail, J. Appl. Cryst. **42**, 726–729 (2009).

[45] S. Grimme, J. Comput. Chem. **27**, 1787–1799 (2006).

[46] V. Barone, M. Casarin, D. Forrer, M. Pavone, M. Sambi, and A. Vittadini, J. Comput. Chem. **30**, 934–939 (2009).

[47] T. Rangel, K. Berland, S. Sharifzadeh, F. Brown-Altvater, K. Lee, P. Hyldgaard, L. Kronik, and J. B. Neaton, Phys. Rev. B **93**, 115206 (2016).

[48] A. Marini, C. Hogan, M. Grüning, and D. Varsano, Comput. Phys. Commun. **180**, 1392–1403 (2009).

[49] A. A. Mostofi, J. R. Yates, G. Pizzi, Y.-S. Lee, I. Souza, D. Vanderbilt, and N. Marzari, Comput. Phys. Commun. **185**, 2309–2310 (2014).

[50] L. A. Agapito, M. Fornari, D. Ceresoli, A. Ferretti, S. Curtarolo, and M. B. Nardelli, Phys. Rev. B **93**, 125137 (2016).

[51] S. Baroni, S. de Gironcoli, A. Dal Corso, and P. Giannozzi, Rev. Mod. Phys. **73**, 515–562 (2001).

[52] F. Brown-Altvater, T. Rangel, and J. B. Neaton, Phys. Rev. B **93**, 195206 (2016).

[53] S. Poncé, E. Margine, C. Verdi, and F. Giustino, Comput. Phys. Commun. **209**, 116–133 (2016).

[54] F. Giustino, M. L. Cohen, and S. G. Louie, Phys. Rev. B **76**, 165108 (2007).

[55] J.-J. Zhou, J. Park, I.-T. Lu, I. Maliyov, X. Tong, and M. Bernardi, Preprint at arXiv:2002.02045 (2020).

[56] G. Pizzi, D. Volja, B. Kozinsky, M. Fornari, and N. Marzari, Comput. Phys. Commun. **185**, 422–429 (2014).

[57] P. E. Blöchl, O. Jepsen, and O. K. Andersen, Phys. Rev. B **49**, 16223–16233 (1994).

[58] J. Hoja, A. M. Reilly, and A. Tkatchenko, Wiley Interdiscip. Rev. Comput. Mol. Sci. **7**, 1294 (2017).

[59] A. M. Reilly and A. Tkatchenko, J. Chem. Phys. **139**, 024705 (2013).

[60] M. Bernardi, D. Vigil-Fowler, J. Lischner, J. B. Neaton, and S. G. Louie, Phys. Rev. Lett. **112**, 257402 (2014).

[61] B. F. E. Curchod, U. Rothlisberger, and I. Tavernelli, ChemPhysChem **14**, 1314–1340 (2013).

[62] G. D. Mahan, *"Many-Particle Physics"*, 3rd ed. (Springer, 2000).

[63] I. R. Thomas, I. J. Bruno, J. C. Cole, C. F. Macrae, E. Pidcock, and P. A. Wood, J. Appl. Crystallogr. **43**, 362–366 (2010).

[64] I. Natkaniec, E. L. Bokhenkov, B. Dorner, J. Kalus, G. A. Mackenzie, G. S. Pawley, U. Schmelzer, and E. F. Sheka, J. Phys. C **13**, 4265 (1980).

[65] N.-E. Lee, J.-J. Zhou, L. A. Agapito, and M. Bernardi, Phys. Rev. B **97**, 115203 (2018).

Chapter 3

ELECTRON-TWO-PHONON SCATTERING FROM NEXT-TO-LEADING ORDER PERTURBATION THEORY

This chapter is a slightly modified version of the published article:

N.-E. Lee, J.-J. Zhou, H.-Y. Chen, and M. Bernardi, *"Ab initio electron-two-phonon scattering in GaAs from next-to-leading order perturbation theory"*, Nat. Commun. 11, 1607 (2020).

3.1 Introduction

Electron-phonon (*e*-ph) interactions are essential to understanding electrical transport, nonequilibrium dynamics, and superconductivity. Using density functional theory (DFT) and related methods, it has become possible to compute *e*-ph interactions from first principles, and use them to predict the carrier scattering rates and mobilities, both in simple and in complex materials with up to tens of atoms in the unit cell [1–11]. In the typical workflow, one takes into account only the leading-order *e*-ph scattering processes, which involve scattering of the carriers with one phonon. Nearly all *ab initio* work to date has relied on such leading-order perturbation theory, tacitly neglecting higher-order *e*-ph processes.

Yet many compounds, including polar semiconductors, oxides and organic crystals, exhibit *e*-ph interactions that cannot be treated with lowest-order perturbation theory. Polar materials are a paradigmatic case in which *e*-ph interactions due to polar optical modes – in particular, the longitudinal optical (LO) mode – are long-range [12, 13], which can lead to higher-order *e*-ph scattering and polaron formation. In weakly polar materials, such as III-V and II-VI semiconductors and high-mobility oxides, one expects that perturbation theory is still valid, but that higher-order *e*-ph processes are significant and need to be included.

Studies of second and even third-order *e*-ph processes in semiconductors exist [14–19], but they are limited to simplified models, restricted to the conduction band minimum, or only valid at zero temperature, and are therefore inadequate for quantitative predictions. In first-principles *e*-ph and charge transport calculations, next-to-leading order effects have been typically assumed to be negligible, even though their

contributions have been estimated to be important using simplified models [15–17, 20, 21]. In materials with intermediate or strong e-ph coupling, which typically include oxides with low room-temperature mobility and highly polar compounds (e.g., alkali halides), the e-ph interactions can lead to regimes beyond the reach of perturbation theory, including the formation of polarons [22]. This coupling regime has been investigated with diagram-resummation techniques such as the cumulant method, both analytically [23] and more recently *ab initio* [24–26].

Higher-order processes are generally important in quantum field theories of condensed matter. An example are light-matter interactions, where phonon-assisted [27] and two-photon [28, 29] absorption have been studied extensively. Even calculations in quantum electrodynamics beyond the leading order can provide important lessons – for example, higher-order corrections are essential to accurately predict large-angle Bhabha scattering in electron-positron collisions [30], and calculations up to the tenth order have been carried out to compute the magnetic moment of the electron [31].

However, it is a daunting task to systematically go beyond the leading order due to the rapid increase in the number of Feynman diagrams and their computational complexity. For e-ph interactions, the next-to-leading order involves electron scattering events with two phonons, which requires computationally challenging Brillouin zone integrals over two crystal momenta. This computational complexity has hampered next-to-leading order e-ph calculations for decades [14], and the relevant next-to-leading order diagrams (see Fig. 3.1) have not yet been computed numerically from first principles.

Here we formulate and compute from first principles next-to-leading order e-ph interactions, focusing on electron scattering processes involving two phonons (hereafter denoted as 2ph processes). We compute and analyze their contributions to the

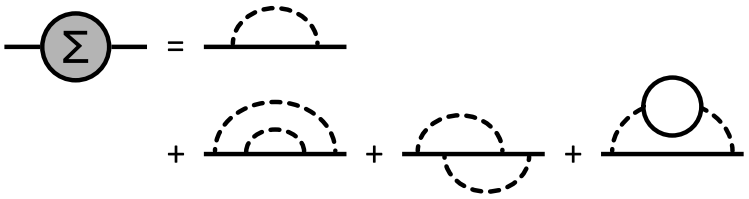

Figure 3.1: **Next-to-leading order self-energy diagrams.** Diagrams for the e-ph self-energy up to $O(g^4)$, where g is the e-ph coupling constant. The first two diagrams in the second row contribute to the two-phonon scattering processes.

e-ph scattering rates, using as an ideal case study a weakly polar semiconductor, GaAs. We find that the 2ph scattering rates are surprisingly large and comparable in magnitude to the lowest order rates due to one-phonon (1ph) processes. Our analysis shows that the relative importance of the 2ph contributions is nearly temperature independent at 200−400 K, and rationalizes the peculiar energy dependence of the 2ph processes. The results are sensitive to the lifetimes of the intermediate states, which need to be included to avoid divergences due to resonance effects; we develop a self-consistent scheme to overcome this challenge. The 2ph processes are also shown to play an important role in accurately predicting the electron mobility in GaAs. We formulate and iteratively solve a linearized Boltzmann transport equation (BTE) that includes the 2ph processes, showing that this level of theory can correct the discrepancy with experiment of the mobility predicted with the BTE including only 1ph processes. Our work proposes an approach for systematically improving the accuracy of *ab initio* *e*-ph calculations beyond the leading order. While this method is broadly applicable, it is particularly well-suited for weakly polar (III-V and II-VI) semiconductors and high-mobility oxides, in which the weak polaron effects can be treated perturbatively.

3.2 Results

Two-phonon processes and their scattering rates

We use the Matsubara frequency sum technique [32] to derive the electron self-energy due to *e*-ph interactions up to $O(g^4)$ (see Fig. 3.1), where g is the *e*-ph coupling constant; our treatment focuses on computing the imaginary part of the self-energy and the related 2ph scattering rates. The derivations are lengthy and tedious, and are given in detail in Appendix A.

All 2ph processes considered in this work consist of two consecutive 1ph scattering events [14], as we show in Fig. 3.2. They include processes in which the electron absorbs one phonon and emits another phonon, or vice versa (both processes are denoted as 1e1a), and processes in which the electron emits or absorbs two phonons (denoted as 2e and 2a, respectively). The intermediate electronic state accessed following the first scattering event is associated a virtual electron that cannot be observed and whose energy can take any value. Processes are defined as *on shell* when the intermediate electron energy equals its band electron energy, and *off shell* when it does not (see Fig. 3.2). As we discuss below, on-shell processes lead to divergent integrals, which are regularized by including the intermediate electron lifetime.

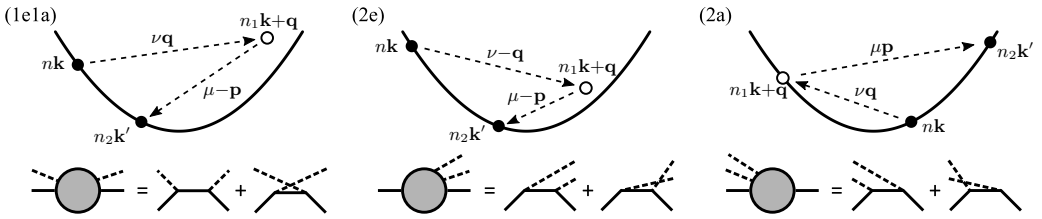

Figure 3.2: **Electron-two-phonon scattering processes.** Two-phonon scattering processes considered in this work, including one-phonon absorption plus one-phonon emission (left panel, labelled 1e1a), two-phonon emission (middle panel, labelled 2e), and two-phonon absorption (right panel, labelled 2a). Each of these three processes comprises two interfering scattering channels, only one of which is shown in the band structure schematics. The lower panels show the corresponding Feynman diagrams with two external phonon lines. Note that the intermediate state does not need to be on-shell; of the three processes shown here, only the 2a is on-shell.

The key result of our analysis is the scattering rate due to the 2ph processes, $\Gamma^{(2\mathrm{ph})}_{n\mathbf{k}}$, for an electronic state with band index n and crystal momentum $\mathbf{k}$, which can be expressed as (see Appendix A for detail derivation)

$$\Gamma^{(2\mathrm{ph})}_{n\mathbf{k}} = \frac{2\pi}{\hbar}\frac{1}{N_\Omega^2}\sum_{n_2}\sum_{\nu\mathbf{q}}\sum_{\mu\mathbf{p}}\left[\,\widetilde{\Gamma}^{(1\mathrm{e}1\mathrm{a})} + \widetilde{\Gamma}^{(2\mathrm{e})} + \widetilde{\Gamma}^{(2\mathrm{a})}\right], \tag{3.1}$$

where the process-resolved 2ph scattering rates $\widetilde{\Gamma}^{(\mathrm{i})}$ (i = 1e1a, 2e or 2a) depend on the two phonon momenta $\mathbf{q}$ and $\mathbf{p}$ and their respective mode indexes ν and μ, and n_2 is the band index of the final electronic state, whose momentum is fixed to $\mathbf{k}' \equiv \mathbf{k}+\mathbf{q}+\mathbf{p}$ by momentum conservation; to correctly normalize the sum, we divide it by N_Ω^2, the number of points sampled in the ($\mathbf{q}$, $\mathbf{p}$) space. The process-resolved 2ph scattering rates are defined as

$$\widetilde{\Gamma}^{(\mathrm{i})} = \gamma^{(\mathrm{i})}\,\delta(\varepsilon_{n\mathbf{k}} - \varepsilon_{n_2\mathbf{k}'} - \alpha^{(\mathrm{i})}_{\mathbf{p}}\omega_{\mu\mathbf{p}} - \alpha^{(\mathrm{i})}_{\mathbf{q}}\omega_{\nu\mathbf{q}}), \tag{3.2}$$

where ε are electron energies relative to the chemical potential, and ω are phonon energies; the delta function imposes energy conservation, and the constants α for each process are defined as

$$\begin{aligned} \alpha^{(1\mathrm{e}1\mathrm{a})}_{\mathbf{p}} &= \;\;1, \;\; \alpha^{(2\mathrm{e})}_{\mathbf{p}} = 1, \;\; \alpha^{(2\mathrm{a})}_{\mathbf{p}} = -1, \\ \alpha^{(1\mathrm{e}1\mathrm{a})}_{\mathbf{q}} &= -1, \;\; \alpha^{(2\mathrm{e})}_{\mathbf{q}} = 1, \;\; \alpha^{(2\mathrm{a})}_{\mathbf{q}} = -1. \end{aligned}$$

The square amplitudes of the three processes are

$$\gamma^{(\mathrm{i})} = \;A^{(\mathrm{i})}\left|\sum_{n_1}\left(\frac{g_{n_1 n\nu}(\mathbf{k},\mathbf{q})\,g_{n_2 n_1\mu}(\mathbf{k}+\mathbf{q},\mathbf{p})}{\varepsilon_{n_2\mathbf{k}'} - \varepsilon_{n_1\mathbf{k}+\mathbf{q}} + \alpha^{(\mathrm{i})}_{\mathbf{p}}\omega_{\mu\mathbf{p}} + \mathrm{i}\,\eta - \Sigma_{n_1\mathbf{k}+\mathbf{q}}}\right.\right. \tag{3.3}$$

$$+ \frac{g_{n_1 n\mu}(\mathbf{k},\mathbf{p}) g_{n_2 n_1 \nu}(\mathbf{k}+\mathbf{p},\mathbf{q})}{\varepsilon_{n_2\mathbf{k}'} - \varepsilon_{n_1\mathbf{k}+\mathbf{p}} + \alpha^{(\mathrm{i})}_{\mathbf{q}} \omega_{\nu\mathbf{q}} + \mathrm{i}\,\eta - \Sigma_{n_1\mathbf{k}+\mathbf{p}}} \Bigg)\Bigg|^2 ,$$

where n_1 is the band index and Σ the self-energy of the intermediate electronic state, and η is a positive infinitesimal. The prefactors $A^{(\mathrm{i})}$ contain the thermal occupation numbers of electrons and phonons (denoted by f and N, respectively) and are defined as:

$$\begin{aligned} A^{(1\mathrm{e}1\mathrm{a})} &= N_{\nu\mathbf{q}} + N_{\nu\mathbf{q}} N_{\mu\mathbf{p}} + N_{\mu\mathbf{p}} f_{n_2\mathbf{k}'} - N_{\nu\mathbf{q}} f_{n_2\mathbf{k}'}, \\ A^{(2\mathrm{e})} &= \frac{1}{2}\left[(1+N_{\nu\mathbf{q}})(1+N_{\mu\mathbf{p}} - f_{n_2\mathbf{k}'}) - N_{\mu\mathbf{p}} f_{n_2\mathbf{k}'}\right], \\ A^{(2\mathrm{a})} &= \frac{1}{2}\left[N_{\nu\mathbf{q}}(N_{\mu\mathbf{p}} + f_{n_2\mathbf{k}'}) + (1+N_{\mu\mathbf{p}}) f_{n_2\mathbf{k}'}\right]. \end{aligned} \tag{3.4}$$

Let us examine the process amplitudes in Eq. (3.3). Since all three processes have similar expressions, we focus on a 1e1a process in which the electron absorbs one phonon and then emits another as an example, though our considerations are general. In this process, which is shown schematically in Fig. 3.3, an electron first absorbs a phonon with energy $\omega_{\nu\mathbf{q}}$, transitioning to an intermediate state $|n_1\mathbf{k}+\mathbf{q}\rangle$ with energy $E = \varepsilon_{n\mathbf{k}} + \omega_{\nu\mathbf{q}}$, and then emits a phonon with energy $\omega_{\mu\mathbf{p}}$, reaching the final state with energy $\varepsilon_{n_2\mathbf{k}'}$. Note that the energy E of the intermediate (virtual) electron does not need to match its band energy $\varepsilon_{n_1\mathbf{k}+\mathbf{q}}$. The amplitude for this process, from Eq. (3.3), reads

$$\frac{g_{n_1 n\nu}(\mathbf{k},\mathbf{q}) g_{n_2 n_1 \mu}(\mathbf{k}+\mathbf{q},\mathbf{p})}{\varepsilon_{n_2\mathbf{k}'} + \omega_{\mu\mathbf{p}} - \varepsilon_{n_1\mathbf{k}+\mathbf{q}} - \Sigma_{n_1\mathbf{k}+\mathbf{q}}}, \tag{3.5}$$

where we omitted the $\mathrm{i}\,\eta$ infinitesimal for clarity. This expression can be understood as follows: the two e-ph coupling constants are associated with each of the two consecutive 1ph scattering events, and the denominator is due to the propagator of

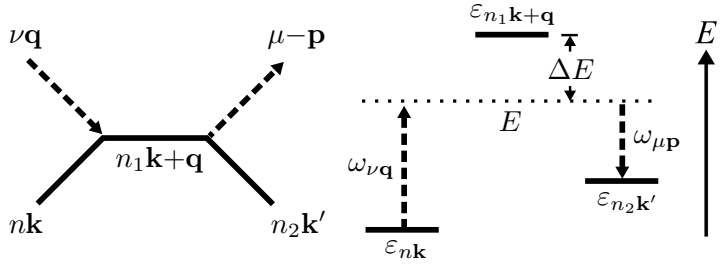

Figure 3.3: **Energetics of two-phonon processes.** The example 1e1a process discussed in the text, with its energetics shown on the right.

the intermediate electron, which is proportional to $1/(E - \varepsilon_{n_1\mathbf{k+q}} - \Sigma_{n_1\mathbf{k+q}})$. The amplitude of the 2ph process is thus inversely proportional to its off-shell extent, $\Delta E = E - \varepsilon_{n_1\mathbf{k+q}}$, implying that processes with large intermediate off-shell extents ΔE are unlikely to occur. In an on-shell 2ph process, E is equal (or very close) to the intermediate-state band energy $\varepsilon_{n_1\mathbf{k+q}}$, resulting in a small denominator $\Delta E \simeq 0$ and thus in a large amplitude. The inverse lifetime of the intermediate state, which is proportional to $\mathrm{Im}\Sigma_{n_1\mathbf{k+q}}$, prevents the on-shell process amplitude from diverging.

Numerical calculations and intermediate lifetime

We implement the expressions derived above in our in-house developed code, PERTURBO [33], and carry out first-principles calculations on GaAs (see Methods in Section 3.4). In our approach, we sum the 2ph scattering rates in Eq. (3.1) over all possible pairs of phonons, and thus include both on-shell and off-shell processes on the same footing. The treatment of the intermediate lifetimes in our implementation deserves a detailed discussion. When the intermediate state is on shell, the scattering process results in resonance effects, and as discussed above, the intermediate state lifetimes are crucial to prevent the 2ph scattering rates from diverging. Here and below, the intermediate state lifetime is defined as the inverse scattering rate of the intermediate state, which is obtained from the imaginary part of its self-energy as $2\,\mathrm{Im}\Sigma/\hbar$.

The 2ph scattering rates depend on the intermediate state self-energy, Σ in the denominator of Eq. (3.3), whose value needs to be chosen carefully. We neglect its real part, which only corrects the band structure and barely affects the 2ph calculation. The imaginary part of Σ includes in principle scattering effects from all possible sources. In practice, we approximate $\mathrm{Im}\Sigma$ with the total e-ph scattering rate, including both the lowest-order (1ph) rates and the 2ph rates, using $|\mathrm{Im}\Sigma| = \hbar/2[\Gamma^{(1\mathrm{ph})} + \Gamma^{(2\mathrm{ph})}]$, where $\Gamma^{(1\mathrm{ph})}$ is the usual 1ph scattering rate [4]. This approach makes Eq. (3.1) a self-consistent problem. We iterate Eq. (3.1) until the 2ph scattering rate equals the 2ph contribution to the intermediate state lifetime. In each iteration m, the lifetime is due to the sum of the lowest order plus the 2ph scattering rates at the previous iteration, namely, $|\mathrm{Im}\Sigma(m)| = \hbar/2\,[\Gamma^{(1\mathrm{ph})} + \Gamma^{(2\mathrm{ph})}(m-1)]$. The initial $\Gamma^{(2\mathrm{ph})}$ is set to zero, and the convergence process is performed separately at each temperature.

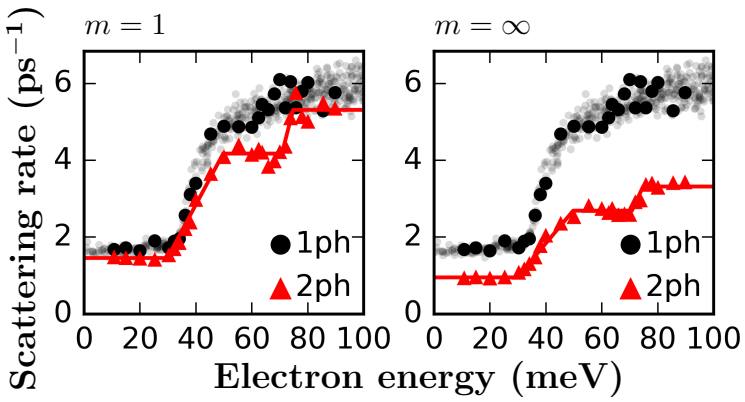

Figure 3.4: **Calculated two-phonon scattering rates.** Calculated 2ph scattering rates, $\Gamma^{(2\text{ph})}_{n\mathbf{k}}$ in Eq. (3.1), for electrons in GaAs at 300 K. The zero of the energy axis is the conduction band minimum. The left panel shows the first iteration, and the right the final result after converging the intermediate lifetime update procedure. The lowest-order (1ph) *e*-ph scattering rates are also given for comparison.

Analysis of the two-phonon scattering rates

Figure 3.4 shows the first iteration and the converged result for the 2ph scattering rates in GaAs at 300 K, for states near the bottom of the conduction band (see Methods in Section 3.4). In this energy range, the *e*-ph interactions in GaAs are dominated by the long-range field due to the LO mode [4], with nearly negligible contributions from all other phonon modes. The converged 2ph scattering rates are surprisingly large – they are smaller than the leading-order 1ph rate, thus justifying the perturbative approach, but they are nearly half the value of the 1ph rates at all energies. We find that the rainbow diagram (the first diagram in the second row of Fig. 3.1) provides the dominant contribution to the 2ph scattering rate, while the contribution from the vertex-correction diagram (the second diagram in the second row of Fig. 3.1) is negligible, in agreement with Migdal's theorem. Therefore, the lowest-order perturbation theory can capture only part of the dynamical processes due to the long-range *e*-ph interactions with the LO mode in GaAs. The results shown in Fig. 3.4 include only the dominant *e*-ph interaction with the LO mode, but we have verified that including all phonon modes gives nearly unchanged 2ph scattering rates in GaAs (see Fig. 3.9 in Supplementary Materials).

The 2ph scattering rate exhibits a trend as a function of energy with *three plateaus* near the bottom of the conduction band. This trend is a consequence of the dominant *e*-ph interactions in GaAs, which consist of absorption or emission events of LO phonons with energy $\omega_{\text{LO}} \approx 35$ meV. To rationalize the energy dependence of the 2ph

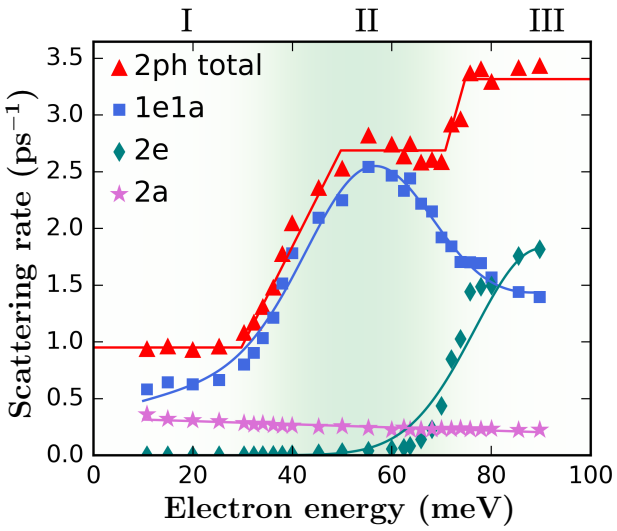

Figure 3.5: **Process-resolved two-phonon scattering rate.** Contributions to the 2ph scattering rate in GaAs at 300 K. The scattering rates of the 1e1a, 2e and 2a processes are shown, together with their sum, the total 2ph scattering rate. The solid curves fit the data and aid the visualization.

scattering rate, we define three energy regions, denoted as I, II, and III in Figs. 3.5 and 3.6, which correspond, respectively, to electron energies below ω_{LO}, between ω_{LO} and $2\omega_{\mathrm{LO}}$, and greater than $2\omega_{\mathrm{LO}}$ referenced to the conduction band minimum, which is taken hereafter to be the electron energy zero. The band structure in all three energy regions is nearly parabolic. We plot the rates of each of the 1e1a, 2e, and 2a process contributions in Fig. 3.5, and analyze the LO phonon emission and absorption processes in each energy region in Fig. 3.6.

In region I, the electrons possess an energy smaller than ω_{LO}, and thus cannot emit two LO phonons since this would require a final state in the band gap; the rate of the 2e process is accordingly negligible in region I. The 2a process in which the electron absorbs two LO phonons is active in region I, but it is thermally activated and weak at 300 K since $\omega_{\mathrm{LO}} \approx 35$ meV. The 2a process is nearly energy independent and weak throughout the three regions. The 1e1a process in which an electron absorbs and them emits an LO phonon is the dominant contribution in region I. Recall that the 2ph rate is inversely proportional to the square of the off-shell extent, ΔE^2. The 1e1a channel in which an LO phonon is first emitted and then absorbed is thus suppressed in region I since its intermediate state, resulting from one LO phonon emission, is always off-shell, as shown in Fig. 3.6(a).

In region II, the 1e1a scattering rate increases abruptly at energy ω_{LO} because the

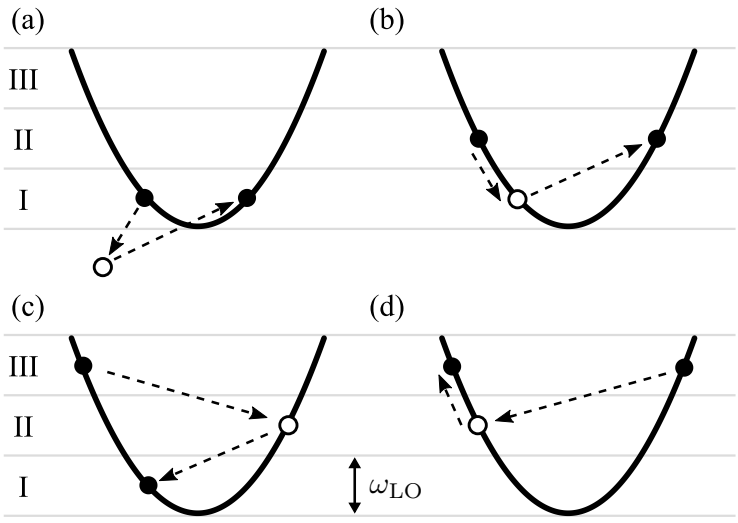

Figure 3.6: **Schematics of two-phonon processes.** Schematics of selected 2ph processes in energy region I (a), region II (b), and region III (c) and (d).

intermediate state following one LO phonon emission can be on-shell, as shown in Fig. 3.6(b). The rate of the 2e processes remains negligible in region II up to an energy of $2\omega_{\mathrm{LO}}$. In region III, the contribution from the 2e process increases dramatically since the electrons can emit two LO phonons and can transition to the bottom of the conduction band, as shown in Fig. 3.6(c). The 1e1a scattering rate drops from region II to region III due to subtle reasons related to the lifetime of the intermediate state. Recall that for the on-shell process, $\Delta E \simeq 0$ and the amplitude is proportional to the intermediate state lifetime [see Eq. (3.5)]. An electron in region II can emit a phonon, transition to an on-shell intermediate state in region I, and then absorb another phonon to transition to a final state, as shown in Fig. 3.6(b). Since the scattering rates for states in region I are considerably smaller than in the other two regions, the on-shell intermediate states have correspondingly long lifetimes, which gives a large amplitude to on-shell 1e1a processes in region II. On the other hand, the 1e1a processes for electrons in region III lead to intermediate states in region II or above [see Fig. 3.6(d)], which have much shorter lifetimes than in region I, resulting in a smaller 1e1a rate in region III compared to region II. These arguments allow us to rationalize the 2ph process rates in Fig. 3.5.

Let us discuss the temperature dependence of the 2ph scattering processes, focusing on the ratio $\Gamma^{(2\mathrm{ph})}/\Gamma^{(1\mathrm{ph})}$ of the 2ph scattering rates to the leading-order 1ph rates. We provide a brief analysis here and a more extensive discussion in the Supplementary Materials (see Fig. 3.12). The temperature dependence of the 2ph rates

originates from the intermediate state lifetimes in the denominators of Eq. (3.3) and the thermal factors $A^{(i)}$ in Eq. (3.4). The intermediate state e-ph scattering rate increases with temperature due to an increase in phonon number, so the intermediate state lifetimes become shorter, lowering the 2ph rate $\Gamma^{(2ph)}$ for increasing temperatures. On the contrary, the thermal factors $A^{(i)}$, which contain factors proportional to the phonon number N, increase rapidly with temperature, making $\Gamma^{(2ph)}$ greater at higher temperatures. In the 200–400 K temperature range investigated here, these two effects compensate in GaAs, resulting in nearly temperature independent $\Gamma^{(2ph)}/\Gamma^{(1ph)}$ ratios. We conclude that the 2ph processes are equally as important relative to the leading-order 1ph processes over a wide temperature range near room temperature.

Contribution to the electron mobility

Since the 2ph contributions are significant, one expects that they contribute to charge transport. Figure 3.7 shows the electron mobility in GaAs obtained by solving the BTE, either within the relaxation time approximation (RTA) or with a more accurate

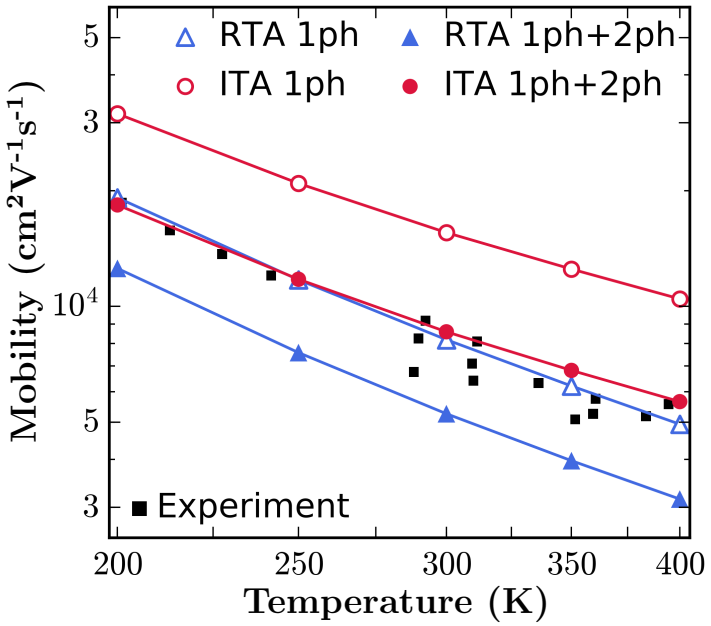

Figure 3.7: **Calculated electron mobility in GaAs.** Electron mobility in GaAs, computed by solving the linearized BTE, either within the RTA or with an iterative approach (ITA). For each solution method, two sets of calculations are shown, one that includes only the 1ph leading-order processes, and one that includes both 1ph and 2ph scattering. Experimental values are taken from Refs. [34–40].

iterative approach (ITA) [6, 9], which we have extended here to include 2ph processes (see Appendix B). Results are given for calculations that either neglect or include the 2ph contributions. The iterative solution with only 1ph scattering overestimates the electron mobility in GaAs by 40−80% at 200−400 K, consistent with results in Ref. [10] (and in Ref. [6], provided the polar correction is not included for the acoustic modes, which artificially increases the acoustic mode contribution to scattering in Ref. [6] and lowers the computed mobility). This result is puzzling, since the BTE can accurately predict the mobility in nonpolar semiconductors; the discrepancy with experiment is too large to be due to small errors in the electron effective mass (in our calculation, the effective mass is $0.055m_0$ versus an experimental value of $0.067m_0$, where m_0 is the electron mass). Redoing the mobility calculation with a band structure with the experimental effective mass of $0.067m_0$ (see Fig. 3.11 in Supplementary Materials) reduces the mobility overestimate to roughly 20% compared to experiment for the iterative BTE solution with 1ph scattering, and including 2ph processes still improves the agreement with the experiment of the mobility and its temperature dependence.

This open problem is solved here by including the 2ph processes in the ITA, which lowers the mobility due to the additional 2ph scattering and gives mobility values in excellent agreement with experiments [34–40]. Both the absolute value of the mobility and its temperature dependence improve when the 2ph processes are included. This result implies that the agreement with the experiment of the RTA with 1ph processes is due to error compensation. We conclude that the 2ph contributions are crucial to improving the computed electron mobility in GaAs.

Since the long-range LO mode coupling is dominant in many polar semiconductors and oxides, we expect the 2ph processes to be important in a wide range of polar materials. We apply our approach to $BaSnO_3$, a weakly polar oxide with dominant LO-mode e-ph interactions and a high room-temperature electron mobility. We compute the 2ph scattering rates and the mobility including 2ph processes in $BaSnO_3$ (see Fig. 3.10 in Supplementary Materials). Similarly to GaAs, the mobility computed with the iterative BTE including only 1ph processes is substantially higher than the experimental value, while adding 2ph scattering significantly improves the agreement with experiment. This result confirms that our approach is broadly applicable to weakly polar semiconductors, in which perturbation theory is valid and the mobility near room temperature is usually limited by scattering with the LO mode.

3.3 Discussion

Our calculations show quantitatively that the 2ph contributions are substantial even in a weakly polar material such as GaAs in which higher-order e-ph interactions and polaron effects are typically neglected. The approach introduced in this work is general, and it is expected to give accurate e-ph scattering rates and carrier mobilities in weakly polar III-V and II-VI semiconductors and in polar oxides with high room-temperature mobility (and thus, weak polaron effects [22]); the perturbative approach is valid in these materials, and the long-range e-ph interactions make next-to-leading order effects substantial.

An open question left out for future work is whether the 2ph processes due to acoustic modes can be important in metals and nonpolar materials. A practical observation is that the mobility computed using only 1ph processes matches the experiment closely in elemental metals [3] and nonpolar semiconductors [10], so 2ph acoustic processes are expected to be negligible, although a rigorous proof (or numerical evidence) of this point is more challenging. As discussed by Kocevar [14], there are two e-ph perturbations contributing to 2ph processes. The one considered in this work is due to the first derivative of the potential with respect to lattice vibrations, taken to second order in perturbation theory, which leads to 2ph scattering consisting of two consecutive 1ph scattering events. The second contribution, which is not included in this work, is due to the second derivatives of the potential with respect to lattice vibrations; it leads to a direct 2ph interaction associated with the so-called Debye-Waller (DW) vertex, which represents an electron interacting simultaneously with two phonons [14]. The DW vertex leads to additional self-energy diagrams and 2ph processes, some of which are illustrated in Fig. 3.8.

Due to translational invariance, for acoustic phonons in the long-wavelength limit, there is a strong cancellation between the scattering processes considered here and those due to the DW interaction [14, 41]. This cancellation has also been hypothesized to be valid for acoustic phonons beyond the long-wavelength limit, although this point has never been proven. This result, together with the numerical evidence that 1ph processes are sufficient to explain the mobility in nonpolar semiconductors and elemental metals, is suggestive of a negligible role of 2ph acoustic processes. Since the DW vertex cannot currently be computed *ab initio* for two general phonon momenta, numerical studies of 2ph processes due to the DW interaction are left out for future work. In the calculations on the two weakly polar materials considered here, GaAs and $BaSnO_3$, the LO mode interaction is dominant, and our results are

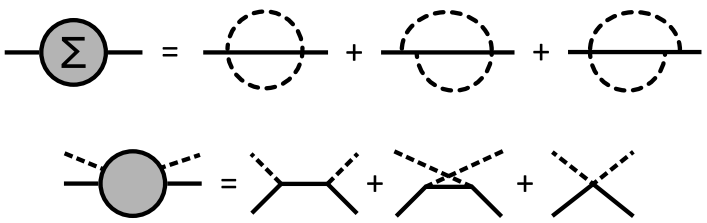

Figure 3.8: **Diagrams beyond this work.** The top panel shows some of the additional self-energy diagrams resulting from the four-point Debye-Waller vertex, which introduces a new 1e1a process interfering with the two considered in this work in the bottom panel.

nearly unchanged if acoustic phonons are included.

In summary, our calculations of the 2ph scattering rates and their contribution to the mobility pave the way to studying higher-order e-ph interactions and charge transport in polar materials from first principles. Together with recently proposed methods to treat charge transport in materials with polarons and stronger e-ph interactions [26], it is clear that *ab initio* calculations are becoming able to investigate e-ph interactions and charge transport in a wide range of polar materials.

3.4 Methods

Numerical calculations

The DFT and lowest-order e-ph calculations in GaAs follow our previous work [4]. Briefly, we carry out DFT calculations in GaAs using the QUANTUM ESPRESSO code [42] with a plane-wave basis set. We employ the local density approximation [43] and norm-conserving pseudopotentials [44]. A relaxed lattice constant of 5.55 Å, a kinetic energy cutoff of 72 Ry, and $8 \times 8 \times 8$ $\mathbf{k}$-point grids are used in all DFT calculations. Phonon dispersions are computed with density functional perturbation theory (DFPT) [45] on an $8 \times 8 \times 8$ $\mathbf{q}$-point grid. The e-ph coupling constants, $g_{nm\nu}(\mathbf{k}, \mathbf{q})$, are computed using these coarse $\mathbf{k}$- and $\mathbf{q}$-point grids [4] using DFPT together with our in-house developed PERTURBO code [33], and interpolated using Wannier functions [46] generated with WANNIER90 [47].

To compute and converge the 2ph scattering rates, we use Monte Carlo integration by sampling up to 3 billion random $(\mathbf{q}, \mathbf{p})$ pairs of Brillouin zone points drawn from a Cauchy distribution [4]. The delta function in Eq. (3.2) is approximated by a Gaussian with a small broadening of 5 meV. Since in GaAs the LO phonon dominates e-ph scattering for electrons within ~100 meV of the conduction band

edge [4], in the 2ph scattering rate calculations we use only the long-range coupling to the LO modes [13, 48, 49], which greatly reduces the 2ph computational cost while giving 2ph scattering rates nearly identical to calculations with all phonon modes included (see Fig. 3.9 in Supplementary Materials). We use a carrier concentration of 10^{16} cm^{-3} in all scattering rate and mobility calculations, and set the chemical potential accordingly at each temperature. The mobility calculations are carried out by integrating over energies of up to 250 meV above the conduction band minimum; we have verified that this energy window is sufficient to converge the mobility.

We highlight that the 2ph scattering rate calculations are *extremely* computationally expensive due to the large number of points sampled in the BZ integral over two phonon momenta. The average cost for computing the 2ph scattering rate in GaAs is ~500 CPU core hours per electronic state for each iteration over the intermediate state lifetime; a typical calculation requires 10 iterations to converge, for a total cost of 5,000 CPU core hours per electronic state. By contrast, it takes only 0.08 CPU core hours (5 minutes on a single CPU core) per electronic state to converge the 1ph scattering rate using our code. The computational cost of the 2ph scattering rates is thus approximately $10^4 - 10^5$ higher than the 1ph scattering rates.

3.5 Supplementary Materials

Two-phonon scattering rates with all phonon modes included

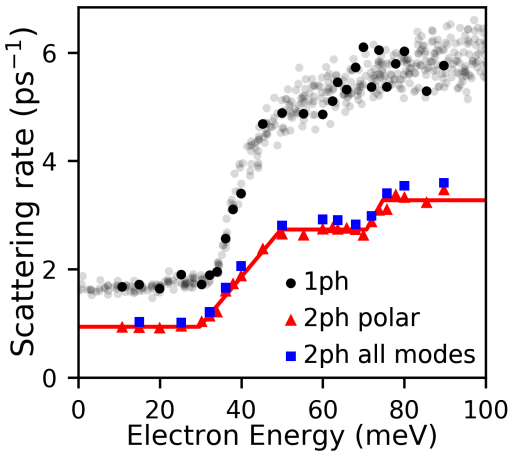

Figure 3.9: **Two-phonon scattering rates with all phonon modes included.** The 2ph scattering rates $\Gamma^{(2ph)}_{n\mathbf{k}}$ in GaAs at 300 K, computed using only the LO mode (curve labelled "2ph polar") and with all phonon modes included (curve labelled "2ph all modes").

Mobility calculation in barium stannate

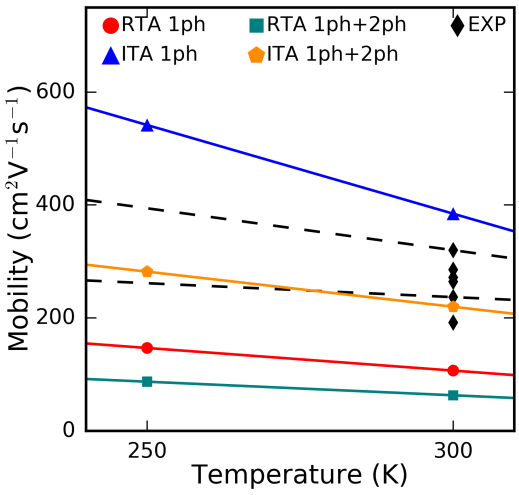

Figure 3.10: **Mobility calculation in $BaSnO_3$.** Electron mobility in $BaSnO_3$ computed using the same methods as in Fig. 3.7. It is seen that the iterative BTE with only 1ph scattering overestimates the mobility, while including 2ph scattering improves the agreement with the experiment, similarly to GaAs. Experimental data are shown with markers at room temperature and dashed lines at lower temperatures. The experimental data are from Figs. 4 and 5 in Ref. [50]. We used the single crystal mobility data for a $0.5 - 1.5 \times 10^{20}$ cm^{-3} carrier concentration range. Our calculation used a 0.8×10^{20} cm^{-3} carrier concentration.

Mobility results with experimental effective mass

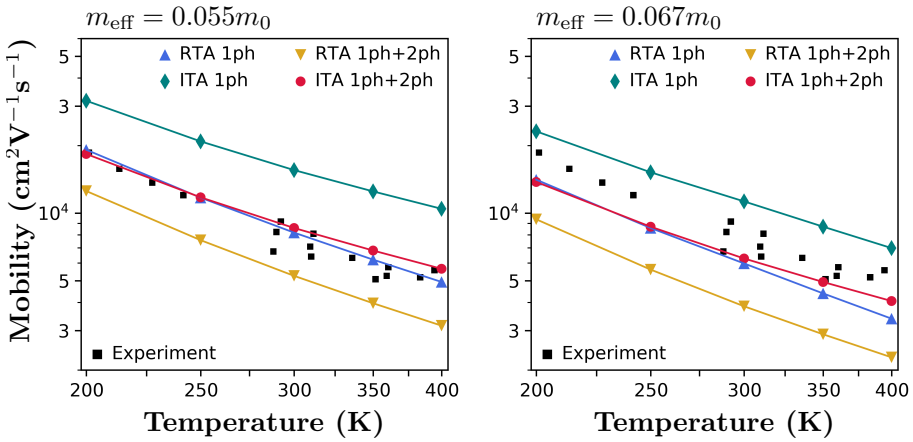

Figure 3.11: **Mobility results with experimental effective mass.** Comparison of mobility results calculated from our DFT band structure with an effective mass of $0.055m_0$ (left panel) and a band structure with the experimental effective mass of $0.067m_0$ (right panel) obtained by manually rescaling the DFT eigenvalues by a factor of $0.067/0.055$. Here, m_0 is the bare electron mass.

Temperature dependence of the two-phonon scattering rates

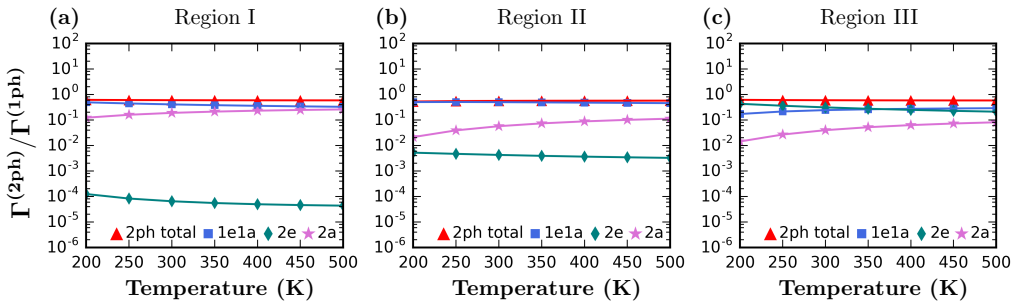

Figure 3.12: **Temperature dependence of the 2ph scattering rates.** Temperature dependence of the ratios of the 2ph scattering processes to the leading order e-ph scattering rate. From left to right, the panels are for electronic states with energies of 20, 45, and 90 meV above the conduction band minimum, and thus, respectively, in region I, II, and III defined in Section 3.2.

Figure 3.12 above shows the temperature dependence of the ratios of the 2ph scattering rate and the leading order scattering rate, $\Gamma^{(2ph)}/\Gamma^{(1ph)}$. Results are given for three electronic states, one in each of the regions I, II, and III defined in Section 3.2. The ratios are given for both the total 2ph scattering rate and (for completeness) for the individual 2ph processes, 1e1a, 2e, and 2a. In the 200−500 K temperature range considered in this work, the ratio of the total 2ph scattering rate to the 1ph scattering rate is nearly temperature independent in all three energy regions.

References

[1] M. Bernardi, Eur. Phys. J. B **89**, 239 (2016).

[2] M. Bernardi, D. Vigil-Fowler, J. Lischner, J. B. Neaton, and S. G. Louie, Phys. Rev. Lett. **112**, 257402 (2014).

[3] J. I. Mustafa, M. Bernardi, J. B. Neaton, and S. G. Louie, Phys. Rev. B **94**, 155105 (2016).

[4] J.-J. Zhou and M. Bernardi, Phys. Rev. B **94**, 201201 (2016).

[5] G. Brunin, H. P. C. Miranda, M. Giantomassi, M. Royo, M. Stengel, M. J. Verstraete, X. Gonze, G.-M. Rignanese, and G. Hautier, Phys. Rev. B **102**, 094308 (2020).

[6] T.-H. Liu, J. Zhou, B. Liao, D. J. Singh, and G. Chen, Phys. Rev. B **95**, 075206 (2017).

[7] J.-J. Zhou, O. Hellman, and M. Bernardi, Phys. Rev. Lett. **121**, 226603 (2018).

[8] N.-E. Lee, J.-J. Zhou, L. A. Agapito, and M. Bernardi, Phys. Rev. B **97**, 115203 (2018).

[9] W. Li, Phys. Rev. B **92**, 075405 (2015).

[10] J. Ma, A. S. Nissimagoudar, and W. Li, Phys. Rev. B **97**, 045201 (2018).

[11] T. Sohier, D. Campi, N. Marzari, and M. Gibertini, Phys. Rev. Mater. **2**, 114010 (2018).

[12] H. Fröhlich, Adv. Phys. **3**, 325–361 (1954).

[13] P. Vogl, Phys. Rev. B **13**, 694–704 (1976).

[14] P. Kocevar, *"Physics of Nonlinear Transport in Semiconductors"* (Springer US, 1980), pp. 167–174.

[15] G. P. Alldredge and F. J. Blatt, Ann. Phys. **45**, 191–231 (1967).

[16] A. Sher and K. K. Thornber, Appl. Phys. Lett. **11**, 3–5 (1967).

[17] G. I. Thorbergsson and J. Sak, Phys. Lett. A **116**, 325–328 (1986).

[18] M. E. Mora-Ramos, F. J. Rodríguez, and L. Quiroga, J. Phys. Condens. Matter **11**, 8223–8238 (1999).

[19] M. A. Smondyrev, Theor. Math. Phys. **68**, 653–664 (1986).

[20] Z. Wang and G. D. Mahan, Phys. Rev. B **39**, 10753–10760 (1989).

[21] L. M. Woods and G. D. Mahan, Phys. Rev. B **57**, 7679–7685 (1998).

[22] D. Emin, *"Polarons"*, 1st ed. (Cambridge University Press, 2012).

[23] O. Gunnarsson, V. Meden, and K. Schönhammer, Phys. Rev. B **50**, 10462–10473 (1994).

[24] S. M. Story, J. J. Kas, F. D. Vila, M. J. Verstraete, and J. J. Rehr, Phys. Rev. B **90**, 195135 (2014).

[25] J. P. Nery, P. B. Allen, G. Antonius, L. Reining, A. Miglio, and X. Gonze, Phys. Rev. B **97**, 115145 (2018).

[26] J.-J. Zhou and M. Bernardi, Phys. Rev. Research **1**, 033138 (2019).

[27] J. Noffsinger, E. Kioupakis, C. G. Van de Walle, S. G. Louie, and M. L. Cohen, Phys. Rev. Lett. **108**, 167402 (2012).

[28] M. Murayama and T. Nakayama, Phys. Rev. B **52**, 4986–4997 (1995).

[29] A. Hayat, P. Ginzburg, and M. Orenstein, Nat. Photonics **2**, 238 (2008).

[30] Z. Bern, L. Dixon, and A. Ghinculov, Phys. Rev. D **63**, 053007 (2001).

[31] T. Aoyama, T. Kinoshita, and M. Nio, Phys. Rev. D **97**, 036001 (2018).

[32] G. D. Mahan, *"Many-Particle Physics"*, 3rd ed. (Springer, 2000).

[33] J.-J. Zhou, J. Park, I.-T. Lu, I. Maliyov, X. Tong, and M. Bernardi, Preprint at arXiv:2002.02045 (2020).

[34] D. L. Rode, Phys. Rev. B **2**, 1012–1024 (1970).

[35] D. L. Rode and S. Knight, Phys. Rev. B **3**, 2534–2541 (1971).

[36] J. S. Blakemore, J. Appl. Phys. **53**, R123–R181 (1982).

[37] H. G. B. Hicks and D. F. Manley, Solid State Commun. **7**, 1463–1465 (1969).

[38] C. M. Wolfe, G. E. Stillman, and W. T. Lindley, J. Appl. Phys. **41**, 3088–3091 (1970).

[39] P. Blood, Phys. Rev. B **6**, 2257–2261 (1972).

[40] K. H. Nichols, C. M. L. Yee, and C. M. Wolfe, Solid-State Electronics **23**, 109–116 (1980).

[41] T. Holstein, Phys. Rev. **113**, 479–496 (1959).

[42] P. Giannozzi et al., J. Phys. Condens. Matter **21**, 395502 (2009).

[43] J. P. Perdew and A. Zunger, Phys. Rev. B **23**, 5048–5079 (1981).

[44] N. Troullier and J. L. Martins, Phys. Rev. B **43**, 1993–2006 (1991).

[45] S. Baroni, S. de Gironcoli, A. Dal Corso, and P. Giannozzi, Rev. Mod. Phys. **73**, 515–562 (2001).

[46] F. Giustino, M. L. Cohen, and S. G. Louie, Phys. Rev. B **76**, 165108 (2007).

[47] A. A. Mostofi, J. R. Yates, G. Pizzi, Y.-S. Lee, I. Souza, D. Vanderbilt, and N. Marzari, Comput. Phys. Commun. **185**, 2309–2310 (2014).

[48] J. Sjakste, N. Vast, M. Calandra, and F. Mauri, Phys. Rev. B **92**, 054307 (2015).

[49] C. Verdi and F. Giustino, Phys. Rev. Lett. **115**, 176401 (2015).

[50] H. J. Kim, U. Kim, T. H. Kim, J. Kim, H. M. Kim, B.-G. Jeon, W.-J. Lee, H. S. Mun, K. T. Hong, J. Yu, K. Char, and K. H. Kim, Phys. Rev. B **86**, 165205 (2012).

Chapter 4

FACILE AB INITIO APPROACH FOR SELF-LOCALIZED POLARONS FROM A CANONICAL TRANSFORMATION

4.1 Introduction

Self-localized (small) polarons are charge carriers that interact strongly with the lattice vibrations, becoming trapped as a result of the local lattice distortion [1]. Small polarons are essential to understanding electrical transport and optical properties in a wide range of materials, including transition metal oxides, alkali halides, and organic molecular crystals [2–4]. The presence of small polarons in these materials is typically associated with a diffusive, thermally activated charge transport regime characterized by low mobility values, typically less than 1 $\mathrm{cm}^2/\mathrm{V\,s}$ [5]. Recent progress has enabled direct observation of small polaron states [6, 7] and clarified their important role in various technologies [8–12].

The theoretical treatment of small polarons was pioneered by Holstein [13] based on ideas from Landau and Pekar [14]. It was later extended by Lang and Firsov [15], and generalized by Munn and Silbey [16, 17] and Hannewald et al. [18] to improve the treatment of electron-phonon (e-ph) interactions. The resulting small polaron theory can qualitatively demonstrate the transition from bandlike to hopping transport observed in experiments [4, 19, 20], but the presence of a self-localized polaron state is typically assumed in these theories rather than directly predicted. These approaches are not geared toward quantitative predictions on real materials as they rely on empirical parameters and take into account only one (or a few) vibrational modes.

Early work formulated the problem of polaron formation as a competition of energies for localizing an electronic state, which relaxes the lattice while increases the electron kinetic energy [21]. Yet, whether charge carriers form small polarons or not remains controversial in many materials. For example, angle-resolved photoemission experiments found no evidence of small polarons in $SrTiO_3$ [22] although mobility and optical measurements suggest their presence [23, 24].

First-principles calculations can accurately compute the electronic structure, lattice dynamics, and e-ph coupling [25], and are ideally suited to provide quantitative approaches for treating both large and small polarons. However, existing studies

have focused on semiconductors and insulators without small polaron effects [26–32]. First-principles calculations of small polarons involve supercells with excess charge or defects explicitly added [33–36]. While useful, these approaches require computationally costly calculations with many atoms, and their reliability is limited by the accuracy of density functional theory (DFT) exchange-correlation functionals and the treatment of charged systems in DFT. A rigorous first-principle approach connecting standard small polaron theory [37] and modern *ab initio* e-ph calculations is still missing.

Here we show an efficient real-space approach to compute the small polaron energy starting from a trial polaron wavefunction. Employing a canonical transformation formalism [13], we construct a self-localized polaron state that is free from hopping and decoupled from all vibrational modes[1]. We establish whether an electron or hole charge carrier favors a delocalized state or tends to self-trap by comparing the energy of the polaron state with the conduction or valence band edge, at once predicting whether a small polaron forms and determining its formation energy. The computational cost of this scheme is equivalent to a DFT calculation on a unit cell plus an inexpensive e-ph computational step. Its efficiency allows us to investigate small polarons in various alkali halides, oxides, and perovskites. Our work bridges the gap between small polaron theory and *ab initio* e-ph calculations, formulating an efficient computational approach to treat small polarons from first principles.

4.2 Small Polaron Hamiltonian

Analogy to the charged harmonic oscillator

We derive the effective small polaron Hamiltonian in a distorted lattice through a canonical transformation [13] inspired by the treatment of the charged harmonic oscillator (CHO) in an external electric field E [38]. The Hamiltonian of a one-dimensional CHO is

$$H^{(\mathrm{CHO})} = \omega(b^\dagger b + \frac{1}{2}) - \omega g(b + b^\dagger), \tag{4.1}$$

where $b^\dagger$ and b are creation and annihilation operators for the oscillator quanta and the coupling parameter is $g = eE/\sqrt{2m\omega^3}$, with e, m, ω the charge, mass, and frequency of the oscillator, respectively. Here and below, we set $\hbar = 1$. To solve the CHO Hamiltonian, the common approach is to stretch the oscillator spring to its new equilibrium position using the canonical transformation of operators,

[1] Note that here we define a small polaron as a self-trapped electronic state, regardless of its spatial extent.

$O \to \widetilde{O} = e^S O e^{-S}$. Defining the CHO generator as $S^{(\mathrm{CHO})} = -g(b^\dagger - b)$, this transformation gives

$$\widetilde{b} = b + g, \tag{4.2}$$

$$\widetilde{H}^{(\mathrm{CHO})} = \omega(b^\dagger b + \frac{1}{2}) - \omega g^2. \tag{4.3}$$

The shift of the operator b in Eq. (4.2) amounts to shifting the coordinate system:

$$\widetilde{x} = \frac{1}{\sqrt{2m\omega}}(\widetilde{b}^\dagger + \widetilde{b}) = \frac{1}{\sqrt{2m\omega}}(b^\dagger + b) + x_0, \tag{4.4}$$

where x is the position operator and $x_0 = 2g/\sqrt{2m\omega}$ is the new equilibrium position. The second term in Eq. (4.3) is always negative and can be interpreted as the energy decrease resulting from relaxing the system to a new equilibrium position due to the electrical force, because $-\omega g^2 = \frac{1}{2}m\omega^2 {x_0}^2 - eEx_0$.

Canonical transformation

We follow Holstein's treatment [13] and perform an analogous transformation on the e-ph Hamiltonian in the electronic Wannier [39] and phonon momentum basis,

$$\begin{aligned} H = &\sum_{mn} \varepsilon_{mn} a_m^\dagger a_n + \sum_{\mathbf{Q}} \omega_{\mathbf{Q}} \left(b_{\mathbf{Q}}^\dagger b_{\mathbf{Q}} + \frac{1}{2} \right) \\ &+ \frac{1}{\sqrt{N_\Omega}} \sum_{mn} \sum_{\mathbf{Q}} \omega_{\mathbf{Q}} g_{\mathbf{Q}mn} \left(b_{\mathbf{Q}}^\dagger + b_{-\mathbf{Q}} \right) a_m^\dagger a_n. \end{aligned} \tag{4.5}$$

Here, $n = j_n \mathbf{R}_n$ is a collective index labelling the j_n-th Wannier function (WF) in the unit cell with origin at the Bravais lattice vector $\mathbf{R}_n$, while $a_n = a_{j_n \mathbf{R}_n}$ is the corresponding electron annihilation operator and $b_{\mathbf{Q}} = b_{\nu\mathbf{q}}$ is the annihilation operator for the phonon with mode index ν and momentum $\mathbf{q}$. The hopping strength and phonon energy are denoted as ε_{mn} and $\omega_{\mathbf{Q}}$, respectively, and N_Ω is the number of unit cells in the crystal. Here the e-ph coupling matrix element in the Wannier basis, denoted as $g_{\mathbf{Q}mn}$, does not include the phonon frequency factor, different from the standard convention [40]. Also recall that the e-ph coupling needs to satisfy the relation $g^*_{\mathbf{Q}mn} = g_{-\mathbf{Q}nm}$ for the Hamiltonian to be Hermitian.

We define the generator S as

$$S = \sum_{mn} C_{mn} a_m^\dagger a_n, \tag{4.6}$$

$$C_{mn} = \frac{1}{\sqrt{N_\Omega}} \sum_{\mathbf{Q}} B_{\mathbf{Q}mn} (b_{\mathbf{Q}}^\dagger - b_{-\mathbf{Q}}), \tag{4.7}$$

and using the transformation $O \to \widetilde{O} = e^{S} O e^{-S}$, we obtain the transformed electron and phonon annihilation operators, respectively, as

$$\widetilde{a}_m = \sum_n e^{-C}_{mn} a_n, \tag{4.8}$$

$$\widetilde{b}_{\mathbf{Q}} = b_{\mathbf{Q}} - \frac{1}{\sqrt{N_\Omega}} \sum_{mn} B_{\mathbf{Q}mn} a^\dagger_m a_n, \tag{4.9}$$

where e^{-C}_{mn} is the shorthand notation for the phonon operator

$$e^{-C}_{mn} = \delta_{mn} - C_{mn} + \frac{1}{2!} \sum_i C_{mi} C_{in} - \cdots, \tag{4.10}$$

where C_{mn} is defined in Eq. (4.7). Above, we introduced the undetermined distortion coefficients $B_{\mathbf{Q}mn}$ which, analogous to the coupling g in the CHO example, quantify how the transformation stretches the spring of each phonon mode to a new equilibrium position due to the electrical forces applied on the lattice by the charge carrier. This physical interpretation is consistent with Eq. (4.9), where one changes the basis to a distorted lattice configuration, in analogy with Eq. (4.2); the operators $a^\dagger_n$ and $b^\dagger_{\mathbf{Q}}$ now create polaron and phonon in this distorted lattice, respectively. To make the transformation unitary, the same conjugate relations used for $g_{\mathbf{Q}mn}$ are imposed on the distortion coefficient, $B^*_{\mathbf{Q}mn} = B_{-\mathbf{Q}nm}$, so that the operators C_{mn} and S are both anti-Hermitian.

Effective polaron Hamiltonian

The transformed Hamiltonian is obtained by substituting the transformed electron and phonon operators:

$$\begin{aligned} \widetilde{H} = &\sum_{mn} E_{mn} a^\dagger_m a_n + \sum_{\mathbf{Q}} \omega_{\mathbf{Q}} (b^\dagger_{\mathbf{Q}} b_{\mathbf{Q}} + \frac{1}{2}) \\ &+ \frac{1}{\sqrt{N_\Omega}} \sum_{mn\mathbf{Q}} \omega_{\mathbf{Q}} G_{\mathbf{Q}mn} (b^\dagger_{\mathbf{Q}} + b_{-\mathbf{Q}}) a^\dagger_m a_n, \end{aligned} \tag{4.11}$$

where the polaron hopping strength E_{mn} and the residual polaron-phonon (pl-ph) coupling constant $G_{\mathbf{Q}mn}$ are defined, respectively, as

$$\begin{aligned} E_{mn} &= \langle \widetilde{\varepsilon} \rangle_{mn} + \frac{1}{N_\Omega} \sum_{i\mathbf{Q}} \omega_{\mathbf{Q}} B_{-\mathbf{Q}mi} \left(B_{\mathbf{Q}in} - 2 \langle \widetilde{g}_{\mathbf{Q}} \rangle_{in} \right), \\ G_{\mathbf{Q}mn} &= \langle \widetilde{g}_{\mathbf{Q}} \rangle_{mn} - B_{\mathbf{Q}mn}, \end{aligned} \tag{4.12}$$

where the angle brackets $\langle \cdots \rangle$ indicate a thermal average over phonon states. In this effective polaron Hamiltonian, the transformed hopping and e-ph coupling matrices

$\widetilde{\varepsilon}_{mn}$ and $\widetilde{g}_{\mathbf{Q}mn}$, denoted here $\widetilde{M}_{mn}$, are defined as

$$\widetilde{M}_{mn} = \sum_{ij} e^{C}_{mi} M_{ij} e^{-C}_{jn}. \tag{4.13}$$

These transformed matrices still contain phonon operators (through the operator C_{mn}). Following Holstein [13], we take their thermal average in Eq. (4.12) to obtain the effective polaron Hamiltonian in Eq. (4.11).

Self-localized small polaron states

We then set the distortion coefficients to

$$B_{\mathbf{Q}mn} = g_{\mathbf{Q}mn}\delta_{mn}, \tag{4.14}$$

and show that this choice leads to a self-localized polaron state. Using this ansatz, the thermal average of the transformed matrix can be written as $\langle\widetilde{M}\rangle_{mn} = \exp\left[-\lambda_{mn}\right] M_{mn}$ [38], where the exponent λ_{mn} depends on the difference between the local e-ph coupling at the m and n WF sites,

$$\lambda_{mn} = \frac{1}{N_\Omega}\sum_{\mathbf{Q}}\left(N_{\mathbf{Q}} + \frac{1}{2}\right)\left|g_{\mathbf{Q}mm} - g_{\mathbf{Q}nn}\right|^2, \tag{4.15}$$

and on the phonon occupation factor $N_{\mathbf{Q}}$. In this work, the quantity λ_{mn} is computed using *ab initio* e-ph coupling constants $g_{\mathbf{Q}mm}$, paying attention to converge the Brillouin zone integral in Eq. (4.15). The diagonal part of λ_{mn} is identically zero, which makes $\exp[-\lambda_{mm}] = 1$ for all sites m. The off-diagonal part of $\exp[-\lambda_{mn}]$ is orders of magnitude smaller than unity (typically of order 10^{-2} to 10^{-10} at 300 K), as we verify explicitly in our numerical calculations, and thus we approximately have

$$\exp[-\lambda_{mn}] \approx \delta_{mn}. \tag{4.16}$$

Substituting Eqs. (4.14) to (4.16) into Eq. (4.12), we derive the central equations in this work,

$$E_{mn} = \left(\varepsilon_{mm} - \frac{1}{N_\Omega}\sum_{\mathbf{Q}}\omega_{\mathbf{Q}}\left|g_{\mathbf{Q}mm}\right|^2\right)\delta_{mn}, \tag{4.17}$$

$$G_{\mathbf{Q}mn} = 0.$$

The first equation implies that the operator $a^\dagger_m$ in Eq. (4.11) creates a self-localized polaron state, because hopping to nearby states is negligible due to the vanishing

off-diagonal E_{mn} elements. The second line implies that this small polaron state is also decoupled from all phonon modes as $G_{\mathbf{Q}mn} = 0$. The on-site polaron energy E_{mm} is the sum of the electronic energy ε_{mm} of the corresponding WF and the potential energy decrease due to the lattice distortion, analogous to the CHO case [compare the second terms in Eqs. (4.3) and (4.17)].

Whether or not a small polaron forms depends on the competition of two terms, the potential energy decrease due to the lattice distortion and the kinetic energy increase resulting from localizing a Bloch electronic state. If the on-site polaron energy E_{mm} is lower than the energy of the conduction band minimum (CBM) for an electron carrier, or higher than the valence band maximum (VBM) for a hole carrier, then the self-localized polaron is energetically more favorable than a delocalized Bloch wavefunction. In this scenario, the electron or hole quasiparticle forms a small polaron and becomes self-trapped by the lattice distortion; the polaron formation energy is thus the difference between the polaron energy E_{mm} and the respective band edge. An additional insight provided by Eq. (4.17) is that a material with less dispersive electronic bands and stronger on-site e-ph coupling is more likely to host a small polaron.

While Eq. (4.17) gives the polaron energy for an electron with wavefunction equal to a given WF, the choice of a WF created by the operator $a_m^\dagger$ is not unique. In fact, the small polaron wavefunction has rarely been discussed in the canonical transformation treatment. We point out that different WFs will induce different lattice distortions, resulting in different polaron energies; the most stable polaron state corresponds to the WF minimizing the polaron energy (see Section 4.6 for additional discussion). In the following, we take a maximally localized WFs as a trial wavefunction and compute its polaron energy. If the resulting small polaron is stable, as determined by comparing the electron or hole polaron energy with the respective band edge, then our approach provides a sufficient condition for concluding that a small polaron forms in a given material, as well as an approximate polaron wavefunction. Systematic minimization of the polaron energy, which is left out for future work, would more accurately determine the polaron wavefunction, refining the WF guess.

4.3 Methods

We carry out DFT calculations using the Quantum ESPRESSO code [41] with a plane-wave basis set, employing norm-conserving pseudopotentials [42] from

Pseudo Dojo [43] and the Perdew-Burke-Ernzerhof generalized gradient approximation [44]. A kinetic energy cutoff of 100 Ry, an $8\times8\times8$ **k**-point grid, and relaxed lattice parameters are used in all DFT calculations. We use density functional perturbation theory [45] to compute phonon frequencies and eigenvectors on a coarse $8\times8\times8$ **q**-point grid for all materials except Na_2O_2, for which we use a $4\times4\times4$ **q**-point grid. The e-ph coupling constants $g_{mn\nu}(\mathbf{k},\mathbf{q})$ are obtained on coarse grids and transformed to Wannier basis $g_{\mathbf{Q}mn}$ using the PERTURBO code [40], with WFs generated from WANNIER90 [46].

Before computing the polaron energy, we first numerically verify that the identity of Eq. (4.16) is satisfied by carrying out the integration in Eq. (4.15) in all cases. We then compute the on-site polaron energy, E_{mm} in Eq. (4.17), computing the Brillouin zone integral via Monte Carlo integration with 1 million random **q** points drawn from a Cauchy distribution. All materials investigated in this work have strong polar bonds and dominant contributions to e-ph coupling from the longitudinal optical modes through the Fröhlich interaction [27, 47]. The temperature is set to 300 K in

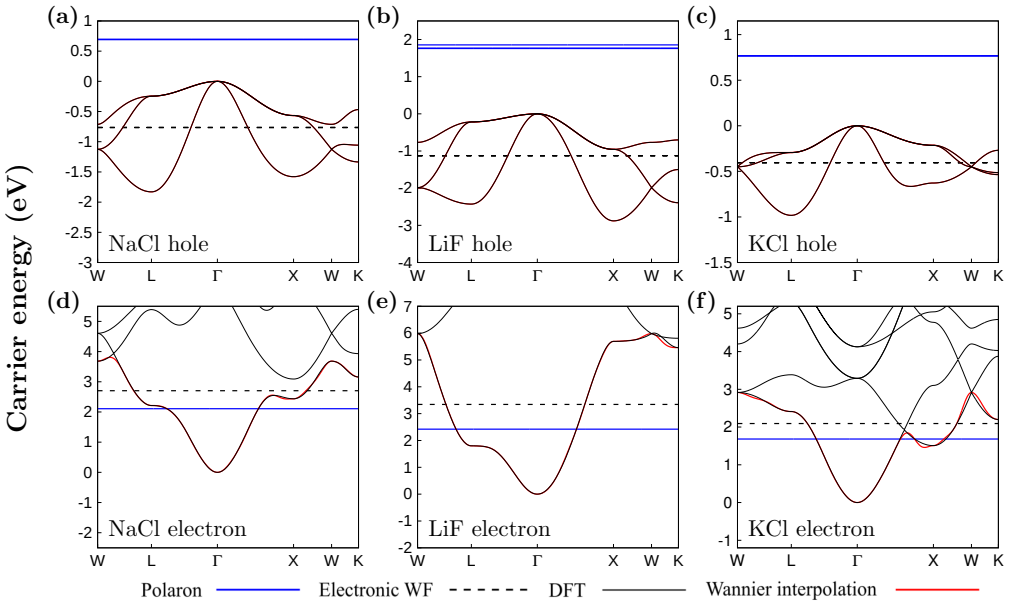

Figure 4.1: **Calculated polaron energy I.** Calculated polaron energy for holes in (a) NaCl, (b) LiF, and (c) KCl, and electrons in (d) NaCl, (e) LiF, and (f) KCl. Blue lines are the polaron on-site energies E_{mm}, and dashed black lines are electronic WF energies ε_{mm}, in Eq. (4.17). The solid black curves are the DFT band structure and the red curves are the Wannier interpolated bands, whose number equals the number of WFs employed in the calculation. The energy zero is set to be either at CBM or VBM, respectively, when electron or hole carriers are considered.

all calculations.

4.4 Results

Figure 4.1 shows the computed polaron energy in three alkali halides, NaCl, LiF, and KCl, for both electron and hole polaron states. Our formalism predicts that holes in these three materials form a self-localized small polaron, in agreement with the experiments [3], because the computed polaron energies E_{mm} are above the VBM, as shown in Fig. 4.1(a)−(c). Electrons in these materials, on the other hand, are not expected to self-trap – as the conduction band in alkali halides is *s*-like and therefore more dispersive than the *p*-like valence band, the potential energy decrease due to the lattice distortion cannot outweigh the increase in kinetic energy for localizing the electronic state. Consistent with this intuition, our results for electrons in NaCl, LiF, and KCl, shown in Fig. 4.1(d)−(f), conclude that electrons in these materials do not form a self-trapped polaron, as is seen by the fact that the polaron energy is above the CBM. Experiments in alkali halides similarly found no evidence of electron polarons down to 5 K temperature [48].

Figure 4.2 shows the calculated electron and hole polaron energies in three alkali metal oxides and peroxides, Na_2O_2, Li_2O_2, and Na_2O. The nature of the charge

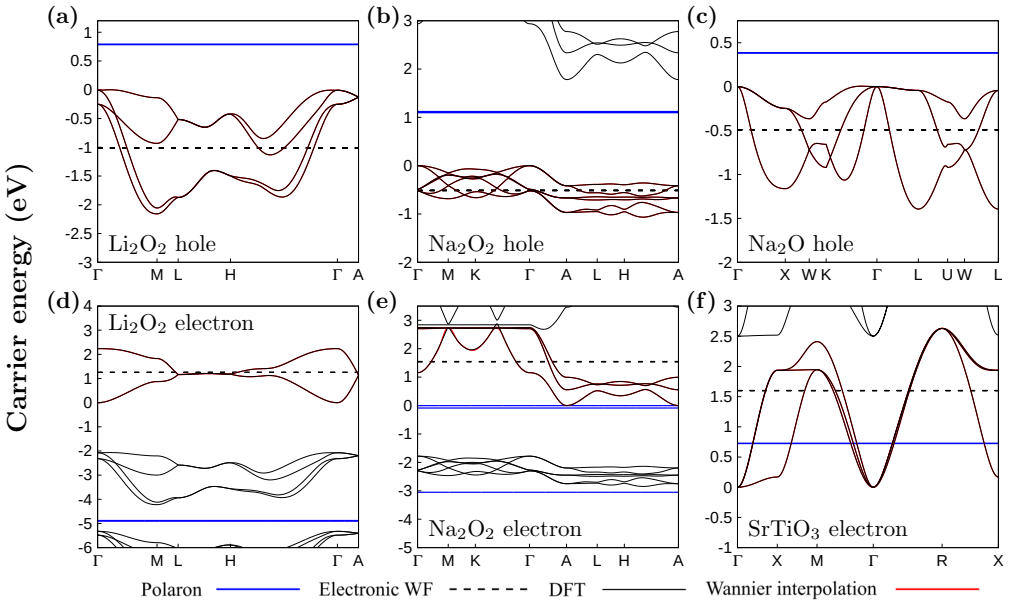

Figure 4.2: **Calculated polaron energy II.** Calculated polaron energy for holes in (a) Li_2O_2, (b) Na_2O_2, and (c) Na_2O, and electrons in (d) Li_2O_2, (e) Na_2O_2, and (f) $SrTiO_3$. The lines and their color code have the same meaning as in Fig. 4.1.

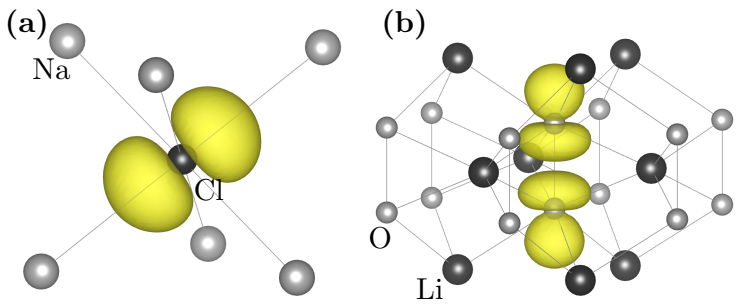

Figure 4.3: **Visualization of polaron wavefunctions.** The square of the trial polaron wavefunction for the (a) hole polaron in NaCl and (b) electron polaron in Li_2O_2.

carriers in these materials is important for application to novel battery technologies, where the low electrical conductivity is a barrier to improved performance and is commonly attributed to the presence of small polarons [8]. Our results in Fig. 4.2 unambiguously demonstrate that both electrons and holes in these materials form a self-localized small polaron, warranting further investigation on their electrical transport properties. The hole polaron wavefunction in NaCl and the electron polaron wavefunction in Li_2O_2 are shown in Fig. 4.3(a) and (b), respectively, highlighting their localized nature.

The last case study we examine is cubic $SrTiO_3$ perovskite, whose electron mobility near room temperature exhibits a power law that can be attributed to a transport regime governed by large (non-self localized) polarons, as we have recently shown [30]. We investigate small polaron formations in cubic $SrTiO_3$, using accurate electronic bandstructure, phonon dispersions, and e-ph interactions from our previous work [29, 30] as a starting point for the polaron calculation. As shown in Fig. 4.2(f), we find a polaron energy significantly higher than the CBM, clearly showing that for electrons in $SrTiO_3$ it is energetically unfavorable to self-localize and form a small polaron state. Note that this finding does not conflict with the existence of localized electronic states due to oxygen vacancies [24, 33], as our formalism treats self-localized electronic states in the pristine crystal.

4.5 Discussion

The formalism presented in this work leaves room for various extensions. One is the possibility of minimizing the polaron energy over the space of possible trial wavefunctions (here, in the form of maximally localized WFs), leading to a more precise computation of the polaron formation energy. In addition, treating e-ph interactions in materials with localized d or f orbitals, for example using the DFT+U

approach, is an important future extension for studies of correlated materials with small polaron effects [49, 50]. Finally, this work paves the way for small polaron transport calculations, for example through the Kubo formula [15, 16], to describe transport in the polaron hopping regime and compute the transition temperature between the bandlike and polaron hopping transport regimes [4, 19, 20]. Both topics are pristine territory for first-principles calculations.

In summary, we developed a facile scheme to predict the formation of self-localized small polarons. Our formalism combines *ab initio* e-ph interactions with an extension of small polaron theory. Its computational cost is a minimal overhead to a DFT calculation on a unit cell, allowing us to rapidly scan several materials. Besides providing a convenient atomistic approach for small polaron studies, our method is a starting point for developing transport calculations in the small polaron hopping regime.

4.6 Supplementary Materials

Polaron wavefunction

The way to determine the polaron wavefunction is less transparent in this formalism. Equation (4.17) gives the polaron energy for the WF created by the operator $a_m^\dagger$. Yet, this WF is not unique. Different WFs have different electronic energies ε_{mm}, and they also induce different lattice distortions because they have different on-site e-ph coupling constants $g_{\mathbf{Q}mm}$ [see Eq. (4.14)], resulting in different polaron energy drops in Eq. (4.17). We illustrate the fact that different trial wavefunctions lead to different polaron energies for NaCl by generating WFs for three bands [Fig. 4.4(a)] or only one band [Fig. 4.4(b)]. We can see that in Fig. 4.4(b), the polaron energy does not exceed the valence band edge, and thus if the electron is initially in this state, it will evolve into states with lower energy, like one of the states in Fig. 4.4(a). These differences can be understood by comparing their on-site e-ph coupling $g_{\mathbf{Q}mm}$. In the case of Fig. 4.4(a), the three WFs, one of which is shown in Fig. 4.3(a), resemble the p orbitals of Cl, and are more spatially localized than the wavefunction in Fig. 4.4(b). Therefore the more localized wavefunction obtained by wannierizing three bands will possess a larger overlap with the phonon perturbation, resulting in a stronger on-site coupling and larger energy decrease [see the second term in Eq. (4.17)].

The true polaron wavefunction of the system is considered to be the most stable polaron wavefunction, which is the WF with the lowest polaron energy. Yet, Eq. (4.17) only gives the polaron energy of a given localized state, while no information

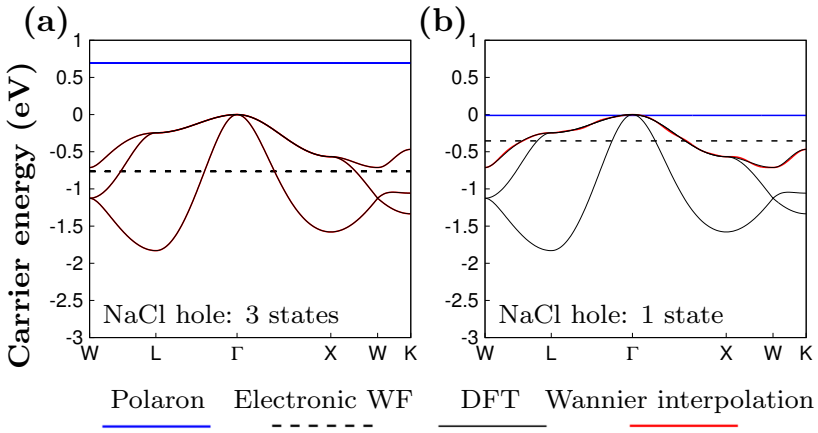

Figure 4.4: **Polaron energies with different trial wavefunctions.** Calculated polaron energy for holes in NaCl using wavefunction obtained by Wannierizing (a) three states and (b) one state. The lines and their color code have the same meaning as in Fig. 4.1 and 4.2.

on which state gives the lowest energy is provided. In Section 4.4, we use the maximally localized WF as a trial wavefunction and compute its polaron energy as a quick test to the polaron formation in materials. If it is the accurate polaron formation energy and polaron wavefunction that are of interests, a variation on all the candidate polaron wavefunctions need to be performed. There are two constraints for a candidate polaron wavefunction created by the operator $a_m^\dagger$. First, when the polaron wavefunction serves as the basis of a tight-binding model, it generates the *ab initio* electronic band structure. Second, since we assume the valence bands are totally filled, it should be orthogonal to all the valence Bloch states (or conduction Bloch states, if the charge carrier of interest is hole). Therefore, all the WFs generated using only the Bloch states in conduction band satisfy both conditions, and comprises the space of candidate polaron wavefunctions.

One strategy to enumerate the candidate polaron wavefunctions and perform the variation is by unitary transformations on existing WFs

$$a'_m = \sum_n U_{mn} a_n. \tag{4.18}$$

Yet, performing a thorough variation on the polaron wavefunction is beyond the scope of this work, and will be left as future direction. In the following, we illustrate how this variation can be performed on a toy model and how it affects the polaron on-site energy. The treatment does not aim to be thorough; instead, it outlines the way to generalize the framework to search for the accurate polaron formation energy

and polaron wavefunction. Since the effect of mixing between states is easier to imagine [for example, see Figs. 4.4(a) and (b)], here, we focus on a toy model with one state per site, and investigate the effect of mixing wavefunctions on different sites.

Toy model: variation of polaron wavefunction

Consider a one-dimensional tight-binding (TB) model with one state per site that couples to one dispersionless phonon with a constant frequency ω_0. The Hamiltonian is given by

$$H^{(\mathrm{TB})} = \sum_{mn} \varepsilon_{mn} a_m^\dagger a_n + \sum_q \omega_0 \left(b_q^\dagger b_q + \frac{1}{2} \right) + \frac{1}{\sqrt{N_\Omega}} \sum_{mn} \sum_q \omega_0 g_{mn}^q \left(b_q^\dagger + b_{-q} \right) a_m^\dagger a_n.$$

Here the indices m and n simply run over all the lattice sites. We only consider the hopping between nearest neighbor sites and set the hopping strength to be $\varepsilon_{mn} = -t\, \delta_{m,n\pm1}$.

The e-ph coupling constant is set to be of the form of

$$g_{mn}^q = g_{mn} \left(e^{iqmd} + e^{iqnd} \right),$$

where g_{mn} is Hermitian and translational invariant, and d is the lattice constant. This form of the coupling constant can be shown to satisfy both the conjugate and translation relations: $g_{mn}^{q\,*} = g_{nm}^{-q}$ and $g_{mn}^q = e^{iqjd} g_{m-j,n-j}^q$, respectively. For simplicity, we consider e-ph coupling constants only up to the nearest-neighbor by setting $g_{mn} = g_0 \delta_{mn} + g_1 \delta_{m,n+1} + g_1^* \delta_{m,n-1}$, with g_0 real.

Polaron energy in untransformed basis

Assuming the off-diagonal components of $\exp[-\lambda_{mn}]$ are all damped out, by Eq. (4.17), the onsite polaron energy in this untransformed basis is given by

$$\Delta E_u = -\frac{1}{N_\Omega} \sum_q \omega_0 \left| g_{mm}^q \right|^2 = -\omega_0 \left| 2 g_0 \right|^2,$$

where q is summed over $j/N_\Omega \cdot 2\pi/d$, with integer $j = 0, \cdots, N_\Omega - 1$. A self-localized state is formed when the polaron energy is lower than the conduction band minimum, that is, when

$$\Delta E_u < -2t.$$

This is in analogy to what we checked in Section 4.4.

Polaron energy in transformed basis

Now we study the polaron energy in a transformed fermion basis using Eq. (4.18). To generate a unitary and translational invariant matrix U_{mn}, we set $U_{mn} = \exp[ih]_{mn}$, where h_{mn} is a Hermitian matrix with the general form of

$$h_{mn} = \begin{bmatrix} \alpha_0 & \alpha_1 & \alpha_2 & \alpha_3 & \cdots & \alpha_1^* \\ \alpha_1^* & \alpha_0 & \alpha_1 & \alpha_2 & \cdots & \alpha_2^* \\ \alpha_2^* & \alpha_1^* & \alpha_0 & \alpha_1 & \cdots & \alpha_3^* \\ \alpha_3^* & \alpha_2^* & \alpha_1^* & \alpha_0 & \cdots & \alpha_4^* \\ \vdots & \vdots & \vdots & \vdots & \ddots & \vdots \\ \alpha_1 & \alpha_2 & \alpha_3 & \alpha_4 & \cdots & \alpha_0 \end{bmatrix}.$$

For simplicity, in the following discussion, we set all the elements α_n to zero except for α_1, and we variate α_1 from 0 to i to see how the polaron energy depends on this basis change. Figure 4.5 shows the spread of the wavefunction amplitude $|U_{0n}|^2$ for three different values of α_1.

The polaron energy in this transformed basis is given by

$$\Delta E_t = -\frac{1}{N_\Omega} \sum_q \omega_0 \Big| \sum_{mn} U_{0m} g^q_{mn} U^\dagger_{n0} \Big|^2.$$

We plot the ratio of the polaron energy in the transformed basis to that in the untransformed basis, $\Delta E_t / |\Delta E_u|$ in Fig. 4.6 for four different values of g_1/g_0.

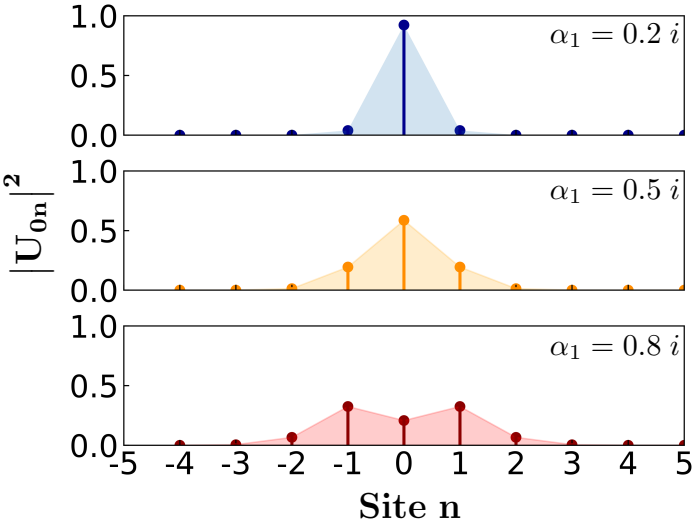

Figure 4.5: **Transformed polaron wavefunctions in the toy model.** The transformed wavefunction amplitude $|U_{0n}|^2$ on nearby sites n for three different values of α_1.

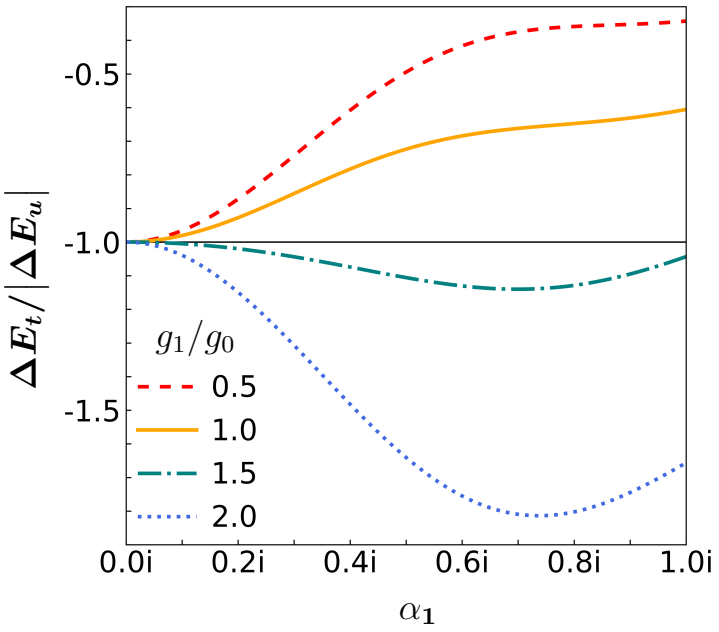

Figure 4.6: **Variation of polaron energy over different wavefunctions.** The ratio of the polaron energy in the transformed basis to that in the untransformed basis, $\Delta E_t/|\Delta E_u|$, for four different values of g_1/g_0. Values smaller than -1 indicate that the system favors the transformed wavefunction over the original one.

We can see that, before reaching a critical ratio for g_1/g_0, this set of transformed wavefunctions always render a higher energy than the untransformed one. On the other hand, as the nonlocal e-ph coupling constant g_1 becomes more or more important, some transformed wavefunctions are energetically more stable, and by performing the variation on the fermion basis, we can find the wavefunction with the lowest possible energy of the system.

References

[1] D. Emin, Phys. Today **35**, 34 (1982).

[2] S. Lany, J. Phys. Condens. Matter **27**, 283203 (2015).

[3] T. G. Castner and W. Känzig, J. Phys. Chem. Solids **3**, 178–195 (1957).

[4] L. B. Schein, C. B. Duke, and A. R. McGhie, Phys. Rev. Lett. **40**, 197–200 (1978).

[5] H. Tuller and A. Nowick, J. Phys. Chem. Solids **38**, 859–867 (1977).

[6] H. Sezen, H. Shang, F. Bebensee, C. Yang, M. Buchholz, A. Nefedov, S. Heissler, C. Carbogno, M. Scheffler, P. Rinke, and C. Wöll, Nat. Commun. **6**, 6901 (2015).

[7] E. Pastor, J.-S. Park, L. Steier, S. Kim, M. Grätzel, J. R. Durrant, A. Walsh, and A. A. Bakulin, Nat. Commun. **10**, 3962 (2019).

[8] J. Kang, Y. S. Jung, S.-H. Wei, and A. C. Dillon, Phys. Rev. B **85**, 035210 (2012).

[9] S. P. Ong, Y. Mo, and G. Ceder, Phys. Rev. B **85**, 081105 (2012).

[10] X. Wu, M. T. Trinh, D. Niesner, H. Zhu, Z. Norman, J. S. Owen, O. Yaffe, B. J. Kudisch, and X.-Y. Zhu, J. Am. Chem. Soc. **137**, 2089–2096 (2015).

[11] D. Cortecchia, J. Yin, A. Bruno, S.-Z. A. Lo, G. G. Gurzadyan, S. Mhaisalkar, J.-L. Brédas, and C. Soci, J. Mater. Chem. C **5**, 2771–2780 (2017).

[12] M. B. Salamon and M. Jaime, Rev. Mod. Phys. **73**, 583–628 (2001).

[13] T. Holstein, Ann. Phys. (N. Y.) **8**, 343–389 (1959).

[14] M. I. Dykman and E. I. Rashba, Phys. Today **68**, 10 (2015).

[15] I. G. Lang and Y. A. Firsov, J. Exptl. Theoret. Phys. (U.S.S.R.) **43**, 1843–1860 (1962).

[16] R. Silbey and R. W. Munn, J. Chem. Phys. **72**, 2763–2773 (1980).

[17] R. W. Munn and R. Silbey, J. Chem. Phys. **83**, 1843–1853 (1985).

[18] K. Hannewald, V. M. Stojanovi ć, J. M. T. Schellekens, P. A. Bobbert, G. Kresse, and J. Hafner, Phys. Rev. B **69**, 075211 (2004).

[19] V. N. Bogomolov, E. K. Kudinov, and Y. A. Firsov, Fiz. tverd. Tela **9**, 3175 (1967).

[20] H. Böttger and V. V. Bryksin, Phys. Status Solidi B **78**, 415–451 (1976).

[21] D. Emin, Phys. Rev. Lett. **28**, 604–607 (1972).

[22] W. Meevasana, X. J. Zhou, B. Moritz, C.-C. Chen, R. H. He, S.-I. Fujimori, D. H. Lu, S.-K. Mo, R. G. Moore, F. Baumberger, T. P. Devereaux, D. van der Marel, N. Nagaosa, J. Zaanen, and Z.-X. Shen, New J. Phys. **12**, 023004 (2010).

[23] D. Keroack, Y. Lepine, and J. L. Brebner, J. Phys. C: Solid State Phys. **17**, 833–842 (1984).

[24] M. L. Crespillo, J. T. Graham, F. Agulló-López, Y. Zhang, and W. J. Weber, Appl. Mater. Today **12**, 131–137 (2018).

[25] R. M. Martin, *"Electronic Structure: Basic Theory and Practical Methods"*, 1st ed. (Cambridge University Press, 2004).

[26] J. J. Kas, J. J. Rehr, and L. Reining, Phys. Rev. B **90**, 085112 (2014).

[27] J.-J. Zhou and M. Bernardi, Phys. Rev. B **94**, 201201 (2016).

[28] N.-E. Lee, J.-J. Zhou, L. A. Agapito, and M. Bernardi, Phys. Rev. B **97**, 115203 (2018).

[29] J.-J. Zhou, O. Hellman, and M. Bernardi, Phys. Rev. Lett. **121**, 226603 (2018).

[30] J.-J. Zhou and M. Bernardi, Phys. Rev. Research **1**, 033138 (2019).

[31] Y. Kang, H. Peelaers, and C. G. Van de Walle, Phys. Rev. B **100**, 121113 (2019).

[32] N.-E. Lee, J.-J. Zhou, H.-Y. Chen, and M. Bernardi, Nat. Commun. **11**, 1607 (2020).

[33] A. Janotti, J. B. Varley, M. Choi, and C. G. Van de Walle, Phys. Rev. B **90**, 085202 (2014).

[34] S. Kokott, S. V. Levchenko, P. Rinke, and M. Scheffler, New J. Phys. **20**, 033023 (2018).

[35] S. Yuan, Z. Wang, M. L. F. Baron, and K. H. Bevan, Phys. Rev. B **100**, 205201 (2019).

[36] N. Tsunoda, Y. Kumagai, and F. Oba, Phys. Rev. Materials **3**, 114602 (2019).

[37] J. T. Devreese, Preprint at arXiv:cond-mat/0004497 (2000).

[38] G. D. Mahan, *"Many-Particle Physics"*, 3rd ed. (Springer, 2000).

[39] N. Marzari, A. A. Mostofi, J. R. Yates, I. Souza, and D. Vanderbilt, Rev. Mod. Phys. **84**, 1419–1475 (2012).

[40] J.-J. Zhou, J. Park, I.-T. Lu, I. Maliyov, X. Tong, and M. Bernardi, Preprint at arXiv:2002.02045 (2020).

[41] P. Giannozzi et al., J. Phys. Condens. Matter **21**, 395502 (2009).

[42] N. Troullier and J. L. Martins, Phys. Rev. B **43**, 1993–2006 (1991).

[43] M. van Setten, M. Giantomassi, E. Bousquet, M. Verstraete, D. Hamann, X. Gonze, and G.-M. Rignanese, Comput. Phys. Commun. **226**, 39–54 (2018).

[44] J. P. Perdew, K. Burke, and M. Ernzerhof, Phys. Rev. Lett. **77**, 3865–3868 (1996).

[45] S. Baroni, S. de Gironcoli, A. Dal Corso, and P. Giannozzi, Rev. Mod. Phys. **73**, 515–562 (2001).

[46] A. A. Mostofi, J. R. Yates, G. Pizzi, Y.-S. Lee, I. Souza, D. Vanderbilt, and N. Marzari, Comput. Phys. Commun. **185**, 2309–2310 (2014).

[47] V. A. Jhalani, J.-J. Zhou, J. Park, C. E. Dreyer, and M. Bernardi, Phys. Rev. Lett. **125**, 136602 (2020).

[48] W. H. Duerig, Phys. Rev. **86**, 565–565 (1952).

[49] M. Setvin, C. Franchini, X. Hao, M. Schmid, A. Janotti, M. Kaltak, C. G. Van de Walle, G. Kresse, and U. Diebold, Phys. Rev. Lett. **113**, 086402 (2014).

[50] F. Freytag, G. Corradi, and M. Imlau, Sci. Rep. **6**, 36929 (2016).

Chapter 5

CONCLUSION AND FUTURE DIRECTIONS

In summary, this thesis presents research that investigates electron-phonon (*e*-ph) interactions and charge transport from first principles, paying attention to the organic molecular crystals, higher-order *e*-ph scattering processes, and formation of small polaron in materials with strong coupling strength.

Microscopic transport mechanism in organic molecular crystals

In Chapter 2, we compute the *e*-ph scattering rates and the phonon-limited hole mobility of naphthalene crystal in the framework of *ab initio* band theory. The computed mobilities dramatically improve the agreement with experiment compared to previous theoretical works, and they can accurately predict the temperature dependence between 100−300 K. We revisit the common belief that only rigid molecular motions affect carrier dynamics in organic molecular crystals, showing that scattering between intermolecular phonons and holes regulates the mobility while intramolecular phonons possess the strongest coupling with holes. The result in Chapter 2 is a first step toward reconciling band theory and charge hopping methods in quantum chemistry, and it shows that *ab initio* approaches based on band theory and many-body perturbation theory are well equipped to compute charge transport in organic semiconductors.

Beside naphthalene, many organic molecular crystals, for example, anthracene [1], durene [2], and rubrene [3], exhibit a bandlike power-law trend in their mobility. Yet, band theory has long been excluded from being a potential candidate for explaining their transport trend because the values of the mean free path in organic crystals are typically comparable to their unit cell size, which is thought to be the point where the BTE breaks down. The success of predicting the hole mobility in naphthalene is the revival of band theory in the organic community, but more evidence is required to consolidate its role played in those complex materials. As a result, a natural step to proceed is applying this novel workflow for transport calculation on different organic semiconductors. This will not only enable us to gain more control on designing novel organic technological applications, but will also provide insight into the underlying transport mechanism in organic molecular crystals.

Higher-order electron-phonon interactions

In Chapter 3, we derive next-to-leading order e-ph interactions, and compute from first principles the associated electron-two-phonon (2ph) scattering rates. The derivations involve Matsubara sums of two-loop Feynman diagrams, and the numerical challenges are overcome by using Monte Carlo integration together with a self-consistent update of the intermediate state lifetimes. We apply our method to GaAs, a weakly polar semiconductor with a dominant long-range e-ph interaction, and find that the 2ph scattering rates are as large as nearly half the value of the one-phonon (1ph) rates. Our analysis shows that the relative importance of the 2ph contributions is nearly temperature independent at 200−400 K, and rationalizes the peculiar energy dependence of the 2ph processes. In this chapter, we also formulate and iteratively solve the linearized BTE that incorporates the 2ph processes, which is shown to be indispensable to accurately predict the electron mobility in GaAs. This formalism proposes an approach broadly relevant to weakly polar semiconductors and high-mobility oxides, and sets the stage for systematically improving the accuracy of *ab initio* e-ph calculations beyond the leading order.

Nevertheless, the scattering processes considered in Chapter 3 are not complete even in the next-to-leading order perturbation expansion. As we pointed out in Section 3.3, the diagrams in Fig. 3.2 only involve the e-ph vertex shown in Fig. 5.1(a) that results from the first derivative of the KS potential with respect to lattice vibrations [see the expansion in Eq. (1.4)]. The next order of this KS potential expansion leads to the so-called Debye-Waller vertex [see Fig. 5.1(b)], which contributes a direct 2ph scattering process [see Fig. 5.1(d)] representing an electron interacting simultaneously with two phonons [4]. The impact of this direct 2ph scattering on the total scattering rates is still unknown, and whether it will give a strong cancellation for the acoustic phonons as people hypothesize deserves further examination.

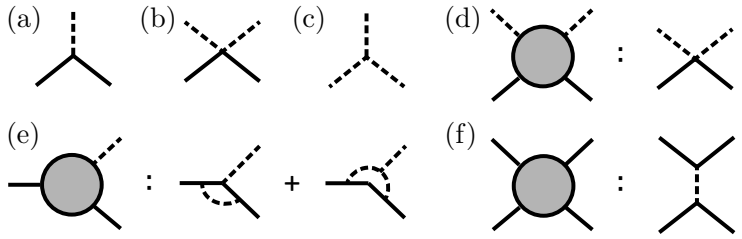

Figure 5.1: **More next-to-leading order vertices and scattering processes.** The figure shows in panels (a)−(c) some lowest order e-ph vertices and in panels (d)−(f) some additional amputated scattering processes.

Besides the expansion series of the KS potential, we also impose the harmonic approximation on the calculation on lattice dynamics in Eq. (1.3). Going one order beyond this harmonic approximation introduces the phonon-phonon interaction vertex shown in Fig. 5.1(c) [5]. Together with the lowest order e-ph interaction, they contribute two more 1ph scattering processes, shown in Fig. 5.1(e). These 1ph processes emerge also from the next-to-leading order self-energy diagrams, and effectively screen the bare e-ph coupling constant. Lastly, the last self-energy diagram in Fig. 3.1 gives rise to the electron-electron interaction shown in Fig. 5.1(f) similar to the Auger scattering; but instead of Coulomb potential, the two electrons interact with each other through exchanging a phonon. A thorough consideration on all these next-to-leading order scattering processes will provide more insights into the charge carrier dynamics, and puts the applicability of the perturbation expansion on a more solid ground.

Small polarons and their transport property

In Chapter 4, we show a formalism based on canonical transformations for computing the polaron formation energy using *ab initio* e-ph interactions. With a heuristic choice of the lattice distortion, we construct a self-trapped electronic state which is free from hopping and decoupled from all vibrational modes. Whether charge carriers in a material favor a localized small polaron state over a delocalized Bloch state can be inferred by a direct comparison of the calculated polaron energy with the conduction or valence band edge. The computational cost of this scheme is equivalent to a standard DFT calculation on a unit cell plus an inexpensive e-ph step. This efficiency allows us to easily investigate small polarons in several oxides and perovskites. The result in Chapter 4 bridges the gap between the small polaron theory and *ab initio* e-ph calculations and formulates an efficient computational approach to treat small polarons from first principles.

The formalism developed in Chapter 4 permits several straightforward extensions for better understanding the physical properties of small polarons. As elaborated in Chapter 4, this facile scheme utilizes a maximally-localized Wannier function as a trial state to estimate the polaron properties. A near-term extension would focus on obtaining the precise polaron formation energy and polaron wavefunction by performing a variation method outlined in Section 4.6. Another direction is applying the formalism on materials with transition metal that host small polarons, such as rutile [6] and lithium niobate [7]. Since transition metals have localized open d or f orbitals, hybrid functional or Hubbard correction DFT+U is usually indispensable

to correctly obtain their electronic properties. With a recent implementation that reconciles the DFPT and the DFT+U calculations, we can correctly compute the on-site *e*-ph coupling constant and thus extend the applicability of the polaron energy calculations to a broader range of materials.

A natural step beyond the energetic calculations is investigating the transport properties of small polarons. Small polaron transport theory developed using the Kubo formula [8–11] describes how these localized charge carriers hop between sites in response to an applied electric field. This is one of the most promising candidates to explaining the transport mechanism in materials with very low mobility. It can not only describe the thermally activated mobility trend, but also can predict the band-hopping transition observed in experiments [12–14]. Combing the *ab initio* *e*-ph calculation with this small polaron transport theory will provide more insights into the transport mechanism of materials in the hopping regime, and complement the usual band transport picture on the other side of the mobility spectrum.

References

[1] N. Karl, *"Organic semiconductors, Landolt-Börnstein Numerical Data and Functional Relationships in Science and Technology New Series - Group III Crystal and Solid State Physics"*, Vol. 17i (Springer-Verlag Berlin-Heidelberg, 1985).

[2] Z. Burshtein and D. F. Williams, J. Chem. Phys. **66**, 2746–2748 (1977).

[3] V. Podzorov, E. Menard, A. Borissov, V. Kiryukhin, J. A. Rogers, and M. E. Gershenson, Phys. Rev. Lett. **93**, 086602 (2004).

[4] P. Kocevar, *"Physics of Nonlinear Transport in Semiconductors"* (Springer US, 1980), pp. 167–174.

[5] M. Bernardi, Eur. Phys. J. B **89**, 239 (2016).

[6] M. Setvin, C. Franchini, X. Hao, M. Schmid, A. Janotti, M. Kaltak, C. G. Van de Walle, G. Kresse, and U. Diebold, Phys. Rev. Lett. **113**, 086402 (2014).

[7] F. Freytag, G. Corradi, and M. Imlau, Sci. Rep. **6**, 36929 (2016).

[8] T. Holstein, Ann. Phys. (N. Y.) **8**, 343–389 (1959).

[9] I. G. Lang and Y. A. Firsov, J. Exptl. Theoret. Phys. (U.S.S.R.) **43**, 1843–1860 (1962).

[10] R. Silbey and R. W. Munn, J. Chem. Phys. **72**, 2763–2773 (1980).

[11] G. D. Mahan, *"Many-Particle Physics"*, 3rd ed. (Springer, 2000).

[12] L. B. Schein, C. B. Duke, and A. R. McGhie, Phys. Rev. Lett. **40**, 197–200 (1978).

[13] V. N. Bogomolov, E. K. Kudinov, and Y. A. Firsov, Fiz. tverd. Tela **9**, 3175 (1967).

[14] H. Böttger and V. V. Bryksin, Phys. Status Solidi B **78**, 415–451 (1976).

Appendix A

ANALYTIC DERIVATION OF THE SCATTERING RATES OF TWO-PHONON PROCESSES

In this section, we calculate the contributions to the e-ph scattering rates from the next-to-leading-order self-energy diagrams. We use the Matsubara technique to calculate the two-loop self-energy, whose imaginary part is related to the total scattering rates via the optical theorem (see the figure below). Here and in the following, solid and dashed lines represent electron and phonon propagators, respectively. We focus on the scattering processes with two external phonons, corresponding to the three processes in the second row of the figure.

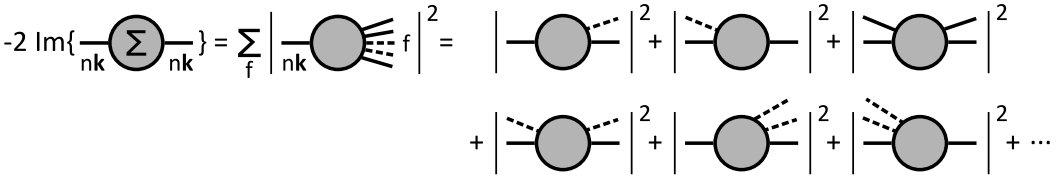

The Feynmann rules, which have been derived in Ref. [1], will be adapted here to our context. The starting point is the e-ph Hamiltonian

$$H = \sum_{n\mathbf{k}} \varepsilon_{n\mathbf{k}} a^\dagger_{n\mathbf{k}} a_{n\mathbf{k}} + \sum_{\nu\mathbf{q}} \omega_{\nu\mathbf{q}} \left(b^\dagger_{\nu\mathbf{q}} b_{\nu\mathbf{q}} + \frac{1}{2} \right) + \frac{1}{\sqrt{N_\Omega}} \sum_{mn\mathbf{k}} \sum_{\nu\mathbf{q}} g_{mn\nu}(\mathbf{k}, \mathbf{q}) \left(b^\dagger_{\nu-\mathbf{q}} + b_{\nu\mathbf{q}} \right) a^\dagger_{m\mathbf{k}+\mathbf{q}} a_{n\mathbf{k}},$$

where $a_{n\mathbf{k}}$ and $b_{\nu\mathbf{q}}$ are the annihilation operators for electrons and phonons with energies $\varepsilon_{n\mathbf{k}}$ and $\omega_{\nu\mathbf{q}}$, respectively, $g_{mn\nu}(\mathbf{k}, \mathbf{q})$ is the e-ph coupling constant, and N_Ω is the number of unit cells in the crystal. Comparing with Eqs. (2.67) and (3.200) in Ref. [1], we have introduced the dependence on electron crystal momentum $\mathbf{k}$ for the e-ph couplings and the electron band indices m and n. Also note that for the Hamiltonian to be Hermitian, the e-ph couplings must satisfy $g^*_{mn\nu}(\mathbf{k}, \mathbf{q}) = g_{nm\nu}(\mathbf{k}+\mathbf{q}, -\mathbf{q})$.

A.1 Feynmann Rules

The rules for constructing diagrams are listed in Section 3.4 of Ref. [1]. We slightly modify them here:

1. With each internal electron line, associate the propagator $\mathcal{G}^{(0)}(\mathbf{k}, ik_\lambda) = 1/(ik_\lambda - \xi_{n\mathbf{k}})$, where $\xi_{n\mathbf{k}} = \varepsilon_{n\mathbf{k}} - \mu$ and μ is the chemical potential.

2. With each internal phonon line, associate the propagator $\mathcal{D}^{(0)}(\mathbf{q}, i\omega_\kappa) = -2\omega_{\nu\mathbf{q}}/(\omega_\kappa^2 + \omega_{\nu\mathbf{q}}^2)$.

3. With each vertex, associate the e-ph coupling constant $g_{mn\nu}(\mathbf{k}, \mathbf{q})$. Beware of the direction of $\mathbf{q}$.

4. Conserve momentum and complex frequency at each vertex and sum over the internal degrees of freedom.

5. Multiply the expression by

$$\frac{(-1)^{L+F}(2S+1)^F}{(\beta N_\Omega)^L} = \left(-\frac{1}{\beta N_\Omega}\right)^L (-2)^F ,$$

where F is the number of closed Fermion loops. The $(2S + 1)$ factor is a summation over spin degrees of freedom, and $2S + 1 = 2$ for electrons. The integer L is the number of loops, and $\beta = 1/k_B T$, where T is temperature.

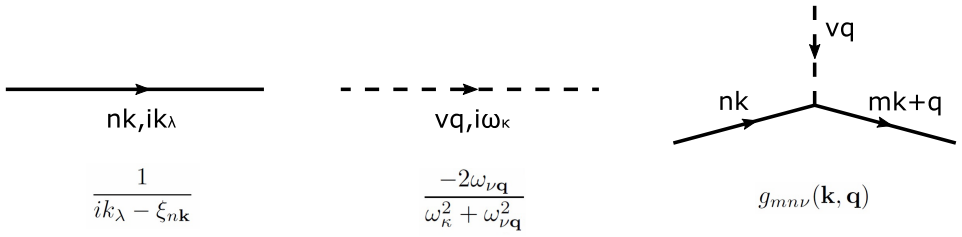

A.2 Electron Self-Energy

We consider below the 1-loop diagram that gives the lowest-order (one-phonon) self-energy and the three relevant two-loop diagrams for the electron self-energy. Diagram IIc will not contribute to the two-phonon processes and thus will not be considered in the following.

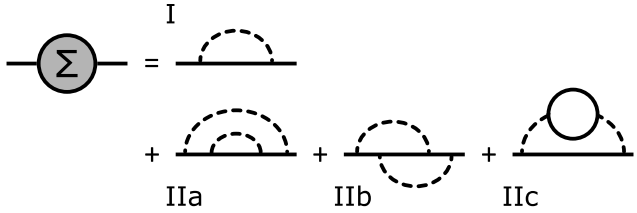

A.3 One-Loop Diagram I

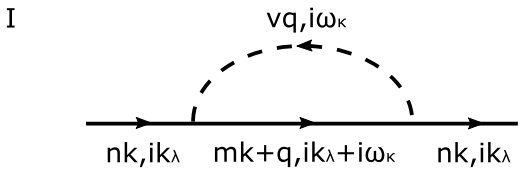

As a warm up exercise, we first derive the one-loop self-energy diagram, labelled as I in figure above. Since $L = 1$ and $F = 0$, the Feynman rules give

$$\begin{aligned}\Sigma^{(\mathrm{I})} &= -\frac{1}{\beta N_\Omega}\sum_{m\nu\mathbf{q}}\sum_{i\omega_\kappa} g_{mn\nu}(\mathbf{k},\mathbf{q})\mathcal{D}^{(0)}(\mathbf{q},i\omega_\kappa)\mathcal{G}^{(0)}(\mathbf{k}+\mathbf{q},ik_\lambda+i\omega_\kappa)g_{nm\nu}(\mathbf{k}+\mathbf{q},-\mathbf{q}) \\ &= -\frac{1}{\beta N_\Omega}\sum_{m\nu\mathbf{q}}\sum_{i\omega_\kappa} |g_{mn\nu}(\mathbf{k},\mathbf{q})|^2 \frac{-2\omega_{\nu\mathbf{q}}}{\omega_\kappa^2+\omega_{\nu\mathbf{q}}^2}\frac{1}{ik_\lambda+i\omega_\kappa-\xi_{m\mathbf{k}+\mathbf{q}}} \\ &\equiv \frac{1}{N_\Omega}\sum_{m\nu\mathbf{q}} |g_{mn\nu}(\mathbf{k},\mathbf{q})|^2 \left(-\frac{1}{\beta}\right)\sum_{i\omega_\kappa} f(i\omega_\kappa),\end{aligned}$$

where $f(z)$ is defined as

$$f(z) \equiv \frac{2\omega_{\nu\mathbf{q}}}{z^2-\omega_{\nu\mathbf{q}}^2}\,\frac{1}{z+ik_\lambda-\xi_{m\mathbf{k}+\mathbf{q}}}.$$

To apply the Matsubara frequency summation method, we define the bosonic weighting function as in Ref. [1]:

$$n_B(z) = \frac{1}{e^{\beta z}-1},$$

whose poles are at $i\omega_\kappa = i2\kappa\pi/\beta$, with residues $1/\beta$ and integer κ values. The weighting function for fermions is

$$n_F(z) = \frac{1}{e^{\beta z}+1},$$

whose poles are at $ik_\lambda = i(2\lambda+1)\pi/\beta$, with residues $-1/\beta$ and integer λ values.

For this diagram, we will do the contour integral for $f(z)n_B(z)$ at the complex infinity. Since $f(z)n_B(z)$ decays faster than $1/z$, we can apply the Cachy residue theorem, which gives (here and below, z' are the relevant poles):

$$\begin{aligned}0 &= \lim_{|z|\to\infty}\oint \frac{dz}{2\pi i} f(z)n_B(z) = \sum_{z' \text{ of } f\cdot n_B} \mathrm{Res}\{f(z')n_B(z')\} \\ &= \sum_{i\omega_\kappa} f(i\omega_\kappa)\frac{1}{\beta} + \sum_{z' \text{ of } f} \mathrm{Res}\{f(z')n_B(z')\}.\end{aligned}$$

Using this result, we get:

$$\Sigma^{(\mathrm{I})} = \frac{1}{N_\Omega} \sum_{m\nu\mathbf{q}} |g_{mn\nu}(\mathbf{k},\mathbf{q})|^2 \sum_{z' \text{ of } f} \mathrm{Res}\{f(z')\} n_B(z').$$

The poles of $f(z)$ are at $z_1 = \omega_{\nu\mathbf{q}}$, $z_2 = -\omega_{\nu\mathbf{q}}$, and $z_3 = -ik_\lambda + \xi_{m\mathbf{k+q}}$. Their residues are

$$\begin{aligned}
\mathrm{Res}\{f(z), z_1\} &= \frac{1}{\omega_{\nu\mathbf{q}} + ik_\lambda - \xi_{m\mathbf{k+q}}} \\
\mathrm{Res}\{f(z), z_2\} &= -\frac{1}{-\omega_{\nu\mathbf{q}} + ik_\lambda - \xi_{m\mathbf{k+q}}} \\
\mathrm{Res}\{f(z), z_3\} &= \frac{2\omega_{\nu\mathbf{q}}}{(-ik_\lambda + \xi_{m\mathbf{k+q}})^2 - \omega_{\nu\mathbf{q}}^2} \\
&= \frac{1}{-\omega_{\nu\mathbf{q}} + ik_\lambda - \xi_{m\mathbf{k+q}}} - \frac{1}{\omega_{\nu\mathbf{q}} + ik_\lambda - \xi_{m\mathbf{k+q}}}.
\end{aligned}$$

We also know that $n_B(z_1) = n_B(\omega_{\nu\mathbf{q}}) \equiv N_{\nu\mathbf{q}}$, $n_B(z_2) = n_B(-\omega_{\nu\mathbf{q}}) = -N_{\nu\mathbf{q}} - 1$ and $n_B(z_3) = -n_F(\xi_{m\mathbf{k+q}}) \equiv -f_{m\mathbf{k+q}}$, where N and f are the thermal occupation numbers for phonons and electrons, respectively. We also used the fact that $ik_\lambda = i(2\lambda+1)\pi/\beta$. Substituting this result in the self-energy expression, we get

$$\Sigma^{(\mathrm{I})} = \frac{1}{N_\Omega} \sum_{m\nu\mathbf{q}} |g_{mn\nu}(\mathbf{k},\mathbf{q})|^2 \left[\frac{N_{\nu\mathbf{q}} + f_{m\mathbf{k+q}}}{ik_\lambda + \omega_{\nu\mathbf{q}} - \xi_{m\mathbf{k+q}}} + \frac{1 + N_{\nu\mathbf{q}} - f_{m\mathbf{k+q}}}{ik_\lambda - \omega_{\nu\mathbf{q}} - \xi_{m\mathbf{k+q}}} \right].$$

Employing the analytic continuation $ik_\lambda \to E + i\eta$, we obtain the off-shell lowest-order e-ph self-energy:

$$\Sigma^{(\mathrm{I})}(E) = \frac{1}{N_\Omega} \sum_{m\nu\mathbf{q}} |g_{mn\nu}(\mathbf{k},\mathbf{q})|^2 \left[\frac{N_{\nu\mathbf{q}} + f_{m\mathbf{k+q}}}{E + \omega_{\nu\mathbf{q}} - \xi_{m\mathbf{k+q}} + i\eta} + \frac{1 + N_{\nu\mathbf{q}} - f_{m\mathbf{k+q}}}{E - \omega_{\nu\mathbf{q}} - \xi_{m\mathbf{k+q}} + i\eta} \right].$$

We will be mainly interested in the scattering rate at the electron energy $\xi_{n\mathbf{k}}$ and therefore we will set $E = \xi_{n\mathbf{k}}$ to obtain the on-shell self-energy for the state with band n and crystal momentum $\mathbf{k}$. Using the identity

$$\frac{1}{x + i\eta} = P\frac{1}{x} - i\pi\delta(x)$$

and Eq. (7.304) in Ref. [1], which states that the scattering rate Γ is obtained as $\Gamma = -2\mathrm{Im}\Sigma$, we get

$$\begin{aligned}
\Gamma^{(\mathrm{I})}_{n\mathbf{k}} = \frac{2\pi}{N_\Omega} \sum_{m\nu\mathbf{q}} |g_{mn\nu}(\mathbf{k},\mathbf{q})|^2 \big[&(N_{\nu\mathbf{q}} + f_{m\mathbf{k+q}})\delta(\xi_{n\mathbf{k}} + \omega_{\nu\mathbf{q}} - \xi_{m\mathbf{k+q}}) \\
&+ (1 + N_{\nu\mathbf{q}} - f_{m\mathbf{k+q}})\delta(\xi_{n\mathbf{k}} - \omega_{\nu\mathbf{q}} - \xi_{m\mathbf{k+q}}) \big].
\end{aligned}$$

This is the well-known lowest-order scattering rate commonly used in first-principles calculations.

A.4 Two-Loop Diagram IIa

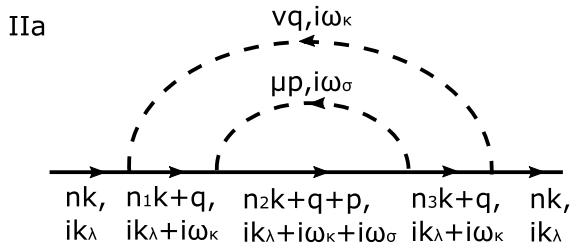

Now we compute the first two-loop diagram, which is shown in the figure above. Since $L = 2$ and $F = 0$, the Feynman rules give

$$\Sigma^{(\mathrm{IIa})} = \frac{1}{\beta^2 N_\Omega^2} \sum_{n_1 n_2 n_3} \sum_{\nu\mathbf{q}} \sum_{\mu\mathbf{p}} g_{n_1 n\nu}(\mathbf{k},\mathbf{q}) g^*_{n_3 n\nu}(\mathbf{k},\mathbf{q}) g_{n_2 n_1 \mu}(\mathbf{k}+\mathbf{q},\mathbf{p}) g^*_{n_2 n_3 \mu}(\mathbf{k}+\mathbf{q},\mathbf{p}) \times \sum_{i\omega_\kappa} \sum_{i\omega_\sigma} f(i\omega_\kappa, i\omega_\sigma),$$

where $f(i\omega_\kappa, i\omega_\sigma)$ is defined as

$$\begin{aligned} f(i\omega_\kappa, i\omega_\sigma) &\equiv \frac{1}{ik_\lambda + i\omega_\kappa - \xi_{n_1\mathbf{k}+\mathbf{q}}} \frac{1}{ik_\lambda + i\omega_\kappa + i\omega_\sigma - \xi_{n_2\mathbf{k}+\mathbf{q}+\mathbf{p}}} \\ &\quad \times \frac{1}{ik_\lambda + i\omega_\kappa - \xi_{n_3\mathbf{k}+\mathbf{q}}} \frac{2\omega_{\nu\mathbf{q}}}{\omega_\kappa^2 + \omega_{\nu\mathbf{q}}^2} \frac{2\omega_{\mu\mathbf{p}}}{\omega_\sigma^2 + \omega_{\mu\mathbf{p}}^2} \\ &\equiv A_\kappa \frac{1}{ik_\lambda + i\omega_\kappa + i\omega_\sigma - \xi_{n_2\mathbf{k}+\mathbf{q}+\mathbf{p}}} \frac{2\omega_{\mu\mathbf{p}}}{-(i\omega_\sigma)^2 + \omega_{\mu\mathbf{p}}^2}, \end{aligned}$$

where in A_κ we collect all terms independent of $i\omega_\sigma$. Let us sum over $i\omega_\sigma$ first. Performing the contour integral for $f(i\omega_\kappa, z) n_B(z)$ gives

$$\sum_{i\omega_\sigma} f(i\omega_\kappa, i\omega_\sigma) = -\beta \sum_{z' \text{ of } f} \mathrm{Res}\{f(i\omega_\kappa, z') n_B(z')\}.$$

Note that $f(i\omega_\kappa, z)$ has three poles, whose residues and bosonic weight factors are computed as:

$$\begin{aligned} z_1 &\to -ik_\lambda - i\omega_\kappa + \xi_{n_2\mathbf{k}+\mathbf{q}+\mathbf{p}} \\ \mathrm{Res}\{f(i\omega_\kappa, z_1)\} &= A_\kappa \left(\frac{1}{z_1 + \omega_{\mu\mathbf{p}}} - \frac{1}{z_1 - \omega_{\mu\mathbf{p}}} \right) \\ n_B(z_1) &= -f_{n_2\mathbf{k}+\mathbf{q}+\mathbf{p}} \\ \\ z_2 &\to \omega_{\mu\mathbf{p}} \\ \mathrm{Res}\{f(i\omega_\kappa, z_2)\} &= -A_\kappa \frac{1}{z_2 + ik_\lambda + i\omega_\kappa - \xi_{n_2\mathbf{k}+\mathbf{q}+\mathbf{p}}} \end{aligned}$$

$$
\begin{aligned}
n_B(z_2) &= N_{\mu\mathbf{p}} \\
z_3 &\to -\omega_{\mu\mathbf{p}} \\
\mathrm{Res}\{f(i\omega_\kappa, z_3)\} &= A_\kappa \frac{1}{z_3 + ik_\lambda + i\omega_\kappa - \xi_{n_2\mathbf{k+q+p}}} \\
n_B(z_3) &= -N_{\mu\mathbf{p}} - 1.
\end{aligned}
$$

Using these results, we get

$$
\begin{aligned}
&\sum_{i\omega_\sigma} f(i\omega_\kappa, i\omega_\sigma) \\
&\quad = \beta A_\kappa \frac{1 + N_{\mu\mathbf{p}} - f_{n_2\mathbf{k+q+p}}}{ik_\lambda + i\omega_\kappa - \xi_{n_2\mathbf{k+q+p}} - \omega_{\mu\mathbf{p}}} + \beta A_\kappa \frac{N_{\mu\mathbf{p}} + f_{n_2\mathbf{k+q+p}}}{ik_\lambda + i\omega_\kappa - \xi_{n_2\mathbf{k+q+p}} + \omega_{\mu\mathbf{p}}} \\
&\quad \equiv \beta h^{(-)}(i\omega_\kappa) + \beta h^{(+)}(i\omega_\kappa),
\end{aligned}
$$

where we defined two functions, $h^{(-)}(i\omega_\kappa)$ and $h^{(+)}(i\omega_\kappa)$, as the first and second terms in the expression above.

We then sum over $i\omega_\kappa$, using again

$$
\sum_{i\omega_\kappa} h^{(\pm)}(i\omega_\kappa) = -\beta \sum_{z' \text{ of } h^{(\pm)}} \mathrm{Res}\{h^{(\pm)}(z') n_B(z')\}.
$$

A subtle point is that the cases with $n_3 \neq n_1$ and $n_3 = n_1$ have different pole structures, and need to be discussed separately (see the figure above for diagram IIa; n_3 and n_1 label two intermediate electronic states in the self-energy diagram). Luckily, the two cases give the same expression for the two-phonon scattering processes, as we show explicitly below. Before carrying out the calculation, let us introduce some useful abbreviations. We will use in the following $\xi_{n_1\mathbf{k+q}} \equiv \xi_1$, $\xi_{n_1\mathbf{k+p}} \equiv \xi_{1\mathbf{p}}$, $f_{n_2\mathbf{k+q+p}} \equiv f_2$, $\omega_{\nu\mathbf{q}} \equiv \omega_{\mathbf{q}}$, etc.

Case with $\mathbf{n_3 \neq n_1}$

Let us focus on $h^{(-)}$ for the case $n_3 \neq n_1$ first. In this case, $h^{(-)}$ is defined as

$$
h^{(-)}(z) = \frac{1}{z + ik_\lambda - \xi_1} \; \frac{1}{z + ik_\lambda - \xi_3} \; \frac{-2\omega_{\mathbf{q}}}{z^2 - \omega_{\mathbf{q}}^2} \; \frac{1 + N_{\mathbf{p}} - f_2}{z + ik_\lambda - \xi_2 - \omega_{\mathbf{p}}}.
$$

It has five poles, which are given here together with their residues and bosonic weight factors:

$$
z_1 \to -ik_\lambda + \xi_1
$$

$$\begin{aligned}
\mathrm{Res}\{h^{(-)}(z_1)\} &= \frac{1}{\xi_1-\xi_3}\,\frac{1+N_{\mathbf{p}}-f_2}{\xi_1-\xi_2-\omega_{\mathbf{p}}}\left(\frac{1}{-ik_\lambda+\xi_1+\omega_{\mathbf{q}}}-\frac{1}{-ik_\lambda+\xi_1-\omega_{\mathbf{q}}}\right)\\
n_B(z_1) &= -f_1
\end{aligned}$$

$$\begin{aligned}
z_2 &\to -ik_\lambda+\xi_3\\
\mathrm{Res}\{h^{(-)}(z_2)\} &= \frac{1}{\xi_3-\xi_1}\,\frac{1+N_{\mathbf{p}}-f_2}{\xi_3-\xi_2-\omega_{\mathbf{p}}}\left(\frac{1}{-ik_\lambda+\xi_3+\omega_{\mathbf{q}}}-\frac{1}{-ik_\lambda+\xi_3-\omega_{\mathbf{q}}}\right)\\
n_B(z_2) &= -f_3
\end{aligned}$$

$$\begin{aligned}
z_3 &\to \omega_{\mathbf{q}}\\
\mathrm{Res}\{h^{(-)}(z_3)\} &= \frac{1}{ik_\lambda+\omega_{\mathbf{q}}-\xi_1}\,\frac{1}{ik_\lambda+\omega_{\mathbf{q}}-\xi_3}\,(-1)\,\frac{1+N_{\mathbf{p}}-f_2}{ik_\lambda+\omega_{\mathbf{q}}-\xi_2-\omega_{\mathbf{p}}}\\
n_B(z_3) &= N_{\mathbf{q}}
\end{aligned}$$

$$\begin{aligned}
z_4 &\to -\omega_{\mathbf{q}}\\
\mathrm{Res}\{h^{(-)}(z_4)\} &= \frac{1}{ik_\lambda-\omega_{\mathbf{q}}-\xi_1}\,\frac{1}{ik_\lambda-\omega_{\mathbf{q}}-\xi_3}\,\frac{1+N_{\mathbf{p}}-f_2}{ik_\lambda-\omega_{\mathbf{q}}-\xi_2-\omega_{\mathbf{p}}}\\
n_B(z_4) &= -N_{\mathbf{q}}-1
\end{aligned}$$

$$\begin{aligned}
z_5 &\to -ik_\lambda+\xi_2+\omega_{\mathbf{p}}\\
\mathrm{Res}\{h^{(-)}(z_5)\} &= \frac{1}{\xi_2+\omega_{\mathbf{p}}-\xi_1}\,\frac{1}{\xi_2+\omega_{\mathbf{p}}-\xi_3}\,(1+N_{\mathbf{p}}-f_2)\\
&\quad\times\left(\frac{1}{-ik_\lambda+\xi_2+\omega_{\mathbf{p}}+\omega_{\mathbf{q}}}-\frac{1}{-ik_\lambda+\xi_2+\omega_{\mathbf{p}}-\omega_{\mathbf{q}}}\right)\\
n_B(z_5) &= -\frac{N_{\mathbf{p}}f_2}{1+N_{\mathbf{p}}-f_2}.
\end{aligned}$$

After performing the same analysis on $h^{(+)}$ and adding them together, the terms related to the two-phonon processes, that is, the terms containing $1/(ik-\xi_2\pm\omega_{\mathbf{p}}\pm\omega_{\mathbf{q}})$, are collected here as

$$\begin{aligned}
&\frac{1}{\beta^2}\sum_{i\omega_\kappa}\sum_{i\omega_\sigma}f(i\omega_\kappa,i\omega_\sigma)=\\
&\quad\frac{1}{ik_\lambda-\xi_2-\omega_{\mathbf{p}}+\omega_{\mathbf{q}}}\left[\frac{1+N_{\mathbf{p}}-f_2}{ik_\lambda-\xi_1+\omega_{\mathbf{q}}}\frac{N_{\mathbf{q}}}{ik_\lambda-\xi_3+\omega_{\mathbf{q}}}+\frac{N_{\mathbf{p}}f_2}{\xi_2-\xi_1+\omega_{\mathbf{p}}}\frac{1}{\xi_2-\xi_3+\omega_{\mathbf{p}}}\right]\\
&+\frac{1}{ik_\lambda-\xi_2-\omega_{\mathbf{p}}-\omega_{\mathbf{q}}}\left[\frac{1+N_{\mathbf{p}}-f_2}{ik_\lambda-\xi_1-\omega_{\mathbf{q}}}\frac{1+N_{\mathbf{q}}}{ik_\lambda-\xi_3-\omega_{\mathbf{q}}}-\frac{N_{\mathbf{p}}f_2}{\xi_2-\xi_1+\omega_{\mathbf{p}}}\frac{1}{\xi_2-\xi_3+\omega_{\mathbf{p}}}\right]
\end{aligned}$$

$$+\frac{1}{ik_\lambda-\xi_2+\omega_{\mathbf{p}}+\omega_{\mathbf{q}}}\left[\frac{N_{\mathbf{p}}+f_2}{ik_\lambda-\xi_1+\omega_{\mathbf{q}}}\frac{N_{\mathbf{q}}}{ik_\lambda-\xi_3+\omega_{\mathbf{q}}}+\frac{f_2(1+N_{\mathbf{p}})}{\xi_2-\xi_1-\omega_{\mathbf{p}}}\frac{1}{\xi_2-\xi_3-\omega_{\mathbf{p}}}\right]$$
$$+\frac{1}{ik_\lambda-\xi_2+\omega_{\mathbf{p}}-\omega_{\mathbf{q}}}\left[\frac{N_{\mathbf{p}}+f_2}{ik_\lambda-\xi_1-\omega_{\mathbf{q}}}\frac{1+N_{\mathbf{q}}}{ik_\lambda-\xi_3-\omega_{\mathbf{q}}}-\frac{f_2(1+N_{\mathbf{p}})}{\xi_2-\xi_1-\omega_{\mathbf{p}}}\frac{1}{\xi_2-\xi_3-\omega_{\mathbf{p}}}\right]$$
$$+\cdots$$

The rates of the two-phonon processes emerge after analytically continuing ik_λ to $E+i\eta$ and taking the imaginary part of $1/(E-\xi_2\pm\omega_{\mathbf{p}}\pm\omega_{\mathbf{q}}+i\eta)$. We also use the delta functions to set $E=\xi_2\mp\omega_{\mathbf{p}}\mp\omega_{\mathbf{q}}$ in some of the denominators. After carrying out these calculations, we obtain

$$\mathrm{Im}\left\{\frac{1}{\beta^2}\sum_{i\omega_\kappa}\sum_{i\omega_\sigma}f(i\omega_\kappa,i\omega_\sigma)\right\}=$$
$$-i\pi\delta(E-\xi_2-\omega_{\mathbf{p}}+\omega_{\mathbf{q}})\frac{(1+N_{\mathbf{p}}-f_2)N_{\mathbf{q}}+N_{\mathbf{p}}f_2}{(\xi_2-\xi_1+\omega_{\mathbf{p}})(\xi_2-\xi_3+\omega_{\mathbf{p}})}$$
$$-i\pi\delta(E-\xi_2-\omega_{\mathbf{p}}-\omega_{\mathbf{q}})\frac{(1+N_{\mathbf{p}}-f_2)(1+N_{\mathbf{q}})-N_{\mathbf{p}}f_2}{(\xi_2-\xi_1+\omega_{\mathbf{p}})(\xi_2-\xi_3+\omega_{\mathbf{p}})}$$
$$-i\pi\delta(E-\xi_2+\omega_{\mathbf{p}}+\omega_{\mathbf{q}})\frac{(N_{\mathbf{p}}+f_2)N_{\mathbf{q}}+f_2(1+N_{\mathbf{p}})}{(\xi_2-\xi_1-\omega_{\mathbf{p}})(\xi_2-\xi_3-\omega_{\mathbf{p}})}$$
$$-i\pi\delta(E-\xi_2+\omega_{\mathbf{p}}-\omega_{\mathbf{q}})\frac{(N_{\mathbf{p}}+f_2)(1+N_{\mathbf{q}})-f_2(1+N_{\mathbf{p}})}{(\xi_2-\xi_1-\omega_{\mathbf{p}})(\xi_2-\xi_3-\omega_{\mathbf{p}})}.$$

Case with $\mathbf{n_3=n_1}$

In this case, $h^{(-)}$ is defined as

$$h^{(-)}(z)=\left(\frac{1}{z+ik_\lambda-\xi_1}\right)^2\frac{-2\omega_{\mathbf{q}}}{z^2-\omega_{\mathbf{q}}^2}\frac{1+N_{\mathbf{p}}-f_2}{z+ik_\lambda-\xi_2-\omega_{\mathbf{p}}}.$$

The function $h(z)n_B(z)$ has a pole of order 2 at $z_1=-ik_\lambda+\xi_1$. By employing

$$\mathrm{Res}\{f,z_1\}=\frac{1}{(n-1)!}\lim_{z\to z_1}\frac{d^{n-1}}{dz^{n-1}}\{(z-z_1)^n f(z)\},$$

where n is the order of the pole, we get

$$\mathrm{Res}\{h^{(-)}n_B,z_1\}=\frac{4z_1\omega_{\mathbf{q}}}{(z_1^2-\omega_{\mathbf{q}}^2)^2}\frac{1+N_{\mathbf{p}}-f_2}{z_1+ik_\lambda-\xi_2-\omega_{\mathbf{p}}}n_B(z_1)$$
$$+\frac{2\omega_{\mathbf{q}}}{z_1^2-\omega_{\mathbf{q}}^2}\frac{1+N_{\mathbf{p}}-f_2}{(z_1+ik_\lambda-\xi_2-\omega_{\mathbf{p}})^2}n_B(z_1)$$

$$+\frac{-2\omega_{\mathbf{q}}}{z_1^2-\omega_{\mathbf{q}}^2}\,\frac{1+N_{\mathbf{p}}-f_2}{z_1+ik_\lambda-\xi_2-\omega_{\mathbf{p}}}\,n_B'(z_1).$$

After substituting $z_1=-ik_\lambda+\xi_1$, $n_B(z_1)=-f_1$, and $n_B'(z_1)=\beta f_1(1-f_1)$, we get

$$\begin{aligned}\mathrm{Res}\{h^{(-)}n_B,z_1\}=&\frac{f_1(1+N_{\mathbf{p}}-f_2)}{(\xi_1-\xi_2-\omega_{\mathbf{p}})^2}\,\frac{-2\omega_{\mathbf{q}}}{(ik_\lambda-\xi_1)^2-\omega_{\mathbf{q}}^2}\\&+\frac{\beta f_1(1-f_1)(1+N_{\mathbf{p}}-f_2)}{\xi_1-\xi_2-\omega_{\mathbf{p}}}\,\frac{-2\omega_{\mathbf{q}}}{(ik_\lambda-\xi_1)^2-\omega_{\mathbf{q}}^2}\\&-\frac{f_1(1+N_{\mathbf{p}}-f_2)}{\xi_1-\xi_2-\omega_{\mathbf{p}}}\left[\frac{1}{(ik_\lambda-\xi_1+\omega_{\mathbf{q}})^2}-\frac{1}{(ik_\lambda-\xi_1-\omega_{\mathbf{q}})^2}\right].\end{aligned}$$

The other three poles are simple poles and can be treated in the usual way. Repeating this procedure for $h^{(+)}$ and adding all the contributions, we get

$$\begin{aligned}\frac{1}{\beta^2}\sum_{i\omega_\kappa}\sum_{i\omega_\sigma}f(i\omega_\kappa,i\omega_\sigma)=&\\&\frac{1}{ik_\lambda-\xi_2-\omega_{\mathbf{p}}+\omega_{\mathbf{q}}}\left[\frac{N_{\mathbf{q}}(1+N_{\mathbf{p}}-f_2)}{(ik_\lambda-\xi_1+\omega_{\mathbf{q}})^2}+\frac{N_{\mathbf{p}}f_2}{(\xi_2-\xi_1+\omega_{\mathbf{p}})^2}\right]\\&+\frac{1}{ik_\lambda-\xi_2-\omega_{\mathbf{p}}-\omega_{\mathbf{q}}}\left[\frac{(1+N_{\mathbf{q}})(1+N_{\mathbf{p}}-f_2)}{(ik_\lambda-\xi_1-\omega_{\mathbf{q}})^2}-\frac{N_{\mathbf{p}}f_2}{(\xi_2-\xi_1+\omega_{\mathbf{p}})^2}\right]\\&+\frac{1}{ik_\lambda-\xi_2+\omega_{\mathbf{p}}+\omega_{\mathbf{q}}}\left[\frac{N_{\mathbf{q}}(N_{\mathbf{p}}+f_2)}{(ik_\lambda-\xi_1+\omega_{\mathbf{q}})^2}+\frac{f_2\ (1+N_{\mathbf{p}})}{(\xi_2-\xi_1-\omega_{\mathbf{p}})^2}\right]\\&+\frac{1}{ik_\lambda-\xi_2+\omega_{\mathbf{p}}-\omega_{\mathbf{q}}}\left[\frac{(1+N_{\mathbf{q}})(N_{\mathbf{p}}+f_2)}{(ik_\lambda-\xi_1-\omega_{\mathbf{q}})^2}-\frac{f_2\ (1+N_{\mathbf{p}})}{(\xi_2-\xi_1-\omega_{\mathbf{p}})^2}\right]\\&+\cdots\end{aligned}$$

We perform the analytic continuation $ik_\lambda\to E+i\eta$, take the imaginary part of $1/(E-\xi_2\pm\omega_{\mathbf{p}}\pm\omega_{\mathbf{q}}+i\eta)$, and get

$$\begin{aligned}\mathrm{Im}\left\{\frac{1}{\beta^2}\sum_{i\omega_\kappa}\sum_{i\omega_\sigma}f(i\omega_\kappa,i\omega_\sigma)\right\}=&\\&-i\pi\delta(E-\xi_2-\omega_{\mathbf{p}}+\omega_{\mathbf{q}})\frac{1}{(\xi_2-\xi_1+\omega_{\mathbf{p}})^2}\left[(1+N_{\mathbf{p}}-f_2)N_{\mathbf{q}}+N_{\mathbf{p}}f_2\right]\\&-i\pi\delta(E-\xi_2-\omega_{\mathbf{p}}-\omega_{\mathbf{q}})\frac{1}{(\xi_2-\xi_1+\omega_{\mathbf{p}})^2}\left[(1+N_{\mathbf{p}}-f_2)(1+N_{\mathbf{q}})-N_{\mathbf{p}}f_2\right]\\&-i\pi\delta(E-\xi_2+\omega_{\mathbf{p}}+\omega_{\mathbf{q}})\frac{1}{(\xi_2-\xi_1-\omega_{\mathbf{p}})^2}\left[(N_{\mathbf{p}}+f_2)N_{\mathbf{q}}+f_2(1+N_{\mathbf{p}})\right]\\&-i\pi\delta(E-\xi_2+\omega_{\mathbf{p}}-\omega_{\mathbf{q}})\frac{1}{(\xi_2-\xi_1-\omega_{\mathbf{p}})^2}\left[(N_{\mathbf{p}}+f_2)(1+N_{\mathbf{q}})-f_2(1+N_{\mathbf{p}})\right].\end{aligned}$$

A.5 Two-Loop Diagram IIb

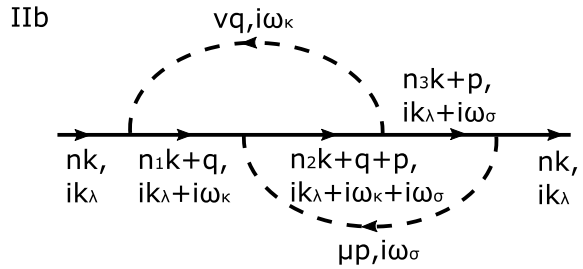

The second two-loop diagram, called here IIb, is shown in the figure above. Since this diagram also has $L = 2$ and $F = 0$, the Feynman rules give

$$\Sigma^{(\mathrm{IIb})} = \frac{1}{\beta^2 N_\Omega^2} \sum_{n_1 n_2 n_3} \sum_{\nu\mathbf{q}} \sum_{\mu\mathbf{p}} g_{n_1 n\nu}(\mathbf{k},\mathbf{q}) g^*_{n_2 n_3 \nu}(\mathbf{k}+\mathbf{p},\mathbf{q}) g_{n_2 n_1 \mu}(\mathbf{k}+\mathbf{q},\mathbf{p}) g^*_{n_3 n\mu}(\mathbf{k},\mathbf{p}) \times \sum_{i\omega_\kappa} \sum_{i\omega_\sigma} f(i\omega_\kappa, i\omega_\sigma),$$

where $f(i\omega_\kappa, i\omega_\sigma)$ is defined as

$$\begin{aligned} f(i\omega_\kappa, i\omega_\sigma) &\equiv \frac{1}{ik_\lambda + i\omega_\kappa - \xi_1} \frac{1}{ik_\lambda + i\omega_\kappa + i\omega_\sigma - \xi_2} \\ &\quad \times \frac{1}{ik_\lambda + i\omega_\sigma - \xi_{3\mathbf{p}}} \frac{2\omega_\mathbf{q}}{-\omega_\kappa^2 - \omega_\mathbf{q}^2} \frac{2\omega_\mathbf{p}}{-\omega_\sigma^2 - \omega_\mathbf{p}^2} \\ &\equiv A_\kappa \frac{1}{ik_\lambda + i\omega_\kappa + i\omega_\sigma - \xi_2} \frac{1}{ik_\lambda + i\omega_\sigma - \xi_{3\mathbf{p}}} \frac{2\omega_\mathbf{p}}{-\omega_\sigma^2 - \omega_\mathbf{p}^2}. \end{aligned}$$

Using a notation we introduced above, A_κ collects all terms independent of ω_σ, and we use again abbreviations introduced in the previous section, such as $\xi_{3\mathbf{p}} \equiv \xi_{n_3\mathbf{k}+\mathbf{p}}$, etc. Summing over $i\omega_\sigma$ first, we get

$$\begin{aligned} -\frac{1}{\beta} \sum_{i\omega_\sigma} f(i\omega_\kappa, i\omega_\sigma) = \\ & f_2 A_\kappa \frac{1}{i\omega_\kappa - \xi_2 + \xi_{3\mathbf{p}}} \left(\frac{1}{ik_\lambda + i\omega_\kappa - \xi_2 - \omega_\mathbf{p}} - \frac{1}{ik_\lambda + i\omega_\kappa - \xi_2 + \omega_\mathbf{p}} \right) \\ & + f_{3\mathbf{p}} A_\kappa \frac{1}{i\omega_\kappa - \xi_2 + \xi_{3\mathbf{p}}} \left(\frac{1}{ik_\lambda - \xi_{3\mathbf{p}} + \omega_\mathbf{p}} - \frac{1}{ik_\lambda - \xi_{3\mathbf{p}} - \omega_\mathbf{p}} \right) \\ & + N_\mathbf{p} A_\kappa \frac{1}{ik_\lambda + i\omega_\kappa - \xi_2 + \omega_\mathbf{p}} \frac{1}{ik_\lambda - \xi_{3\mathbf{p}} + \omega_\mathbf{p}} \\ & + (N_\mathbf{p} + 1) A_\kappa \frac{1}{ik_\lambda + i\omega_\kappa - \xi_2 - \omega_\mathbf{p}} \frac{1}{ik_\lambda - \xi_{3\mathbf{p}} - \omega_\mathbf{p}}. \end{aligned}$$

We then sum over $i\omega_\kappa$, and collect the relevant terms for two-phonon scattering processes. After performing the analytic continuation and taking the imaginary part, we get

$$\begin{aligned}
\mathrm{Im}\left\{\frac{1}{\beta^2}\sum_{i\omega_\kappa}\sum_{i\omega_\sigma} f(i\omega_\kappa, i\omega_\sigma)\right\} = \\
&-i\pi\delta(E-\xi_2-\omega_{\mathbf{p}}+\omega_{\mathbf{q}})\frac{N_{\mathbf{q}}+N_{\mathbf{q}}N_{\mathbf{p}}+N_{\mathbf{p}}f_2-N_{\mathbf{q}}f_2}{(\xi_2-\xi_1+\omega_{\mathbf{p}})(\xi_2-\xi_{3\mathbf{p}}-\omega_{\mathbf{q}})} \\
&-i\pi\delta(E-\xi_2-\omega_{\mathbf{p}}-\omega_{\mathbf{q}})\frac{(1+N_{\mathbf{p}})(1+N_{\mathbf{q}})-f_2(1+N_{\mathbf{p}}+N_{\mathbf{q}})}{(\xi_2-\xi_1+\omega_{\mathbf{p}})(\xi_2-\xi_{3\mathbf{p}}+\omega_{\mathbf{q}})} \\
&-i\pi\delta(E-\xi_2+\omega_{\mathbf{p}}+\omega_{\mathbf{q}})\frac{N_{\mathbf{p}}N_{\mathbf{q}}+N_{\mathbf{q}}f_2+N_{\mathbf{p}}f_2+f_2}{(\xi_2-\xi_1-\omega_{\mathbf{p}})(\xi_2-\xi_{3\mathbf{p}}-\omega_{\mathbf{q}})} \\
&-i\pi\delta(E-\xi_2+\omega_{\mathbf{p}}-\omega_{\mathbf{q}})\frac{N_{\mathbf{p}}+N_{\mathbf{q}}N_{\mathbf{p}}+N_{\mathbf{q}}f_2-N_{\mathbf{p}}f_2}{(\xi_2-\xi_1-\omega_{\mathbf{p}})(\xi_2-\xi_{3\mathbf{p}}+\omega_{\mathbf{q}})}.
\end{aligned}$$

A.6 Two-Phonon Scattering Rates

Collecting the contributions from diagrams IIa and IIb, using $\Gamma = -2\mathrm{Im}\Sigma$, and setting E to the band energy $\xi_{n\mathbf{k}}$, the scattering rate of the two-phonon processes becomes

$$\begin{aligned}
\Gamma^{(2\mathrm{ph})}_{n\mathbf{k}} = \frac{2\pi}{N_\Omega^2}\sum_{n_1n_2n_3}\sum_{\mathbf{qp}}\sum_{\nu\mu}\times \\
&\left[\gamma^{(\mathrm{i})}\delta(\xi_{n\mathbf{k}}-\xi_2-\omega_{\mathbf{p}}+\omega_{\mathbf{q}})+\gamma^{(\mathrm{ii})}\delta(\xi_{n\mathbf{k}}-\xi_2-\omega_{\mathbf{p}}-\omega_{\mathbf{q}})\right. \\
&\left.+\gamma^{(\mathrm{iii})}\delta(\xi_{n\mathbf{k}}-\xi_2+\omega_{\mathbf{p}}+\omega_{\mathbf{q}})+\gamma^{(\mathrm{iv})}\delta(\xi_{n\mathbf{k}}-\xi_2+\omega_{\mathbf{p}}-\omega_{\mathbf{q}})\right],
\end{aligned}$$

where we introduce the process amplitudes

$$\begin{aligned}
\gamma^{(\mathrm{i})} = \left(N_{\mathbf{q}}+N_{\mathbf{q}}N_{\mathbf{p}}+N_{\mathbf{p}}f_2-N_{\mathbf{q}}f_2\right)\frac{g_{n_1n\nu}(\mathbf{k},\mathbf{q})g_{n_2n_1\mu}(\mathbf{k}+\mathbf{q},\mathbf{p})}{\xi_2-\xi_1+\omega_{\mathbf{p}}} \\
\times\left(\frac{g^*_{n_3n\nu}(\mathbf{k},\mathbf{q})g^*_{n_2n_3\mu}(\mathbf{k}+\mathbf{q},\mathbf{p})}{\xi_2-\xi_3+\omega_{\mathbf{p}}}+\frac{g^*_{n_2n_3\nu}(\mathbf{k}+\mathbf{p},\mathbf{q})g^*_{n_3n\mu}(\mathbf{k},\mathbf{p})}{\xi_2-\xi_{3\mathbf{p}}-\omega_{\mathbf{q}}}\right)
\end{aligned}$$

$$\begin{aligned}
\gamma^{(\mathrm{ii})} = \left[(1+N_{\mathbf{q}})(1+N_{\mathbf{p}}-f_2)-N_{\mathbf{p}}f_2\right]\frac{g_{n_1n\nu}(\mathbf{k},\mathbf{q})g_{n_2n_1\mu}(\mathbf{k}+\mathbf{q},\mathbf{p})}{\xi_2-\xi_1+\omega_{\mathbf{p}}} \\
\times\left(\frac{g^*_{n_3n\nu}(\mathbf{k},\mathbf{q})g^*_{n_2n_3\mu}(\mathbf{k}+\mathbf{q},\mathbf{p})}{\xi_2-\xi_3+\omega_{\mathbf{p}}}+\frac{g^*_{n_2n_3\nu}(\mathbf{k}+\mathbf{p},\mathbf{q})g^*_{n_3n\mu}(\mathbf{k},\mathbf{p})}{\xi_2-\xi_{3\mathbf{p}}+\omega_{\mathbf{q}}}\right)
\end{aligned}$$

$$\gamma^{(\mathrm{iii})} = \left[N_{\mathbf{q}}(N_{\mathbf{p}}+f_2)+(1+N_{\mathbf{p}})f_2\right]\frac{g_{n_1n\nu}(\mathbf{k},\mathbf{q})g_{n_2n_1\mu}(\mathbf{k}+\mathbf{q},\mathbf{p})}{\xi_2-\xi_1-\omega_{\mathbf{p}}}$$
$$\times\left(\frac{g^*_{n_3n\nu}(\mathbf{k},\mathbf{q})g^*_{n_2n_3\mu}(\mathbf{k}+\mathbf{q},\mathbf{p})}{\xi_2-\xi_3-\omega_{\mathbf{p}}}+\frac{g^*_{n_2n_3\nu}(\mathbf{k}+\mathbf{p},\mathbf{q})g^*_{n_3n\mu}(\mathbf{k},\mathbf{p})}{\xi_2-\xi_{3\mathbf{p}}-\omega_{\mathbf{q}}}\right)$$

$$\gamma^{(\mathrm{iv})} = \left(N_{\mathbf{p}}+N_{\mathbf{q}}N_{\mathbf{p}}+N_{\mathbf{q}}f_2-N_{\mathbf{p}}f_2\right)\frac{g_{n_1n\nu}(\mathbf{k},\mathbf{q})g_{n_2n_1\mu}(\mathbf{k}+\mathbf{q},\mathbf{p})}{\xi_2-\xi_1-\omega_{\mathbf{p}}}$$
$$\times\left(\frac{g^*_{n_3n\nu}(\mathbf{k},\mathbf{q})g^*_{n_2n_3\mu}(\mathbf{k}+\mathbf{q},\mathbf{p})}{\xi_2-\xi_3-\omega_{\mathbf{p}}}+\frac{g^*_{n_2n_3\nu}(\mathbf{k}+\mathbf{p},\mathbf{q})g^*_{n_3n\mu}(\mathbf{k},\mathbf{p})}{\xi_2-\xi_{3\mathbf{p}}+\omega_{\mathbf{q}}}\right).$$

Now we restore the infinitesimal $i\eta$ for the intermediate propagators. A useful sanity check is that our finite temperature results should reduce to the zero temperature results in the $T\to 0$ limit, from which we check that the pole structure of the finite and zero temperature expressions are consistent with each other. At zero temperature, we can directly compute the scattering amplitude $\mathcal{M}$. The zero temperature Feynman rules {see Eqs. (2.124) to (2.127) in Ref. [1]} give

$$\mathcal{M}\sim\frac{gg}{E-\xi+i\eta}.$$

The scattering rate is proportional to the absolute square of the scattering amplitude:

$$\Gamma\sim|\mathcal{M}|^2\sim\left|\frac{gg}{E-\xi+i\eta}\right|^2.$$

Therefore, we will insert the infinitesimals in a way that allows us to express the scattering rates in an absolute square form. To achieve this, first note that quantities such as $\mathbf{q}$, $\mathbf{p}$, ν, and μ are dummy variables that are summed over or integrated, so we can rename them at will. Let us denote $(\nu\mathbf{q}\leftrightarrow\mu\mathbf{p})$ the term with its dummy variables swapped in the way indicated by the arrows, $\nu\leftrightarrow\mu$, $\mathbf{q}\leftrightarrow\mathbf{p}$, etc. Let us consider the processes with one phonon absorption and one phonon emission first, that is, the sum of terms (i) and (iv):

$$\sum_{n_1n_3}\left[\gamma^{(\mathrm{i})}\delta(\xi_{n\mathbf{k}}-\xi_2-\omega_{\mu\mathbf{p}}+\omega_{\nu\mathbf{q}})+\gamma^{(\mathrm{iv})}\delta(\xi_{n\mathbf{k}}-\xi_2+\omega_{\mu\mathbf{p}}-\omega_{\nu\mathbf{q}})\right]$$
$$=\sum_{n_1n_3}\Big[\gamma^{(\mathrm{i})}\delta(\xi_{n\mathbf{k}}-\xi_2-\omega_{\mu\mathbf{p}}+\omega_{\nu\mathbf{q}})$$
$$+\gamma^{(\mathrm{iv})}(\nu\mathbf{q}\leftrightarrow\mu\mathbf{p})\delta(\xi_{n\mathbf{k}}-\xi_2+\omega_{\mu\mathbf{p}}-\omega_{\nu\mathbf{q}})(\nu\mathbf{q}\leftrightarrow\mu\mathbf{p})\Big]$$
$$\equiv\ \gamma^{(1e1a)}\,\delta(\xi_{n\mathbf{k}}-\xi_2-\omega_{\mu\mathbf{p}}+\omega_{\nu\mathbf{q}}),$$

where

$$\begin{aligned}
\gamma^{(1e1a)} &= \sum_{n_1 n_3} \left[\gamma^{(\mathrm{i})} + \gamma^{(\mathrm{iv})}(\nu\mathbf{q} \leftrightarrow \mu\mathbf{p})\right] \\
&= \left(N_{\mathbf{q}} + N_{\mathbf{q}}N_{\mathbf{p}} + N_{\mathbf{p}}f_2 - N_{\mathbf{q}}f_2\right) \\
&\quad \times \sum_{n_1} \left(\frac{g_{n_1 n\nu}(\mathbf{k},\mathbf{q}) g_{n_2 n_1 \mu}(\mathbf{k}+\mathbf{q},\mathbf{p})}{\xi_2 - \xi_1 + \omega_{\mathbf{p}}} + \frac{g_{n_1 n\mu}(\mathbf{k},\mathbf{p}) g_{n_2 n_1 \nu}(\mathbf{k}+\mathbf{p},\mathbf{q})}{\xi_2 - \xi_{1\mathbf{p}} - \omega_{\mathbf{q}}} \right) \\
&\quad \times \sum_{n_3} \left(\frac{g^*_{n_3 n\nu}(\mathbf{k},\mathbf{q}) g^*_{n_2 n_3 \mu}(\mathbf{k}+\mathbf{q},\mathbf{p})}{\xi_2 - \xi_3 + \omega_{\mathbf{p}}} + \frac{g^*_{n_2 n_3 \nu}(\mathbf{k}+\mathbf{p},\mathbf{q}) g^*_{n_3 n\mu}(\mathbf{k},\mathbf{p})}{\xi_2 - \xi_{3\mathbf{p}} - \omega_{\mathbf{q}}} \right) \\
&= \left(N_{\mathbf{q}} + N_{\mathbf{q}}N_{\mathbf{p}} + N_{\mathbf{p}}f_2 - N_{\mathbf{q}}f_2\right) \\
&\quad \times \left| \sum_{n_1} \left(\frac{g_{n_1 n\nu}(\mathbf{k},\mathbf{q}) g_{n_2 n_1 \mu}(\mathbf{k}+\mathbf{q},\mathbf{p})}{\xi_2 - \xi_1 + \omega_{\mathbf{p}} + i\eta} + \frac{g_{n_1 n\mu}(\mathbf{k},\mathbf{p}) g_{n_2 n_1 \nu}(\mathbf{k}+\mathbf{p},\mathbf{q})}{\xi_2 - \xi_{1\mathbf{p}} - \omega_{\mathbf{q}} + i\eta} \right) \right|^2 .
\end{aligned}$$

Since the expression is already in square form, we have inserted the $i\eta$ terms in a way that makes the expression become an absolute square. Using a similar approach for the process in which the electron emits two phonons,

$$\begin{aligned}
\gamma^{(2e)} &= \sum_{n_1 n_3} \gamma^{(\mathrm{ii})} = \sum_{n_1 n_3} \frac{1}{2}\left[\gamma^{(\mathrm{ii})} + \gamma^{(\mathrm{ii})}\right] = \sum_{n_1 n_3} \frac{1}{2}\left[\gamma^{(\mathrm{ii})} + \gamma^{(\mathrm{ii})}(\nu\mathbf{q} \leftrightarrow \mu\mathbf{p})\right] \\
&= \frac{1}{2}\left[(1+N_{\mathbf{q}})(1+N_{\mathbf{p}} - f_2) - N_{\mathbf{p}}f_2\right] \\
&\quad \times \left| \sum_{n_1} \left(\frac{g_{n_1 n\nu}(\mathbf{k},\mathbf{q}) g_{n_2 n_1 \mu}(\mathbf{k}+\mathbf{q},\mathbf{p})}{\xi_2 - \xi_1 + \omega_{\mathbf{p}} + i\eta} + \frac{g_{n_1 n\mu}(\mathbf{k},\mathbf{p}) g_{n_2 n_1 \nu}(\mathbf{k}+\mathbf{p},\mathbf{q})}{\xi_2 - \xi_{1\mathbf{p}} + \omega_{\mathbf{q}} + i\eta} \right) \right|^2 ,
\end{aligned}$$

and for the process in which the electron absorbs two phonons,

$$\begin{aligned}
\gamma^{(2a)} &= \sum_{n_1 n_3} \gamma^{(\mathrm{iii})} = \sum_{n_1 n_3} \frac{1}{2}\left[\gamma^{(\mathrm{iii})} + \gamma^{(\mathrm{iii})}\right] = \sum_{n_1 n_3} \frac{1}{2}\left[\gamma^{(\mathrm{iii})} + \gamma^{(\mathrm{iii})}(\nu\mathbf{q} \leftrightarrow \mu\mathbf{p})\right] \\
&= \frac{1}{2}\left[N_{\mathbf{q}}(N_{\mathbf{p}} + f_2) + (1+N_{\mathbf{p}})f_2\right] \\
&\quad \times \left| \sum_{n_1} \left(\frac{g_{n_1 n\nu}(\mathbf{k},\mathbf{q}) g_{n_2 n_1 \mu}(\mathbf{k}+\mathbf{q},\mathbf{p})}{\xi_2 - \xi_1 - \omega_{\mathbf{p}} + i\eta} + \frac{g_{n_1 n\mu}(\mathbf{k},\mathbf{p}) g_{n_2 n_1 \nu}(\mathbf{k}+\mathbf{p},\mathbf{q})}{\xi_2 - \xi_{1\mathbf{p}} - \omega_{\mathbf{q}} + i\eta} \right) \right|^2 .
\end{aligned}$$

We thus get:

$$\begin{aligned}
\Gamma^{(2ph)}_{n\mathbf{k}} = \frac{2\pi}{N_\Omega^2} \sum_{n_2} \sum_{\mathbf{q}\,\mathbf{p}} \sum_{\nu\mu} \Big[&\gamma^{(1e1a)} \delta(\xi_{n\mathbf{k}} - \xi_2 - \omega_{\mathbf{p}} + \omega_{\mathbf{q}}) \\
&+ \gamma^{(2e)} \delta(\xi_{n\mathbf{k}} - \xi_2 - \omega_{\mathbf{p}} - \omega_{\mathbf{q}}) + \gamma^{(2a)} \delta(\xi_{n\mathbf{k}} - \xi_2 + \omega_{\mathbf{p}} + \omega_{\mathbf{q}}) \Big] .
\end{aligned}$$

A.7 Resonance

The last expression is very close to the final result given in Eqs. (3.1)−(3.4). The last problem we need to solve is that the sum giving $\Gamma^{(2\text{ph})}_{n\mathbf{k}}$ in the expression above diverges when the intermediate electron state is on shell, in which case the denominator in the γ terms given above vanishes, resulting in a divergent scattering rate. This phenomenon is called resonance. The problem is that the intermediate state will eventually transition into a different state, but using free propagators $1/(E-\xi+i\eta)$ for the on shell intermediate states implies an infinite intermediate state lifetime. The common practice in this situation, which also arises in other quantum field theories, is to consider the full electron propagator $1/(E-\xi+i\eta-\Sigma)$ as shown in the figure below, which introduces a finite lifetime for the intermediate electronic state. Diagramatically, this approach is equivalent to performing a resummation of diagrams to all orders, as is done in the well-known GW self-energy {see Eq. (5.54) in Ref. [1]}. For our 2ph scattering rate expression, we simply add the intermediate state self-energy in the denominators of all the γ terms above, which removes the divergences.

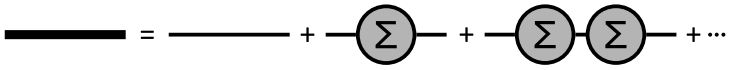

A.8 Summary

We rewrite the expression in more compact form. Defining the momentum of the final electronic state as $\mathbf{k}' \equiv \mathbf{k}+\mathbf{q}+\mathbf{p}$, and using the following constants

$$\alpha^{(1e1a)}_{\mathbf{p}} = \quad 1, \;\; \alpha^{(2e)}_{\mathbf{p}} = 1, \;\; \alpha^{(2a)}_{\mathbf{p}} = -1, \;\; \alpha^{(1e1a)}_{\mathbf{q}} = -1, \;\; \alpha^{(2e)}_{\mathbf{q}} = 1, \;\; \alpha^{(2a)}_{\mathbf{q}} = -1,$$

we can write

$$\Gamma^{(2\text{ph})}_{n\mathbf{k}} = \frac{2\pi}{N_\Omega^2} \sum_{n_2} \sum_{\nu\mathbf{q}} \sum_{\mu\mathbf{p}} \left[\widetilde{\Gamma}^{(1e1a)} + \widetilde{\Gamma}^{(2e)} + \widetilde{\Gamma}^{(2a)} \right],$$

where

$$\widetilde{\Gamma}^{(\text{i})} = \gamma^{(\text{i})} \; \delta(\xi_{n\mathbf{k}} - \xi_{n_2\mathbf{k}'} - \alpha^{(\text{i})}_{\mathbf{p}} \omega_{\mu\mathbf{p}} - \alpha^{(\text{i})}_{\mathbf{q}} \omega_{\nu\mathbf{q}}).$$

The square amplitudes $\gamma^{(\text{i})}$ for the different processes, i = 1e1a, 2e and 2a, are defined as

$$\gamma^{(\text{i})} = A^{(\text{i})} \left| \sum_{n_1} \left(\frac{g_{n_1 n\nu}(\mathbf{k},\mathbf{q}) g_{n_2 n_1 \mu}(\mathbf{k}+\mathbf{q},\mathbf{p})}{\xi_{n_2\mathbf{k}'} - \xi_{n_1\mathbf{k}+\mathbf{q}} + \alpha^{(\text{i})}_{\mathbf{p}} \omega_{\mu\mathbf{p}} + i\eta - \Sigma_{n_1\mathbf{k}+\mathbf{q}}} \right. \right.$$

$$+\frac{g_{n_1 n\mu}(\mathbf{k},\mathbf{p})\,g_{n_2 n_1 \nu}(\mathbf{k}+\mathbf{p},\mathbf{q})}{\xi_{n_2\mathbf{k}'}-\xi_{n_1\mathbf{k}+\mathbf{p}}+\alpha^{(\mathrm{i})}_{\mathbf{q}}\omega_{\nu\mathbf{q}}+i\eta-\Sigma_{n_1\mathbf{k}+\mathbf{p}}}\Bigg)\Bigg|^2,$$

where we have taken into account the resonance by adding the intermediate state self-energy in the denominators. The factors of $A^{(\mathrm{i})}$ contain the thermal occupation numbers of electrons and phonons, and are defined as

$$A^{(1\mathrm{e}1\mathrm{a})} = N_{\nu\mathbf{q}} + N_{\nu\mathbf{q}}N_{\mu\mathbf{p}} + N_{\mu\mathbf{p}}f_{n_2\mathbf{k}'} - N_{\nu\mathbf{q}}f_{n_2\mathbf{k}'},$$

$$A^{(2\mathrm{e})} = \frac{1}{2}\left[(1+N_{\nu\mathbf{q}})(1+N_{\mu\mathbf{p}}-f_{n_2\mathbf{k}'}) - N_{\mu\mathbf{p}}f_{n_2\mathbf{k}'}\right],$$

$$A^{(2\mathrm{a})} = \frac{1}{2}\left[N_{\nu\mathbf{q}}(N_{\mu\mathbf{p}}+f_{n_2\mathbf{k}'}) + (1+N_{\mu\mathbf{p}})f_{n_2\mathbf{k}'}\right].$$

These are our final expressions for the two-phonon scattering rates given in Eqs. (3.1)−(3.4) once the electron energy ξ is renamed to ε.

References

[1] G. D. Mahan, *"Many-Particle Physics"*, 3rd ed. (Springer, 2000).

Appendix B

BOLTZMANN TRANSPORT EQUATION WITH TWO-PHONON CONTRIBUTIONS

B.1 Summary

We briefly summarize the formulation of the linearized Boltzmann transport equation (BTE) incorporating the two-phonon (2ph) scattering processes here, whose derivation will be presented in the next section. Defining the total e-ph scattering rate as

$$\Gamma_{n\mathbf{k}} = \Gamma^{(1\mathrm{ph})}_{n\mathbf{k}} + \Gamma^{(2\mathrm{ph})}_{n\mathbf{k}} \equiv \frac{1}{N_\Omega}\sum_{m}\sum_{\nu\mathbf{q}} \widetilde{\Gamma}^{(1\mathrm{ph})}_{n\mathbf{k},\,\nu\mathbf{q}} + \frac{1}{N_\Omega^2}\sum_{n_2}\sum_{\nu\mathbf{q}}\sum_{\mu\mathbf{p}} \widetilde{\Gamma}^{(2\mathrm{ph})}_{n\mathbf{k},\,\nu\mathbf{q},\,\mu\mathbf{p}} \ ,$$

the linearized BTE can be expressed as

$$\mathbf{F}_{n\mathbf{k}} = \mathbf{F}^0_{n\mathbf{k}} + \tau_{n\mathbf{k}}\left[\frac{1}{N_\Omega}\sum_{m}\sum_{\nu\mathbf{q}} \mathbf{F}_{m\mathbf{k}+\mathbf{q}}\widetilde{\Gamma}^{(1\mathrm{ph})}_{n\mathbf{k},\,\nu\mathbf{q}} + \frac{1}{N_\Omega^2}\sum_{n_2}\sum_{\nu\mathbf{q}}\sum_{\mu\mathbf{p}} \mathbf{F}_{n_2\mathbf{k}'}\widetilde{\Gamma}^{(2\mathrm{ph})}_{n\mathbf{k},\,\nu\mathbf{q},\,\mu\mathbf{p}}\right], \tag{B.1}$$

where the relaxation time $\tau_{n\mathbf{k}}$ is the inverse of the total scattering rate, namely $\tau_{n\mathbf{k}} = 1/\Gamma_{n\mathbf{k}}$, and the first and second terms in brackets are due to the one-phonon (1ph) and 2ph scattering processes, respectively. The function $\mathbf{F}_{n\mathbf{k}}$ is the unknown in the equation, and $\mathbf{F}^0_{n\mathbf{k}} = \tau_{n\mathbf{k}}\mathbf{v}_{n\mathbf{k}}$, with $\mathbf{v}_{n\mathbf{k}}$ the band velocity. After solving the equation, the electrical mobility in direction i can be obtained using Eq. (1.6), which is repeated here as

$$\mu^i = \frac{2e\beta}{n_c V_{\mathrm{uc}}}\sum_{n\mathbf{k}} f_{n\mathbf{k}}(1-f_{n\mathbf{k}})v^i_{n\mathbf{k}}F^i_{n\mathbf{k}},$$

where V_{uc} is the unit cell volume and n_c the charge carrier concentration.

Since the BTE is a nonlinear integro-differential equation, exact solution is usually not obtainable. A common approach to computing $\mathbf{F}_{n\mathbf{k}}$ is the relaxation time approximation (RTA), which neglects the second term on the right hand side of Eq. (B.1) and approximates $\mathbf{F}_{n\mathbf{k}}$ to $\mathbf{F}^0_{n\mathbf{k}}$. A more accurate solution can be systematically obtained through an iterative approach (ITA). This method has been applied to study various transport properties like the thermal conductivity [1–3] and electrical conductivity [4–9]. Starting from the RTA solution $\mathbf{F}_{n\mathbf{k}} = \mathbf{F}^0_{n\mathbf{k}}$, one iteratively

substitutes $\mathbf{F}_{n\mathbf{k}}$ on the right hand side of Eq. (B.1) to obtain an updated $\mathbf{F}_{n\mathbf{k}}$, until a converged $\mathbf{F}_{n\mathbf{k}}$ is reached.

Our work in Chapter 3 presents calculations, both within the RTA and ITA, in which the 2ph processes are either included or neglected; when only 1ph processes are included, $\tau_{n\mathbf{k}}$ is set to the inverse of $\Gamma^{(1\text{ph})}_{n\mathbf{k}}$, and the second term in brackets in Eq. (B.1) is neglected. The ITA with 2ph contributions included is the most accurate level of theory, and the one that agrees best with experiment, while the ITA with only 1ph processes overestimates the experimental result. Note that interference between 2ph processes is neglected in the mobility calculation. This is a good approximation if for most of the ($\mathbf{q}$, $\mathbf{p}$) pairs, there is only one process in Eq. (3.3) that dominates, as in the case of GaAs that we have verified.

B.2 Derivation of the Boltzmann Transport Equation with Two-Phonon Scattering Precesses

In this section, we display the analytic derivation of the linearized BTE incorporating both the 1ph and 2ph processes shown in Eq. (B.1). The BTE represents the conservation of total particle number in the phase space [10] and governs the evolution of an out-of-equilibrium system:

$$\frac{df_\lambda}{dt} = \frac{\partial f_\lambda}{\partial t} + \mathbf{v}\cdot\boldsymbol{\nabla}_{\mathbf{r}} f_\lambda + \frac{\partial \mathbf{k}}{\partial t}\cdot\boldsymbol{\nabla}_{\mathbf{k}} f_\lambda = \left.\frac{df_\lambda}{dt}\right|_{\text{scat}},$$

where the distribution function f_λ describes the probability of particles occupying a state λ and the last term accounts for changes of particle distribution due to collisions. Assuming that the system reaches a steady state and with no diffusion, the equation becomes

$$-e\mathbf{E}\cdot\boldsymbol{\nabla}_{\mathbf{k}} f_\lambda = -\left.\frac{df_\lambda}{dt}\right|_{\text{scat}} \tag{B.2}$$

under an external electric field $\mathbf{E}$, where e is the electron charge $e = -|e|$.

Next, we linearize this equation with respect to the electric field. Suppose the electric field is small and the system just slightly deviates from its thermal equilibrium. Then the distribution function can be expanded around its equilibrium value:

$$\begin{aligned} f_\lambda &= f^0_\lambda + f^1_\lambda + O(E^2) \\ &\equiv f^0_\lambda - e\mathbf{E}\cdot\mathbf{F}_\lambda \frac{\partial f^0_\lambda}{\partial \varepsilon_\lambda} + O(E^2) \\ &= f^0_\lambda + e\mathbf{E}\cdot\mathbf{F}_\lambda f^0_\lambda \left(1 - f^0_\lambda\right)\beta + O(E^2), \end{aligned} \tag{B.3}$$

where f_λ^0 is the Fermi-Dirac distribution for the electronic state λ, ε_λ is the electron energy relative to the chemical potential, and $\beta = 1/k_\mathrm{B}T$ is the temperature inverse with k_B the Boltzmann constant. The function $\mathbf{F}_\lambda$ will be interpreted as the mean free displacement later, while for now it is just a parametrization for the first order deviation. Substituting the expansion in Eq. (B.3) into Eq. (B.2) and keep terms only up to the first order of $\mathbf{E}$, the left hand side becomes

$$-e\mathbf{E}\cdot\boldsymbol{\nabla}_\mathbf{k} f_\lambda \;\simeq\; -e\mathbf{E}\cdot\boldsymbol{\nabla}_\mathbf{k} f_\lambda^0 \;=\; \beta e\mathbf{E}\cdot\mathbf{v}_\lambda f_\lambda^0\left(1-f_\lambda^0\right), \tag{B.4}$$

where $\mathbf{v}_\lambda$ is the band velocity and $\hbar$ is set to unity.

The right hand side of Eq. (B.2) is the total rate of change of the distribution function due to all kinds of scattering processes [3]:

$$\begin{aligned} -\left.\frac{df_\lambda}{dt}\right|_\mathrm{scat} &= \sum_{\lambda'\alpha}\left(P_{\lambda\leftrightarrow\lambda'\alpha}+P_{\lambda\alpha\leftrightarrow\lambda'}\right) \\ &\quad+\sum_{\lambda'\alpha\alpha'}\left(P_{\lambda\leftrightarrow\lambda'\alpha\alpha'}+P_{\lambda\alpha\alpha'\leftrightarrow\lambda'}+P_{\lambda\alpha\leftrightarrow\lambda'\alpha'}\right)+\cdots, \end{aligned} \tag{B.5}$$

where P is the net rate of change of f_λ due to transition between states on the two sides of the arrow. For example, $P_{\lambda\leftrightarrow\lambda'\alpha}$ is the difference between the rate of the state λ making a transition to states $\lambda'\alpha$ and the rate of its reverse process. In our particular e-ph case, we use λ and λ' to label electron states, and α and α' to label phonon states. The terms listed above are the two lowest order e-ph scattering processes, and will be discussed in detail below.

First order scattering

The first two terms in Eq. (B.5) cover processes involving one phonon emission or absorption. The first term can be expressed as

$$P_{\lambda\leftrightarrow\lambda'\alpha} = f_\lambda\left(1-f_{\lambda'}\right)\left(1+N_\alpha\right)L_\lambda^{\lambda'\alpha} - \left(1-f_\lambda\right)f_{\lambda'}N_\alpha L_{\lambda'\alpha}^{\lambda}. \tag{B.6}$$

Here, N_α is the distribution function for phonon in state α. Since the electric field does not affect phonons, we assume that all the phonons are in thermal equilibrium and replace N_α with the Bose-Einstein distribution N_α^0. The intrinsic transition rate is denoted as L with the initial and final states indicated by its lower and upper indices, respectively. To satisfy the microscopic reversibility, the value of L should be unchanged if we swap its initial and the final states. For example, $L_\lambda^{\lambda'\alpha} = L_{\lambda'\alpha}^{\lambda}$.

Note that if there is no electric field and the system reaches thermal equilibrium, $P_{\lambda\leftrightarrow\lambda'\alpha}$ should vanish. This is called the detailed balance, and can be explicitly

checked for Eq. (B.6):

$$f_\lambda^0\left(1-f_{\lambda-\alpha}^0\right)\left(1+N_\alpha^0\right)=\left(1-f_\lambda^0\right)f_{\lambda-\alpha}^0 N_\alpha^0.$$

Here, $f_{\lambda-\alpha}^0$ is a shorthand for the Fermi-Dirac distribution of state with energy $\varepsilon_\lambda-\omega_\alpha$, where ω_α is the energy of phonon in state α. Analogous abbreviations will be applied in the following.

Next, we linearize Eq. (B.6) by substituting the expansion in Eq. (B.3). Using the detailed balance and keeping terms up to the first order of $\mathbf{E}$, we get

$$\begin{aligned}P_{\lambda\leftrightarrow\lambda'\alpha}&\simeq\left[f_\lambda^1\left(1+N_\alpha^0-f_{\lambda'}^0\right)-f_{\lambda'}^1\left(N_\alpha^0+f_\lambda^0\right)\right]L_\lambda^{\lambda'\alpha}\\&=\beta e\mathbf{E}\cdot(\mathbf{F}_\lambda-\mathbf{F}_{\lambda'})\,f_\lambda^0\left(1-f_\lambda^0\right)\left(1+N_\alpha^0-f_{\lambda'}^0\right)L_\lambda^{\lambda'\alpha},\end{aligned}\tag{B.7}$$

where we have used the following identity

$$f_{\lambda-\alpha}^0(1-f_{\lambda-\alpha}^0)(f_\lambda^0+N_\alpha^0)=f_\lambda^0(1-f_\lambda^0)(1+N_\alpha^0-f_{\lambda-\alpha}^0)$$

in the last equality.

Similarly, the second term of Eq. (B.5) can be expressed as

$$P_{\lambda\alpha\leftrightarrow\lambda'}=f_\lambda\left(1-f_{\lambda'}\right)N_\alpha L_{\lambda\alpha}^{\lambda'}-\left(1-f_\lambda\right)f_{\lambda'}\left(1+N_\alpha\right)L_{\lambda'}^{\lambda\alpha}.$$

Again, linearizing it and keeping terms up to the first order of $\mathbf{E}$, we get

$$\begin{aligned}P_{\lambda\alpha\leftrightarrow\lambda'}&\simeq\left[f_\lambda^1\left(N_\alpha^0+f_{\lambda'}^0\right)-f_{\lambda'}^1\left(1+N_\alpha^0-f_\lambda^0\right)\right]L_{\lambda\alpha}^{\lambda'}\\&=\beta e\mathbf{E}\cdot(\mathbf{F}_\lambda-\mathbf{F}_{\lambda'})\,f_\lambda^0\left(1-f_\lambda^0\right)\left(N_\alpha^0+f_{\lambda'}^0\right)L_{\lambda\alpha}^{\lambda'},\end{aligned}\tag{B.8}$$

where we have used the detailed balance

$$f_\lambda^0\left(1-f_{\lambda+\alpha}^0\right)N_\alpha^0=\left(1-f_\lambda^0\right)f_{\lambda+\alpha}^0\left(1+N_\alpha^0\right)$$

and the identity

$$f_{\lambda+\alpha}^0(1-f_{\lambda+\alpha}^0)(1+N_\alpha^0-f_\lambda^0)=f_\lambda^0(1-f_\lambda^0)(N_\alpha^0+f_{\lambda+\alpha}^0).$$

Combining Eq. (B.7) and Eq. (B.8), the rate of change of f_λ due to first order e-ph scattering can be expressed as

$$P_{\lambda\leftrightarrow\lambda'\alpha}+P_{\lambda\alpha\leftrightarrow\lambda'}=\beta e\mathbf{E}\cdot(\mathbf{F}_\lambda-\mathbf{F}_{\lambda'})\,f_\lambda^0\left(1-f_\lambda^0\right)\widetilde{\Gamma}_{\lambda\lambda'\alpha}^{(1\mathrm{ph})},\tag{B.9}$$

where $\widetilde{\Gamma}_{\lambda\lambda'\alpha}^{(1\mathrm{ph})}$ is defined as

$$\widetilde{\Gamma}_{\lambda\lambda'\alpha}^{(1\mathrm{ph})}\equiv\left(1+N_\alpha^0-f_{\lambda'}^0\right)L_\lambda^{\lambda'\alpha}+\left(N_\alpha^0+f_{\lambda'}^0\right)L_{\lambda\alpha}^{\lambda'}.$$

Second order scattering

We move on to the next-to-leading order scattering listed in the second line of Eq. (B.5). The calculation is a straightforward extension of the first order case. The rate of change of f_λ due to second order scattering can be expressed as

$$P_{\lambda\leftrightarrow\lambda'\alpha\alpha'} = \frac{1}{2} f_\lambda \left(1 - f_{\lambda'}\right) \left(1 + N_\alpha\right) \left(1 + N_{\alpha'}\right) L_\lambda^{\lambda'\alpha\alpha'} - \frac{1}{2} \left(1 - f_\lambda\right) f_{\lambda'} N_\alpha N_{\alpha'} L_{\lambda'\alpha\alpha'}^{\lambda},$$

$$P_{\lambda\alpha\alpha'\leftrightarrow\lambda'} = \frac{1}{2} f_\lambda \left(1 - f_{\lambda'}\right) N_\alpha N_{\alpha'} L_{\lambda\alpha\alpha'}^{\lambda'} - \frac{1}{2} \left(1 - f_\lambda\right) f_{\lambda'} \left(1 + N_\alpha\right) \left(1 + N_{\alpha'}\right) L_{\lambda'}^{\lambda\alpha\alpha'},$$

$$P_{\lambda\alpha\leftrightarrow\lambda'\alpha'} = f_\lambda \left(1 - f_{\lambda'}\right) N_\alpha \left(1 + N_{\alpha'}\right) L_{\lambda\alpha}^{\lambda'\alpha'} - \left(1 - f_\lambda\right) f_{\lambda'} \left(1 + N_\alpha\right) N_{\alpha'} L_{\lambda'\alpha'}^{\lambda\alpha},$$

where the factors of one half account for the fact that the two phonons in states α and α' are indistinguishable. Each of the three processes $P_{\lambda\leftrightarrow\lambda'\alpha\alpha'}$, $P_{\lambda\alpha\alpha'\leftrightarrow\lambda'}$, and $P_{\lambda\alpha\leftrightarrow\lambda'\alpha'}$ satisfy the detailed balance, which respectively gives

$$f_\lambda^0 \left(1 - f_{\lambda-\alpha-\alpha'}^0\right) \left(1 + N_\alpha^0\right) \left(1 + N_{\alpha'}^0\right) = \left(1 - f_\lambda^0\right) f_{\lambda-\alpha-\alpha'}^0 N_\alpha^0 N_{\alpha'}^0,$$

$$f_\lambda^0 \left(1 - f_{\lambda+\alpha+\alpha'}^0\right) N_\alpha^0 N_{\alpha'}^0 = \left(1 - f_\lambda^0\right) f_{\lambda+\alpha+\alpha'}^0 \left(1 + N_\alpha^0\right) \left(1 + N_{\alpha'}^0\right),$$

$$f_\lambda^0 \left(1 - f_{\lambda+\alpha-\alpha'}^0\right) N_\alpha^0 \left(1 + N_{\alpha'}^0\right) = \left(1 - f_\lambda^0\right) f_{\lambda+\alpha-\alpha'}^0 \left(1 + N_\alpha^0\right) N_{\alpha'}^0.$$

Linearizing these second order terms and keeping terms up to the first order of $\mathbf{E}$, we get

$$\begin{aligned} P_{\lambda\leftrightarrow\lambda'\alpha\alpha'} \simeq \frac{1}{2} L_\lambda^{\lambda'\alpha\alpha'} \big\{ & f_\lambda^1 \left[(1 + N_\alpha^0)(1 + N_{\alpha'}^0) - f_{\lambda'}^0 (1 + N_\alpha^0 + N_{\alpha'}^0)\right] \\ & - f_{\lambda'}^1 \left[N_\alpha^0 N_{\alpha'}^0 + f_\lambda^0 (1 + N_\alpha^0 + N_{\alpha'}^0)\right] \big\}, \end{aligned}$$

$$\begin{aligned} P_{\lambda\alpha\alpha'\leftrightarrow\lambda'} \simeq \frac{1}{2} L_{\lambda\alpha\alpha'}^{\lambda'} \big\{ & f_\lambda^1 \left[N_\alpha^0 N_{\alpha'}^0 + f_{\lambda'}^0 (1 + N_\alpha^0 + N_{\alpha'}^0)\right] \\ & - f_{\lambda'}^1 \left[(1 + N_\alpha^0)(1 + N_{\alpha'}^0) - f_\lambda^0 (1 + N_\alpha^0 + N_{\alpha'}^0)\right] \big\}, \end{aligned}$$

$$\begin{aligned} P_{\lambda\alpha\leftrightarrow\lambda'\alpha'} \simeq L_{\lambda\alpha}^{\lambda'\alpha'} \big\{ & f_\lambda^1 \left[N_\alpha^0 (1 + N_{\alpha'}^0) - f_{\lambda'}^0 (N_\alpha^0 - N_{\alpha'}^0)\right] \\ & - f_{\lambda'}^1 \left[(1 + N_\alpha^0) N_{\alpha'}^0 + f_\lambda^0 (N_\alpha^0 - N_{\alpha'}^0)\right] \big\}. \end{aligned}$$

Employing the following identities,

$$\begin{aligned} & f_\lambda^0 (1 - f_\lambda^0) \left[(1 + N_\alpha^0)(1 + N_{\alpha'}^0) - f_{\lambda-\alpha-\alpha'}^0 (1 + N_\alpha^0 + N_{\alpha'}^0)\right] \\ & \qquad = f_{\lambda-\alpha-\alpha'}^0 (1 - f_{\lambda-\alpha-\alpha'}^0) \left[N_\alpha^0 N_{\alpha'}^0 + f_\lambda^0 (1 + N_\alpha^0 + N_{\alpha'}^0)\right], \end{aligned}$$

$$\begin{aligned} & f_\lambda^0 (1 - f_\lambda^0) \left[N_\alpha^0 N_{\alpha'}^0 + f_{\lambda+\alpha+\alpha'}^0 (1 + N_\alpha^0 + N_{\alpha'}^0)\right] \\ & \qquad = f_{\lambda+\alpha+\alpha'}^0 (1 - f_{\lambda+\alpha+\alpha'}^0) \left[(1 + N_\alpha^0)(1 + N_{\alpha'}^0) - f_\lambda^0 (1 + N_\alpha^0 + N_{\alpha'}^0)\right], \end{aligned}$$

$$f^0_\lambda(1-f^0_\lambda)\left[N^0_\alpha(1+N^0_{\alpha'})-f^0_{\lambda+\alpha-\alpha'}(N^0_\alpha-N^0_{\alpha'})\right] \\ = f^0_{\lambda+\alpha-\alpha'}(1-f^0_{\lambda+\alpha-\alpha'})\left[(1+N^0_\alpha)N^0_{\alpha'}+f^0_\lambda(N^0_\alpha-N^0_{\alpha'})\right],$$

we arrive at

$$P_{\lambda\leftrightarrow\lambda'\alpha\alpha'}+P_{\lambda\alpha\alpha'\leftrightarrow\lambda'}+P_{\lambda\alpha\leftrightarrow\lambda'\alpha'}=\beta e\mathbf{E}\cdot(\mathbf{F}_\lambda-\mathbf{F}_{\lambda'})\,f^0_\lambda\left(1-f^0_\lambda\right)\widetilde{\Gamma}^{(2\mathrm{ph})}_{\lambda\lambda'\alpha\alpha'}. \quad \text{(B.10)}$$

Here, $\widetilde{\Gamma}^{(2\mathrm{ph})}_{\lambda\lambda'\alpha\alpha'}$ is defined as

$$\widetilde{\Gamma}^{(2\mathrm{ph})}_{\lambda\lambda'\alpha\alpha'}\equiv A^{\lambda'\alpha\alpha'}_\lambda L^{\lambda'\alpha\alpha'}_\lambda+A^{\lambda'}_{\lambda\alpha\alpha'}L^{\lambda'}_{\lambda\alpha\alpha'}+A^{\lambda'\alpha'}_{\lambda\alpha}L^{\lambda'\alpha'}_{\lambda\alpha},$$

where the thermal factors are rearranged and defined as

$$A^{\lambda'\alpha\alpha'}_\lambda=\frac{1}{2}\left[(1+N^0_\alpha)(1+N^0_{\alpha'}-f^0_{\lambda'})-N^0_{\alpha'}f^0_{\lambda'}\right],$$

$$A^{\lambda'}_{\lambda\alpha\alpha'}=\frac{1}{2}\left[N^0_\alpha(N^0_{\alpha'}+f^0_{\lambda'})+(1+N^0_{\alpha'})f^0_{\lambda'}\right],$$

$$A^{\lambda'\alpha'}_{\lambda\alpha}=N^0_\alpha+N^0_\alpha N^0_{\alpha'}+N^0_{\alpha'}f^0_{\lambda'}-N^0_\alpha f^0_{\lambda'}.$$

Note that these thermal factors are the same as those derived from the many-body perturbation theory [see Eq. (3.4)].

Linearized Boltzmann transport equation

Combining Eqs. (B.4), (B.9) and (B.10), we finally obtain the linearized BTE:

$$\mathbf{v}_\lambda=\sum_{\lambda'\alpha}(\mathbf{F}_\lambda-\mathbf{F}_{\lambda'})\,\widetilde{\Gamma}^{(1\mathrm{ph})}_{\lambda\lambda'\alpha}+\sum_{\lambda'\alpha\alpha'}(\mathbf{F}_\lambda-\mathbf{F}_{\lambda'})\,\widetilde{\Gamma}^{(2\mathrm{ph})}_{\lambda\lambda'\alpha\alpha'}.$$

Defining the total e-ph scattering rate as

$$\Gamma_\lambda=\Gamma^{(1\mathrm{ph})}_\lambda+\Gamma^{(2\mathrm{ph})}_\lambda=\sum_{\lambda'\alpha}\widetilde{\Gamma}^{(1\mathrm{ph})}_{\lambda\lambda'\alpha}+\sum_{\lambda'\alpha\alpha'}\widetilde{\Gamma}^{(2\mathrm{ph})}_{\lambda\lambda'\alpha\alpha'}, \quad \text{(B.11)}$$

the equation can be rearranged as

$$\mathbf{F}_\lambda=\mathbf{F}^0_\lambda+\tau_\lambda\left[\sum_{\lambda'\alpha}\mathbf{F}_{\lambda'}\widetilde{\Gamma}^{(1\mathrm{ph})}_{\lambda\lambda'\alpha}+\sum_{\lambda'\alpha\alpha'}\mathbf{F}_{\lambda'}\widetilde{\Gamma}^{(2\mathrm{ph})}_{\lambda\lambda'\alpha\alpha'}\right],$$

where $\mathbf{F}^0_\lambda=\tau_\lambda\mathbf{v}_\lambda$. Here, the relaxation time τ_λ is the inverse of the total scattering rate in Eq. (B.11), namely $\tau_\lambda=1/\Gamma_\lambda$, and $\mathbf{v}_\lambda$ is the band velocity.

Electron phonon dynamics

The last quantity needs to be determined is the intrinsic transition rate L. These intrinsic rates depend on the dynamics of the system, and hence are not regulated by the kinetic theory of Boltzmann. The method to obtaining an expression for the intrinsic rate L is well established once the Hamiltonian is given and the interactions between different states are known.

Take the one phonon absorption term $L^{\lambda'}_{\lambda\alpha} = L^{m\mathbf{k}'}_{n\mathbf{k},\,\nu\mathbf{q}} = L^{m\mathbf{k}+\mathbf{q}}_{n\mathbf{k},\,\nu\mathbf{q}}$ as an example. Note that we now use the full labels for the electron and phonon states and we have implicitly performed the summation over the final state momentum, $\Sigma_{\mathbf{k}'}$, which fixes $\mathbf{k}' = \mathbf{k} + \mathbf{q}$ by momentum conservation. Employing the Fermi golden rule, we get

$$L^{m\mathbf{k}+\mathbf{q}}_{n\mathbf{k},\,\nu\mathbf{q}} = \frac{2\pi}{\hbar} \left| g_{mn\nu}\left(\mathbf{k},\mathbf{q}\right)\right|^2 \delta\left(\varepsilon_{n\mathbf{k}} - \varepsilon_{m\mathbf{k}+\mathbf{q}} + \omega_{\nu\mathbf{q}}\right),$$

where $g_{mn\nu}\left(\mathbf{k},\mathbf{q}\right)$ is the e-ph coupling constant. Similarly, we can get the one phonon emission term as

$$L^{m\mathbf{k}+\mathbf{q},\,\nu-\mathbf{q}}_{n\mathbf{k}} = \frac{2\pi}{\hbar} \left| g_{mn\nu}\left(\mathbf{k},\mathbf{q}\right)\right|^2 \delta\left(\varepsilon_{n\mathbf{k}} - \varepsilon_{m\mathbf{k}+\mathbf{q}} - \omega_{\nu\mathbf{q}}\right).$$

The intrinsic transition rates involving two phonons can be determined either by using the second order time-dependent perturbation theory, or by employing the many-body perturbation theory as we did in Chapter 3. Both methods give the same results.

References

[1] M. Omini and A. Sparavigna, Physica B **212**, 101–112 (1995).

[2] D. A. Broido, A. Ward, and N. Mingo, Phys. Rev. B **72**, 014308 (2005).

[3] A. Chernatynskiy and S. R. Phillpot, Phys. Rev. B **82**, 134301 (2010).

[4] D. L. Rode, Phys. Rev. B **2**, 1012–1024 (1970).

[5] D. L. Rode and S. Knight, Phys. Rev. B **3**, 2534–2541 (1971).

[6] A. Faghaninia, J. W. Ager, and C. S. Lo, Phys. Rev. B **91**, 235123 (2015).

[7] W. Li, Phys. Rev. B **92**, 075405 (2015).

[8] T.-H. Liu, J. Zhou, B. Liao, D. J. Singh, and G. Chen, Phys. Rev. B **95**, 075206 (2017).

[9] J. Ma, A. S. Nissimagoudar, and W. Li, Phys. Rev. B **97**, 045201 (2018).

[10] G. D. Mahan, *"Many-Particle Physics"*, 3rd ed. (Springer, 2000).